

REPORT SERIES IN GEOPHYSICS

No 82

REMOTE SENSING OF SEA ICE PROPERTIES AND DYNAMICS
USING SAR INTERFEROMETRY

Marjan Marbouti

Institute for Atmospheric and Earth System Research (INAR)
Faculty of Science
University of Helsinki
Helsinki, Finland

Academic dissertation in geophysics

*Doctoral thesis, to be presented for public examination with the permission
of the Faculty of Science of the University of Helsinki, in Exactum B123
(Pietari Kalmin katu 5, Helsinki) on the 06th of April, 2022 at 12 o'clock.*

Helsinki 2022

Author's contact details:

Marjan Marbouti
Gustaf Hällströmin katu 2,
00560 Helsinki, Finland
Marjan.marbouti@helsinki.fi

Supervisors

Emeritus Professor Matti Leppäranta, Ph.D.
Institute for Atmospheric and Earth System Research, University of Helsinki,
Finland
Asst. Prof. Tuomo Nieminen, Ph.D.
Institute for Atmospheric and Earth System Research, University of Helsinki,
Finland
Asst. Prof. Jaan Praks, Ph.D.
Department of Electronics and Nanoengineering, Aalto University, Finland
Dr. Oleg Antropov, Ph.D.
VTT Technical Research Centre of Finland, Espoo, Finland

Reviewers

Docent Marko Makynen, Ph.D.
Group leader, Finnish Meteorological Institute, Finland
Assoc. Prof. Rasmus Tonboe, Ph.D.
National Space Institute, Technical University of Denmark, Denmark

Custos

Professor Petteri Uotila, Ph.D.
Institute for Atmospheric and Earth System Research, University of Helsinki,
Finland

Opponent

Dr. Juha Karvonen, Ph.D.
Finnish Meteorological Institute, Finland

Report Series in Geophysics No 82
ISBN 978-951-51-7991-3 (softcover)
ISSN 0355-8630
Unigrafia, Helsinki 2022

ISBN 978-951-51-7992-0 (PDF)
<http://ethesis.helsinki.fi/>
Helsingin yliopiston verkkojulkaisut
Helsinki 2022

Abstract

Landfast ice is attached to the coastline and islands and stays immobile over most of the ice season. It is an important element of polar ecosystems and plays a vital role as a marine habitat and in life of local people and economy through offshore technology. Landfast ice is routinely used for on-ice traffic, tourism, and industry, and it protects coasts from storms in winter from erosion. However, landfast ice can break or experience deformation in order of centimeters to meters, which can be dangerous for the coastline and man-made structures, beacons, on-ice traffic, and represents a safety risk for working on the ice and local people. Therefore, landfast ice deformation and stability are important topics in coastal engineering and sea ice modeling. In the framework of this dissertation, InSAR (SAR Interferometry) technology has been applied for deriving landfast ice displacements (publication I), and mapping sea ice morphology, topography and its temporal change (publication III). Also, advantages of InSAR remote sensing in sea ice classification compared to backscatter intensity were demonstrated (publications II and IV).

In publication I, for the first time, Sentinel-1 repeat-pass InSAR data acquired over the landfast ice areas were used to study the landfast ice displacements in the Gulf of Bothnia. An InSAR pair with a temporal baseline of 12 days acquired in February 2015 was used. In the study, the surface of landfast ice was stable enough to preserve coherence over the 12-day period, enabling analysis of the interferogram. The advantage of this long temporal baseline is in separating the landfast ice from drift ice and detecting long-term trends in deformation maps. The interferogram showed displacements of landfast ice on the order of 40 cm. The main factor seemed to be compression by drift ice, which was driven against the landfast ice boundary by strong winds from southwest.

Landfast ice ridges can hinder ship navigation, but grounded ridges help to stabilize the ice cover. In publication III, ridge formation and displacements in the landfast ice near Utqiagvik, Alaska were examined. The phase signatures of two single-pass bistatic X-band SAR (Synthetic Aperture Radar) image pairs acquired by TanDEM-X (TerraSAR-X add-on for Digital Elevation Measurements) satellite on 13 and 24 January 2012 were analyzed. Altogether six cases were identified with ridge displacement in four and formation in two cases under onshore compression. The ridges moved approximately 0.6 and 3.7 km over the study area and ridge formation reached up to 1 meter in upward. The results well corresponded with the locations identified as convergence zones retrieved from the drift algorithm generated by a SAR-based sea ice-tracking algorithm, backscatter intensity images and coastal radar imagery. This method could potentially be used in future to evaluate sea ice stability and ridge formation.

A bistatic InSAR pair acquired by the TanDEM-X mission in March 2012 over the Bothnian Bay was used in two further studies (publications II and IV). The potential of X-band InSAR imagery for automated sea ice classification was evaluated. The first results were presented in publication II and the data were further elaborated in publication IV. The backscatter intensity, coherence magnitude and InSAR-phase features, as well as their different combinations, were used as the informative features in classification experiments. In publication II, the purpose was to assess ice properties on the scale used in ice charting, with ice types based on ice concentration and sea ice morphology, while in publication IV, a detailed small-scale analysis was performed. In addition, the sampling design was different in these publications. In publication II, to achieve the best discrimination between open water and several sea-ice types, RF (Random Forests) and ML (Maximum likelihood) classifiers were employed. The best overall accuracies were

achieved by combining backscatter intensity & InSAR-phase using RF approach and backscatter intensity & coherence-magnitude using ML approach. The results showed the advantage of adding InSAR features to backscatter intensity for sea ice classification. In the further study (publication IV), a set of state-of-the-art classification approaches including ML, RF and SVM (Support Vector Machine) classifiers were used to achieve the best discrimination between open water and several sea-ice types. Adding InSAR-phase and coherence magnitude to backscatter intensity improved the OA (Overall Accuracy) compared to using only backscatter intensity. The RF and SVM algorithms gave somewhat larger OA compared to ML at the expense of a somewhat longer processing time. Results of publications II and IV demonstrate InSAR features have potential to improve sea ice classification. InSAR could be used by operational ice services to improve mapping accuracy of automated sea ice charting with statistical and machine learning classification approaches.

Preface

I am pleased to acknowledge the people who helped and inspired me throughout my doctoral study. First and foremost, my deepest gratitude goes to my main supervisor Emeritus Prof. Matti Leppäranta for tirelessly working and sharing his broad knowledge and experience with me. Matti, I am very grateful to you for giving me the opportunity to study an interesting research topic, for your helpful suggestions, encouragement and patience. In addition to scientific activities, I learned many lessons from you about real life. I am very lucky to have met you in my life.

I would also like to acknowledge Asst. Prof. Tuomo Nieminen and Assoc. Prof. Mikko Sipilä for timely support of my study and life. In addition to InSAR technology over sea ice, they familiarized me with other fields of science like new particle formation and ocean color properties that made me a versatile researcher in satellite remote sensing. I was working for several years with financial problems. In that situation, a nice man Prof. Markku Kulmala financially supported the rest of my dissertation research. Markku, I am deeply indebted to you for all the support, help and hosting me at your laboratory and familiarizing me with INAR group members in the atmospheric science.

I am very grateful to Asst. Prof. Jaan Praks, my supervisor at Aalto University who has guided me into the InSAR technology. He was the first person that opened my eyes professionally into InSAR and introduced me to another expert in this research area, Dr. Oleg Antropov. Special thanks to Oleg for scientific support in all of my papers and all his valuable advice and knowledge during the work on my doctoral dissertation. Oleg, you were not only my advisor in my study and doctoral dissertation, you also taught me how

one should speak, present and behave professionally in the academic community. I am deeply indebted to you for all those things.

I was lucky to be acquainted with Prof. Leif Eriksson at Chalmers University who invited me twice for scientific collaboration visits to his laboratory. He also introduced me to several new colleagues in remote sensing of sea ice, including Dyre Oliver Dammann, Denis Demchev, Joshua Jones and Anders Berg. I really enjoyed working with this lovely and inspiring group. I also want to express my great gratitude to Prof. Petteri Uotila for accepting my responsibility to continue my PhD and all supports.

I would also like to thank many other scientists who have been involved in my research, and featured as co-authors in my papers. I would like to thank Eero Rinne and Patrick Eriksson in FIS (Finnish Ice Service) who gave me valuable advice in sea ice research over the Baltic Sea.

Finally, my sincere gratitude goes to my family and friends who supported, encouraged and inspired me from the beginning until the end.

Contents

| | |
|---|-------------|
| Abstract | iii |
| Preface | vi |
| List of appended papers and author's contribution | x |
| Author's contribution..... | xi |
| List of acronyms and symbols | xiii |
| 1 Introduction | 1 |
| 2 Physical properties of sea ice | 7 |
| 2.1 Small-scale properties of sea ice..... | 7 |
| 2.1.1 Sea ice forms..... | 8 |
| 2.1.2 Sea ice salinity and impurities..... | 8 |
| 2.2 Sea ice fields..... | 10 |
| 2.2.1 Sea ice morphology | 11 |
| 2.3 Baltic Sea ice | 16 |
| 2.4 Arctic sea ice (Alaska coast- Chukchi and Beaufort Seas)..... | 23 |
| 3 Microwave remote sensing of sea ice | 26 |
| 3.1 Microwave radiometers | 27 |
| 3.2 Active microwave sensors | 27 |
| 4 Basics of Radar, SAR and InSAR | 35 |
| 4.1 Radar and SAR | 35 |
| 4.2 Interferometric SAR concepts | 37 |
| 4.3 InSAR for DEM generation..... | 43 |
| 4.4 InSAR for displacement measurements | 47 |
| 4.5 The interferometric processing | 49 |
| 4.6 Literature review in the context of the dissertation | 50 |
| 4.6.1 Sea ice classification studies | 51 |
| 4.6.2 Sea ice topography studies | 55 |
| 4.6.3 Sea ice displacement studies | 56 |
| 5 Study areas, SAR, in situ, and validation datasets | 57 |
| 5.1 Baltic Sea..... | 57 |

| | | |
|-------|--|-----|
| 5.2 | Arctic region | 66 |
| 6 | Methodology | 69 |
| 6.1 | InSAR methodological approach to retrieving sea ice displacements | 69 |
| 6.2 | Proposed classifications approach in sea ice classification | 70 |
| 6.3 | InSAR methodological approach to generate a Height Difference Map (HDM) | 75 |
| 7 | Results and discussion | 77 |
| 7.1 | Displacement analysis over Baltic landfast ice..... | 77 |
| 7.2 | Relative performance of different SAR features and their combinations over sea ice in RF and ML classifiers..... | 81 |
| 7.3 | Analyses and discussion of sea ice classification using InSAR features in RF, ML and SVM classifiers | 84 |
| 7.3.1 | OAs, UAs and PAs comparisons and class-wise performance for all classifiers (RF, ML, SVM)..... | 86 |
| 7.3.2 | Role of SAR interferometry in classification performance..... | 87 |
| 7.3.3 | Open water and sea ice discrimination | 88 |
| 7.4 | Ridge displacement and formation estimations over landfast ice near Utqiagvik Alaska..... | 93 |
| 7.4.1 | Detection of ridge displacement..... | 94 |
| 7.4.2 | Detection of ridge formation..... | 97 |
| 7.4.3 | Ridge formation and displacement discussions..... | 98 |
| 8 | Conclusions and directions for future work | 100 |
| | References..... | 105 |

List of appended papers and author's contribution

This dissertation consists of following publications, which are referred with the roman numbers in the text:

PI. Marbouti, M., J. Praks, O. Antropov, E. Rinne, and M. Leppäranta. 2017. "A Study of Landfast Ice with Sentinel-1 Repeat-pass Interferometry over the Baltic Sea." *Remote Sensing* 9 (8): 833. DOI:[10.3390/rs9080833](https://doi.org/10.3390/rs9080833).

PII. Marbouti, M., O. Antropov, P. B. Eriksson, J. Praks, V. Arabzadeh, E. Rinne, and M. Leppäranta. 2018. "Automated Sea Ice Classification over the Baltic Sea Using Multiparametric Features of TanDEM-X InSAR Images." *In Proceedings of IEEE International Geoscience and Remote Sensing Symposium (IEEE Xplore)*, 22-27 July 2018, Valencia, Spain. DOI:[10.1109/IGARSS.2018](https://doi.org/10.1109/IGARSS.2018).

PIII. Marbouti, M., L. E. B. Eriksson, D. O. Dammann, D. Demchev, J. Jones, A. Berg, and O. Antropov. 2020. "Evaluating Landfast Sea Ice Ridging near Utqiagvik Alaska Using TanDEM-X Interferometry." *Remote Sensing* 12 (8): 1247. DOI:[10.3390/rs12081247](https://doi.org/10.3390/rs12081247).

PIV. Marbouti, M., O. Antropov, P. B. Eriksson, J. Praks, V. Arabzadeh, E. Rinne, and M. Leppäranta. 2018. "TanDEM-X multiparametric data features in sea ice classification over the Baltic sea." *Geo-spatial Information Science* 24 (2): 313–332. DOI:[10.1080/10095020.2020.1845574](https://doi.org/10.1080/10095020.2020.1845574).

Author's contribution

PI “A Study of Landfast Ice with Sentinel-1 Repeat-Pass Interferometry over the Baltic Sea.”

Matti Leppäranta and Eero Rinne designed the study. Marjan Marbouti was primarily responsible for the experimental analysis. Marjan Marbouti, Jaan Praks, Oleg Antropov and Matti Leppäranta contributed to the results interpretation and discussion. Marjan Marbouti wrote the manuscript with contributions and revisions from all authors.

PII “Automated Sea ice Classification over the Baltic Sea using Multiparametric Features of TanDEM-X InSAR Images”

Oleg Antropov designed the study. Marjan Marbouti was primarily responsible for the experimental analysis. Patrick Eriksson made the validation dataset. Marjan Marbouti, Oleg Antropov, Jaan Praks, and Matti Leppäranta contributed to the results interpretation and discussion. Vahid Arabzadeh helped Marjan Marbouti in part of the analysis. Marjan Marbouti wrote the manuscript with contributions and revisions from all authors.

PIII “Evaluating Landfast Sea Ice Ridging near Utqiagvik Alaska Using TanDEM-X Interferometry”

Marjan Marbouti, Dyre Oliver Dammann and Leif E. B. Eriksson designed the study. Dyre Oliver Dammann and Leif E. B. Eriksson supervised the research. Methodology steps, formal analysis and investigation were done by Marjan Marbouti, Dyre Oliver Dammann, Leif E. B. Eriksson and Denis Demchev. Visualization was done by Marjan Marbouti. Joshua Jones and Denis Demchev made the validation dataset. Marjan Marbouti wrote the manuscript

with contributions, revisions and edits from all authors. Anders Berg and Leif E. B. Eriksson were responsible for funding acquisition.

PIV “TanDEM-X Multiparametric Data Features in Sea Ice Classification over the Baltic Sea”

Oleg Antropov and Marjan Marbouti designed the study. Marjan Marbouti and Oleg Antropov were primarily responsible for the experimental analysis. Patrick Eriksson and Matti Leppäranta made the validation dataset. Marjan Marbouti, Oleg Antropov, Patrick Eriksson and Matti Leppäranta contributed to the results interpretation and discussion. Vahid Arabzadeh helped Marjan Marbouti in part of the analysis. Marjan Marbouti wrote the manuscript with contributions and revisions from all authors.

Publications I–V are reprinted with permission as follows:

- Publications I, III and IV are Open Access and subject to the Creative Commons Attribution License (CC BY).
- Publication II: ©2018 IEEE. Reprinted, with permission, from Marbouti, M., O. Antropov, P. B. Eriksson, J. Praks, V. Arabzadeh, E. Rinne, and M. Leppäranta, Automated Sea Ice Classification over the Baltic Sea Using Multiparametric Features of TanDEM-X InSAR Images, In Proceedings of IEEE International Geoscience and Remote Sensing Symposium (IEEE Xplore), July 2018.

List of acronyms and symbols

Acronyms

The following abbreviations are used in this dissertation:

| | |
|---------|--|
| AMI-SAR | Active Microwave Instrument - Synthetic Aperture Antenna |
| AMSR-2 | Advanced Microwave Scanning Radiometer 2 |
| ALOS | Advanced Land Observing Satellite |
| AP | Alternating Polarization |
| ASAR | Advanced Synthetic Aperture Radar |
| ASI | Agenzia Spaziale Italiana (Italy) |
| BEPERS | Bothnian Experiment in Preparation for ERS-1 |
| CAST | Chinese Academy of Space Technology |
| CDTI | Centro para el Desarrollo Tecnológico Industrial (Spain) |
| CFOSAT | Chinese-French Oceanography Satellite |
| CIS | Canadian Ice Service |
| CM | Confusion Matrix |
| CNSA | China National Space Administration |
| CONAE | Comisión Nacional de Actividades Espaciales |
| COSI | Corea SAR Instrument |
| CoSSC | Coregistered Single-look Slant-range Complex |

| | |
|---------|---|
| CRS | Coarse Resolution ScanSAR |
| CSG-SAR | COSMO-SkyMed Second Generation Synthetic Aperture Radar |
| CSK | COSMO-SkyMed |
| CSA | Canadian Space Agency (Canada) |
| DEM | Digital Elevation Model |
| DInSAR | Differential InSAR |
| DIR | Degree of Ice Ridging |
| DLR | Deutsches Zentrum für Luft- und Raumfahrt (Germany) |
| ECOC | Error-Correcting Output Codes |
| ENVISAT | Environmental Satellite |
| ERS | European Remote-sensing Satellite |
| ESA | European Space Agency |
| EW | Extra Wide swath |
| FBI | Frozen Brash Ice |
| FIMR | Finnish Institute of Marine Research |
| FIS | Finnish Ice Service |
| FMI | Finnish Meteorological Institute |
| FYI | First-year ice |
| FRS | Fine Resolution Stripmap |

| | |
|---------|---|
| GM | Global Monitoring |
| GLAS | Geoscience Laser Altimeter System |
| GLCM | Gray-Level Co-occurrence Matrix |
| HDI | Highly Deformed Ice |
| HDM | Height Difference Map |
| HJ-1C | Huan Jing 1C |
| HoA | Height of Ambiguity |
| HRS | High Resolution Spotlight |
| HUTSCAT | Helsinki University of Technology Scatterometer |
| ICESat | Ice, Cloud and land Elevation Satellite |
| IM | Image |
| InSAR | SAR Interferometry |
| ISA | Israel Space Agency |
| ISRO | Indian Space Research Organisation |
| IW | Interferometric Wide swath |
| JAXA | Japan Aerospace Exploration Agency |
| JERS | Japan Earth Resources Satellite |
| KARI | Korea Aerospace Research Institute |
| KOMPSAT | Korea Multi-Purpose Satellite |
| LBI | Loose Brash Ice |

| | |
|---------------|---|
| LOS | Line Of Sight |
| MIZ | Marginal Ice Zone |
| ML | Maximum Likelihood |
| MLP | Multi-Layer Perceptron |
| MODIS | Moderate Resolution Imaging Spectroradiometer |
| MRF | Markov random fields |
| MRS | Medium Resolution ScanSAR |
| MYI | Multi-year ice |
| NASA | National Aeronautics and Space Administration |
| NM | Nautical Mile |
| NN | Neural Network |
| NWS | National Weather Service |
| OA | Overall Accuracy |
| OceanSat-2,3A | Satellite for the Ocean – 2,3A (India) |
| OSCAT | OceanSat Scatterometer |
| OTB | Orfeo ToolBox |
| OVA | One-Vs-All |
| OVO | One-Vs-One |
| OW | Open Water leads |
| PA | Producer's Accuracy |

| | |
|------------|---|
| PALSAR | Phased-Array L-band Synthetic Aperture Radar |
| QuikSCAT | Quick Scatterometer Mission |
| RAR | Real Aperture Radar |
| RF | Random Forests |
| RISAT | Radar Imaging Satellite |
| RLI | Rough Level Ice |
| SAOCOM | SAtélite Argentino de Observación COndiciones Microondas |
| SAR | Synthetic Aperture Radar |
| SAR-2000 | Synthetic Aperture Radar 2000 (X-band) |
| SAR-C | Synthetic Aperture Radar (C-band) |
| SAR-L | Synthetic Aperture Radar (L-band) |
| SAR-S | Synthetic Aperture Radar (S-band) |
| SAR-X | Synthetic Aperture Radar (X-band) |
| SEOSAR/Paz | Satélite Español de Observación SAR (also Paz) |
| SDI | Slightly Deformed Ice |
| SIC | Sea Ice Concentration |
| SLIE | Seaward Landfast Ice Edge |
| SITE | Sliding Spotlight |
| SLAR | Side-Looking Airborne Radar |
| SLC | Single Look Complex |

| | |
|----------|---|
| SLI | Smooth Level Ice |
| SM | Stripmap |
| SMHI | Swedish Meteorological and Hydrological Institute |
| SNAP | Sentinel's Application Platform |
| SNAPHU | Statistical-cost Network-flow Algorithm for PHase Unwrapping |
| SNR | Signal to Noise Ratio |
| SPOT | Spotlight |
| SVM | Support Vector Machine |
| TanDEM-X | TerraSAR-X Add-on for Digital Elevation Measurement |
| TOPSAR | Terrain Observation with Progressive Scans SAR |
| UA | User's Accuracy |
| UKSA | United Kingdom Space Agency (former BNSC) |
| UTM | Universal Transverse Mercator |
| WMO | World Meteorological Organization |
| WV | Wave |

Symbols

| | |
|------------------|--|
| A | The signal's amplitude |
| B_{\perp} | Perpendicular baseline |
| $B_{\perp,crit}$ | Critical baseline |
| B_{rg} | System bandwidth |
| C_1 and C_2 | Two co-registered complex SAR images |
| c | Speed of light |
| h | Height of radar above the ground |
| Δh | Topographic height variation |
| I | Interferogram |
| j | Imaginary unit |
| K | Number of classes |
| k | Wave number |
| L_S | The length of the synthetic aperture |
| L_p | Antenna length |
| p | Monostatic or bistatic factor |
| r | Distance of the sensor from the target or slant range |
| Δr | Difference in range distance |
| Δr_r | Relative scatterer displacement projected on the slant range direction |

| | |
|-------------------------|--------------------------------|
| S_i | Salinity of ice |
| S_w | Salinity of sea water |
| y | Segregation coefficient |
| T | Temperature |
| Δt | Time difference |
| v_a | Volume fraction of gas bubbles |
| X_r | Slant range resolution |
| X_{gr} | Ground range resolution |
| X_a | Azimuth resolution (RAR) |
| $X_{a,SAR}$ | Azimuth resolution (SAR) |
| γ | Coherence magnitude |
| $\gamma_{baseline}$ | Baseline decorrelation |
| γ_{volume} | Volume decorrelation |
| γ_{therm_noise} | Thermal noise decorrelation |
| $\gamma_{processor}$ | Processor decorrelation |
| $\gamma_{temporal}$ | Temporal decorrelation |
| θ | Incidence angle |
| θ_l | Local incidence angle |
| λ | Wavelength |
| τ | Pulse length |

| | |
|---------------------------------|------------------------|
| $\varphi, \varphi_1, \varphi_2$ | The respective phases |
| $\varphi_{flat-earth}$ | Flat earth phase |
| φ_{topo} | Topography phase |
| $\varphi_{displacement}$ | Displacement phase |
| φ_{atmos} | Atmospheric phase |
| φ_{noise} | Phase noise |
| $\Delta\varphi$ | InSAR phase difference |

1 Introduction

Arctic sea ice is an important part of the climate system. The Arctic sea ice forms a large sea ice cover, in average of 15 million km² at its maximal extent. The Arctic sea ice includes two main sea ice types: (a) FYI (first-year ice) which has formed in the current freeze-up period; and (b) perennial or MYI (multi-year ice), which has survived for a minimum of a year or more. (Wadhams 2000)

MYI is much thicker than FYI and this difference is stronger (MYI thicker than 3.5 m) along the northern coast of Canada and Greenland (Haas et al. 2006, 2010). MYI has a much rougher surface and lower salinity, and therefore smaller dielectric constant, than FYI. Therefore, due to the lower salinity, it is much stronger than FYI and this makes barriers for icebreakers (Wadhams 2000). In the past, the Arctic Ocean was covered with MYI but its coverage has decreased from 75% in the mid-1980s to 45% in 2011 (Maslanik et al. 2011). The present MYI tends to be younger than before (Maslanik et al. 2011). So, MYI is shrinking both in extent and volume. By continuation of this trend, the Arctic Ocean will be free of sea ice in summer roughly 2020 or earlier, 2030 \pm 10 years, and 2040 or later. (Overland and Wang 2013)

The Baltic Sea in northern Europe is located in the seasonal sea ice zone. Its annual sea ice extent is from 10 to 100% of the Baltic Sea area and ice season duration is up to seven months (Leppäranta and Myrberg 2009). The long-term evolution of the Baltic Sea ice conditions gives the countries around the Baltic Sea reasons to worry, because even small changes in climate will change sea ice conditions in the Baltic Sea heavily (Jevrejeva et al. 2004). The Baltic Sea ice has only FYI with thickness 10-100 cm. Sea ice is divided into the landfast ice and drift ice zones. The landfast ice is present in the coastal

and archipelago areas attached to the coast and islands. The drift ice is dynamic and moves by winds and currents. (Leppäranta 2011)

Sea ice in both the Baltic Sea and Arctic Ocean influences the global climate including temperature and ocean–atmosphere interaction. As sea ice surface is bright, more sunlight is reflected back into the atmosphere and is not absorbed by the ocean. Lack and melting of sea ice reduce the reflectance of sunlight and more solar energy will be absorbed in the ocean. A cycle of warming and melting starts when the water becomes warmer producing delays for ice formation in cold periods. The ice area becomes smaller and melts faster in the following summer. These changes in sea ice amount can change ocean circulation that causes climate change. A small temperature increase can go to greater warming over time. Therefore, this makes polar regions sensitive to climate change on Earth. (NOAA 2021)

Ship navigation is very important in both Arctic and Baltic regions. In the Arctic Ocean, sea ice closes the northwest Passage through the Canadian Arctic Archipelago and the northeast Passage off the northern coast of Russia for most of the year (Weeks 2010). Even in summer, several icebreakers are used to open ways although recently more ways are free of sea ice for short periods (Weeks 2010). The Baltic Sea is one of the busiest maritime places on Earth because it handles up to 15% of the world's cargo traffic (Madjidian et al. 2013). Marine transportation increases yearly around 3-4%. The number of vessels increased from 38000 to 53000 from 2001 to 2015. To increase ship navigation safety, ice conditions in the Baltic Sea are monitored during winter and winter shipping is possible by using icebreakers and ice-strengthened vessels. Small harbors are closed during the winter due to navigation restrictions. Sea ice thickness up to 80 cm can be broken by powerful vessels although these vessels need icebreaker assistance to navigate through ridges,

heavy brash ice barriers, and ice under pressure. In overall, sea ice seasons make problems in navigation for 6-7 months in the Bay of Bothnia and 3-4 months in the Gulf of Finland. (Seinä et al. 2006)

During the last decades, SAR (Synthetic Aperture Radar) imaging has become a critically important tool for the sea ice remote sensing. Its principle is based on the emission of electromagnetic waves to illuminate the scene of interest, followed by measuring the backscatter intensity and generating a reflectivity map. Different information is obtained by SAR compared to optical and infrared sensors.

Radar imaging has several advantages over optical and infrared remote sensing systems. Firstly, radar sensors are active sensors, providing their own illumination, thus they operate independently of daylight. Secondly, because of radiowave penetration, radar imaging techniques can be applied during unfavorable weather conditions such as cloud cover or even rain, particularly at L, C, X bands. Thirdly, SAR sensors have high resolution because of virtual antenna synthesis. (Ulaby et al. 2014)

These make the SAR technique a unique tool to detect and analyze sea ice cover in the Arctic regions and in the seasonal sea ice zone with mostly cloudy weather and long polar nights. Sea ice services use SAR imagery as a main tool to produce ice charts for icebreakers as information for route optimization, fuel calculations and in general ship navigation (JCOMM Expert Team on Sea Ice 2017, Berglund and Eriksson 2015). To further extend the potential of SAR technology, a coherent technique called InSAR (SAR interferometry) is utilized. InSAR can be used for mapping ground topography and deformation. This technique has been used for detecting and measuring land deformation (Balzter 2017; Wang L et al. 2020), DEM (Digital Elevation Model) mapping (Geymen 2012; Chunxia et al. 2005; Zhou et al. 2012), earthquake assessment

(Devaraj and Yarrakula 2018; Aslan et al. 2018, 2019), and monitoring volcano eruptions (Kuraoka et al. 2018; Doke et al. 2018). This technique is also applicable for analysis of cm- to dm-scale displacement of landfast ice that puts coastal areas and on-ice traffic in danger (Dammert et al. 1998; Dammann et al. 2018a, 2018b).

The primary goal of this dissertation is elaboration of InSAR techniques for characterization of sea ice and its dynamics. This particularly includes demonstration of InSAR approaches for detecting cm- to meter-scale landfast ice deformation, displacements and examining deformation factors and their mechanism over the Baltic Sea and Arctic coastal regions. Further, assessment of the InSAR utility for improving automatic sea ice classification is pursued, which motivates operational sea ice services to use InSAR approaches for automated sea ice charting with statistical and machine learning classification approaches.

The dissertation consists of four publications:

PI: A Study of Landfast Ice with Sentinel-1 Repeat-Pass Interferometry over the Baltic Sea.

This study was the first to examine the potential of Sentinel-1 data with 12-day temporal baseline in detecting and evaluating long-term deformation over the landfast ice. Also, forces that caused these displacements over the landfast ice were studied. In previous studies, landfast ice stability and displacements over the Baltic Sea were examined with very small temporal baselines (one day and three days).

PII: Automated Sea Ice Classification over the Baltic Sea using Multiparametric Features of TanDEM-X InSAR Images.

PIV: TanDEM-X Multiparametric Data Features in Sea Ice Classification over the Baltic Sea.

Sea ice classification in the ice services is largely done using SAR images while optical images, ground truth from icebreakers and fixed observation sites help sea ice experts in ice chart production. In PII and PIV, the aim was to extend the classification parameter space by introducing InSAR and investigate the applicability of coherence magnitude and InSAR phase to improve automated sea ice classification on different sea ice types at X-band. The goal was to present a workflow for automated sea ice classification using X-band InSAR data acquired by the TanDEM-X (TerraSAR-X add-on for Digital Elevation Measurements) mission. The plan was also to show potential of InSAR in discriminating open water and sea ice classes (especially new ice class) that were particularly difficult using only backscatter intensity in prior studies (Mäkynen and Hallikainen 2004; Dierking 2010, Leppäranta et al. 1992, Geldsetzer and Yackel 2009).

PIII: Evaluating Landfast Sea Ice Ridging near Utqiagvik Alaska Using TanDEM-X Interferometry.

Grounded ridges are important factors in the landfast ice extension and stability. In this study, the focus was on the InSAR potential to measure ridge formation and displacement. To the best of our knowledge, InSAR technique has never been used earlier for this purpose. The stability of the landfast ice cover near Utqiagvik offshore Alaska in the context of the frictional force from grounded ridges has been evaluated in previous studies (Jones et al. 2016; Mahoney et al. 2007b; Druckenmiller 2011). Previously, InSAR technique was used to assess the surface morphology, extent and height of grounded ridges (Dammann et al. 2018b, Dierking et al. 2017).

The structure of the dissertation can be summarized as follows:

Physical properties of sea ice with focusing on the Baltic and Arctic sea ice (Alaska coast- Chukchi and Beaufort Seas) are given in Chapter 2. In Chapter 3, the basics and relevant concepts of microwave remote sensing of sea ice with more focusing on SAR are described. Basics of radar, SAR and InSAR are explained in Chapter 4. Then, in the literature review, specific SAR and InSAR studies for sea ice classification, retrieving sea ice topography and displacement are given. A description of study sites in the Baltic Sea and Arctic region can be found along with a description of SAR and reference data in Chapter 5. Chapter 6 presents primary methodological approaches. Subsections 6.1 and 6.3 formulate approaches for retrieving sea ice displacements and topography that were used in PI and PIII, respectively. The proposed sea ice classification approaches (PII and PIV) are described in subsection 6.2. Chapter 7 contains experimental results and discussions to determine the displacement analysis over the Baltic landfast ice (section 7.1), as well as relative performance of different SAR features and their combinations over sea ice in RF (Random Forests) and ML (Maximum likelihood) classifiers for PII (section 7.2). Analyses and discussion of sea ice classification using InSAR features over sea ice in RF, ML and SVM (Support Vector Machine) classifiers in PIV are presented in section 7.3. In addition, ridge displacements and formation over landfast ice near Utqiagvik, Alaska are experimentally studied and discussed in section 7.4. Chapter 8 concludes the dissertation and gives perspectives for future research directions.

2 Physical properties of sea ice

Sea ice physics is studied over a wide range of scales. Microscale includes individual grains and ice impurities extending from the sub-millimeter region to 0.1 m. In the local scale, 0.1-10 m, sea ice is a solid sheet, a polycrystalline continuum with sub-structure classified according to the formation mechanism into congelation ice, snow-ice, and frazil ice. The ice floe scale extends from 10 m to 10 km, including individual floes and ice forms such as rubble, pressure ridges and landfast ice. When the scale exceeds the floe size, the sea ice medium is called drift ice or pack ice, and, in dynamical oceanography, the mesoscale is around 100 km and the scales from 1000 km upward are in the large-scale regime. (Leppäranta 2011)

2.1 Small-scale properties of sea ice

Sea ice crystals form of water molecules. They are uniaxial, with the optical axis or the c-axis perpendicular to the basal plane. Multiple crystals generate macrocrystals by overlaying together and acting optically as single crystals. The size of macrocrystals or grains is between 10^{-4} to 10^{-1} m and their shape depends on the mode of ice formation. Due to the dissolved substances in seawater, crystal boundaries in sea ice are irregular, and there are brine inclusions inside of macrocrystals between the single crystal platelets. (Weeks and Ackley 1986; Wadhams 2000)

The texture structure of sea ice cover can be divided into three classes: (1) columnar ice: elongated ice grains with size of 1-10 cm, brine inclusions are parallel layers within grains; (2) intermediate columnar/granular ice: grain size 1-10 cm, irregular horizontal banding with crystals exhibiting a slight elongation in the vertical direction, brine inclusions are a string of isolated oblong pockets; and (3) granular ice: grain size < 1 cm, brine inclusions are

irregular pockets or droplets between the grains. The crystal structure depends on the mode of ice formation. (Weeks and Ackley 1986; Eicken and Lange 1989)

2.1.1 Sea ice forms

Sea ice formation is based on three different mechanisms which result in congelation ice, snow-ice and frazil ice (Weeks and Ackley 1986; Weeks 1998; Eicken and Lange 1989; Palosuo 1963). Congelation ice crystals grow down from the ice–water interface and the crystals are columnar with a diameter of 0.5–5 cm and height of 5–50 cm. Congelation ice is the dominant ice type in the Arctic Ocean. Snow-ice is frozen slush forming an upper granular layer in the ice cover. The crystals are on the order of 1 mm in size. Its contribution is small in Arctic seas but can account for more than 50% of the vertical ice layer in subarctic seas where solid precipitation is large. Frazil ice forms in turbulent open water. The crystals are very fine, less than 1 mm. They move freely with the water in the turbulent flow and may attach to the bottom of solid ice floes, accumulate together to form a solid sheet at the surface, or attach to the sea bottom in shallow and well-mixed waters resulting in anchor ice. In the Antarctic seas, frazil ice is the dominant ice type. (Weeks and Ackley 1986)

2.1.2 Sea ice salinity and impurities

Salinity is a key characteristic of sea ice (Weeks and Ackley 1986; Wadhams 2000). It plays a central role in determining the thermal, mechanical, electrical, and radiometric properties of sea ice. When sea water freezes, ice crystals form from water molecules and most of the sea ice impurities are separated from the solid phase of water. The crystal plates originate as dendrites with tips protruding into the seawater. The brine is trapped between these tips. At this step, the sea ice captures a high amount of salt. With time, the brine drains out

and the sea ice salinity decreases. Brine can go out of sea ice in different ways: brine pocket migration, brine expulsion, gravity drainage, and flushing. When sea ice warms, disconnected brine inclusions coalesce into vertical channels that can lead to redistribution, drainage, and desalination of the ice. (Weeks and Ackley 1986)

The salinity of new ice S_i is a fraction of the salinity of sea water S_w and is shown by (Weeks and Ackley 1986):

$$S_i = \gamma S_w, \quad (1)$$

where $\gamma \approx 0.25 - 0.5$ is the segregation coefficient, which depends on the rate of growth, so that a higher growth rate captures more salts. Since the rate of growth in general decreases when ice gets thicker, the top layer of new or young congelation ice has the maximum salinity (Weeks and Ackley 1986). The vertical salinity profile of sea ice develops as a result of entrapment and advection of brine into C-shape (maximums at the top and bottom, minimum in the middle) in midwinter, changing into an I-shape as the ice becomes warmer. In the summer melting season, the brine pockets expand to form a drainage network, and the salinity profile turns to an inverse C-shape (minimum on the top and the bottom). The brine volume can be calculated based on the temperature, salinity and density of sea ice from the phase diagram of sea ice. (Weeks and Ackley 1986; Eicken and Lange 1989)

The formulas are given in Cox and Weeks (1983) for temperature $T \leq -2^\circ\text{C}$ and Leppäranta and Manninen (1988) for temperature $-2^\circ\text{C} \leq T \leq 0^\circ\text{C}$. The brine volume is less than 1% in cold sea ice (below -20°C) while in warm sea ice (around -2°C), it can have large brine volume (10%-20%). The other impurities of sea ice consist of gas bubbles, sediments, and biota. Gas bubbles originate from seawater or sea bottom and in the snow-ice layer from air inclusions trapped by the parent snow cover (Weeks and Ackley 1986;

Wadhams 2000). Their size is usually in millimeters but may reach to a few centimeters and their volume fraction is $v_a \sim 1\%$. In particular, because of their size, they scatter all wavelengths of light equally resulting in the gray or white appearance of ice with a large amount of gas bubbles (Askne et al. 1992; Leppäranta et al. 1992). As gas bubble size can be more than 1 cm close enough to the radar wavelength, gas bubbles are important for SAR backscatter intensity (Leppäranta et al. 1992). Sediments and biota are not as important as gas bubbles for the SAR signal (Leppäranta et al. 1998b). Sea ice sediments are non-living particles in the sea ice. They are created from suspended particles in the water, sea water bottom, or atmospheric deposition (Askne et al. 1992). Brine pockets act as biological habitats, where sea ice has its own biota, also in brackish sea ice (Ikävalko 1997; Horner et al. 1992). The skeleton layer at the ice bottom is the most active layer which is sometimes colored in brown-green due to algae existence (Arst et al. 2006).

2.2 Sea ice fields

Sea ice landscape has ice floes with ridges, leads and polynyas and other morphological features (Weeks 1980). Sea ice cover includes several zones with different dynamic characters (Weeks 1980). The landfast ice forms in the coastal and archipelago areas and it is attached to the land and islands. The landfast ice extends down to depths of 10-20 m from the shoreline (Zubov 1945; Volkov et al. 2002; Leppäranta 2011).

The area located near to the landfast ice is called the shear zone with the width 10-200 km. Ice mobility in the shear zone is restricted by the geometry of the boundary and strong deformations happen. One example of a shear zone is offshore in the Beaufort Sea. The central pack is located further out from the shear zone, and it is free from instant influence by the boundaries; its length scale is the size of the basin. MIZ (Marginal Ice Zone) can be found along the

edge toward the open sea. It is loosely characterized as the zone, which "feels the presence of the open ocean" and it covers around 100 km from the ice edge. MIZs can be found along the oceanic ice edge of the polar oceans. (Wadhams 2000; Leppäranta 2009)

2.2.1 Sea ice morphology

Sea ice cover consists of ice floes with a size distribution from meters to kilometers or tens of kilometers (Wadhams 2000). Ice floes break into smaller pieces, and in the cold season they are at the same time frozen together to form larger ones (Wadhams 2000). In winter, ice floes are typically rectangular or pentagon-shaped, while in summer, sharp corners wear and the floes become rounded (Timokhov 1998). Floe size distributions show statistical regularity based on random floe break-up mechanisms (Leppäranta 2011). Floes contain undeformed, level ice patches, and accumulations of ice blocks (Leppäranta 2011).

The thickest ice block accumulations are sea ice ridges (Timco and Burden 1997; Wadhams 2000), which are typically 5–30 m thick. Over large areas, their volume may account for up to about one-half of the total ice volume. A simple structural model of ridges consists of a triangular sail on top of a reversed triangular keel. In shallow areas where the sea depth is less than the keel depth, grounding of ridges takes place. This is typically observed at the landfast ice boundary. Grounded ridges serve as tie points to the ice and aid the landfast ice to extend farther away from the coast (Zubov 1945; Volkov et al. 2002).

For ice charting, sea ice classification is performed based on local and large-scale properties of sea ice. This includes **the surface structure, stage of ice development, ice thickness, ice concentration, and stage of ice melting**. Sea ice terminology has been standardized by the sea ice working group of WMO

(World Meteorological Organization), which established a nomenclature for sea ice reporting and chart production. Several national institutes including CIS (Canadian Ice Service), FMI (Finnish Meteorological Institute), Norwegian meteorological institute, and SMHI (Swedish Meteorological and Hydrological Institute) provide daily sea ice charts based on sea ice classes defined in the WMO nomenclature. (WMO 2014)

Surface structure

Based on the sea ice surface structure, division of sea ice is made into two primary classes called level ice and deformed ice. The level ice is formed by thermal growth, not affected by mechanical deformation. Divergence, convergence and shear of ice motion are the causes of deformed ice formation. Fractures and leads in a sea ice cover are caused by divergent motions. Deformed ice is divided into the following sub-classes as defined in the WMO sea ice nomenclature (WMO 2014; Seinä et al. 2001):

- **Rafted ice:** Type of deformed ice formed by one piece of ice overriding another.
- **Finger rafted ice:** Type of rafted ice in which floes thrust 'fingers' alternately over and under the other.
- **Ice ridge:** A line or wall of broken ice forced up by pressure. May be fresh or weathered. The submerged volume of broken ice under a ridge is termed an ice keel.
- **Ridged ice:** Ice piled haphazardly one piece over another in the form of ridges or walls. Usually found in FYI (cf. ridging).
- **Hummocked ice:** Sea ice piled haphazardly one piece over another to form an uneven surface. When weathered, has the appearance of smooth hillocks.

- **Rubble field:** An area of extremely deformed sea ice of unusual thickness formed during the winter by the motion of drift ice against, or around a protruding rock, islet or other obstruction.

- **Brash ice:** Accumulations of floating ice made up of fragments not more than 2 m across, the wreckage of other forms of ice.

Stage of ice development and ice thickness

- **New ice** is a general term for recently formed ice where ice crystals are only weakly frozen together. Solid new ice cover grows through dark nilas (less than 5 cm thick), light nilas or ice rind (5-10 cm), grey ice (10-15 cm), grey-white ice (15-30 cm). Grey ice and grey-white ice are also called young ice.

- **Frazil ice:** Fine spicules or plates of ice, suspended in water.

- **Grease ice:** A later stage of freezing than frazil ice when the crystals have coagulated to form a soupy layer on the surface. Grease ice reflects little light, giving the sea a matt appearance.

- **Slush:** Snow which is saturated and mixed with water on land or ice surfaces, or as a viscous floating mass in water after a heavy snowfall.

- **Shuga:** An accumulation of spongy white ice lumps, a few centimeters across; they are formed from grease ice or slush and sometimes from anchor ice rising to the surface.

- **Pancake ice:** Predominantly circular pieces of ice from 30 cm to 3 m in diameter, and up to 10 cm in thickness, with raised rims due to the pieces striking against one another. It may be formed on slight swell from grease ice, shuga or a result of the breaking of ice rind, nilas or, under severe conditions of swell or waves, of grey ice.

Beyond young ice, which is the transition between nilas and FYI, sea ice is classified by its age as FYI and old ice (WMO 2014):

- **FYI** is sea ice of not more than one winter's growth, developing from young ice; with a thickness of 30 cm-2 m. It may be subdivided into thin FYI/white ice (30-70 cm), medium FYI (70-120 cm) and thick FYI (over 120 cm). Thin FYI/white ice can be divided into first stage (30-50 cm) and second stage (50-70 cm).

Sea ice that survived at least one summer's melt is **old ice**. Most topographic features are smoother than on FYI. Old ice is classified into (WMO 2014):

- **Residual ice:** FYI that has survived the summer's melt and is now in the new cycle of growth. It is 30 to 180 cm thick depending on the region where it was in summer. After 1 January (in the Southern hemisphere after 1 July), this ice is called second-year ice.

- **Second-year ice:** Old ice which has survived only one summer's melt; typical thickness up to 2.5 m and sometimes more. Because it is thicker than FYI, it stands higher out of the water. In contrast to MYI, summer melting produces a regular pattern of numerous small puddles. Bare patches and puddles usually appear greenish-blue.

- **MYI:** Old ice up to three meters or more thick which has survived at least two summers' melt. Hummocks even smoother than in second-year ice, and the ice is almost salt-free. Colour, where bare, is usually blue. Melt pattern consists of large interconnecting irregular puddles and a well-developed drainage system.

Note that in literature ice that is referred to as MYI may very well be second-year and more aptly described as old, in that its exact age may not be known,

only that it has survived at least one summer. Once sea ice survives a summer its salinity profile and physical properties are drastically changed.

Stage of ice melting

When sea ice and snow cover turn into the stage of melting, the water melted from snow and ice is accumulated as puddles on the sea ice surface. When the snow cover has regressed and sunlight can penetrate into the ice, sea ice melting begins inside the ice and possibly at the surface. Melt ponds can melt through the ice cover creating thaw holes. The freeboard dries from the surface melt water after the formation of cracks and thaw holes. During the period of drying, the ice surface whitens. The last stage of ice melting is rotten ice, which is sea ice with a honeycombed structure in an advanced state of disintegration. (WMO 2014; Wadhams 2000)

Ice concentration

In the scales larger than the floe size, the relative area of sea ice is the ice concentration, usually given in percentages or tenths (WMO 2014). WMO (2014) specifies the following concentration categories as:

| | |
|----------------|-----------------|
| Compact ice | 10/10 |
| Very close ice | 9/10 - < 10/10) |
| Close ice | 7/10-8/10 |
| Open ice | 4/10-6/10 |
| Very open ice | 1/10-3/10 |
| Open water | <1/10, |
| Ice free | 0 |

2.3 Baltic Sea ice

The Baltic Sea is a shallow, semi-enclosed, brackish sea water basin located in 53°50' - 64°50'N, 09°20' - 30°20'E in northern Europe (Voipio 1981). Nine countries (Denmark, Estonia, Finland, Germany, Latvia, Lithuania, Poland, Russia, and Sweden) have coastlines with the Baltic Sea (Leppäranta and Myrberg 2009).

The geographical division of the Baltic Sea includes fourteen parts, which are based on coastal morphology, sills, and other topographical formations. The deepest point in the Baltic Sea with 459 m is the Landsort Deep located in the Western Gotland Basin, southeast of Stockholm. The Baltic Sea has three main gulfs: the Gulf of Riga, the Gulf of Finland, and the Gulf of Bothnia. They are located to the east and north of the Gotland Sea. The Bothnian Gulf is in the northernmost part of the Baltic Sea between Finland and Sweden. It is a large water body including four basins: the Åland Sea, the Archipelago Sea, the Sea of Bothnia, and the Bay of Bothnia. The surface area of the Baltic Sea is 392978 km² and the mean depth is 54 m. Land uplift is up to 9 mm per year in the north and no uplift in the south. As the Baltic Sea is located at the edge of the seasonal sea ice zone, climate variations show up strongly in the ice season. (Leppäranta and Myrberg 2009)

The length of the ice seasons is 5-7 months, and the maximum annual ice extent has ranged within 12.5%-100% of surface area of the Baltic Sea (Leppäranta and Myrberg 2009). The corresponding averages are 6.4 months and 45% (Leppäranta and Myrberg 2009). Seinä & Palosuo (1996) did classification of five ice season types based on maximum annual extent of ice cover in the Baltic Sea. Classes are extremely mild (5200 to 81 000 km²), mild (81001 to 139000 km²), average (139 001 to 279 000 km²), severe (279 001 to 383 000 km²) and extremely severe (383 001 to 420 000 km²). Three classes

are shown in Figure 1. Considerable evidence suggests that large-scale atmospheric circulation patterns are significantly correlated with the ice conditions in the Baltic region (Jevrejeva 2001). In average and mild winters, warm air masses linked with westerly moving cyclones from the Atlantic dominate the Baltic climate while in severe winters, blocking anticyclonic patterns dominate (Jevrejeva and Moore 2001).

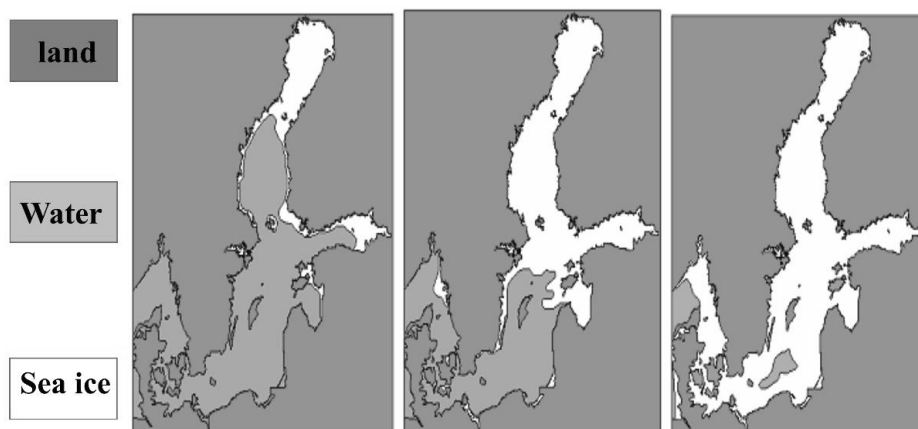
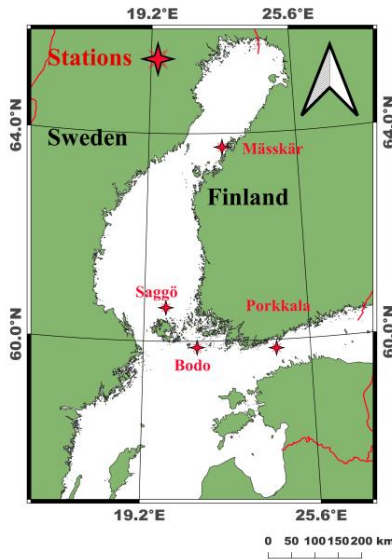


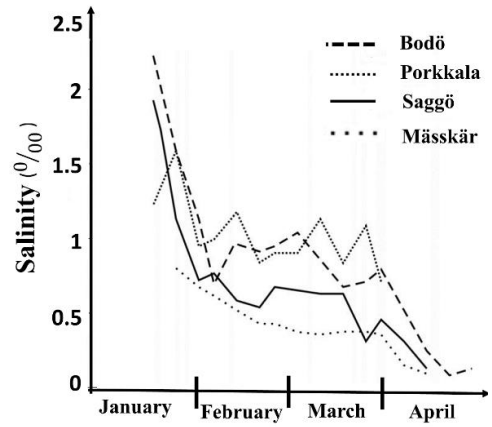
Figure 1. Classification of ice seasons in the Baltic Sea. Examples of (left) extremely mild, (middle) average and (right) extremely severe ice seasons (Grönvall and Seinä 1999).

Sea ice formation regularly starts in November and December in the northern Bay of Bothnia and the Gulf of Finland, respectively. The maximum annual ice extent occurs between January and March. During an average winter, ice covers the entire Bay of Bothnia by mid-January, and at the time of the maximum ice extent, at the turn of February and March, the ice covers the Gulfs of Bothnia, Finland, and Riga. Sea ice breakup begins in April and the ice melts completely by the end of May-beginning of June. (Seinä and Peltola 1991)

The seasonal Baltic Sea ice cover has several similarities in the ice structure to its oceanic counterpart in polar seas and oceans, although there are many special characteristics that result from the brackish waters from which the ice is formed, e.g., resulting in lower bulk salinities than in the Arctic regions (Granskog et al. 2006). In the Baltic Sea, water salinity values vary with location (Leppäranta and Myrberg 2009). The salinity of Baltic Sea ice ranges from 12‰ in the south-west to 2-7‰ in the northern Baltic Sea and to fresh water at the mouth of large rivers (Voipio 1981). The brackish nature of the sea is maintained by intermittent inflows of saline North Sea water through the Danish Straits (Voipio 1981). The mean vertical salinity of sea ice on the Finnish coast of the Baltic Sea was measured in stations Bodo, Mäskär, Saggö and Porkkala and was presented in a study by Palosuo (1963) (Figure 2). In the middle of the winter, salinity decreases a little due to brine pocket expulsion and consequent drainage, but it stays at the fraction of 0.2-0.3 of water salinity (Leppäranta and Myrberg 2009). In spring by the start of the melting season, the salinity decreases rapidly, and the residual level is on an order of 0.1 ppt (Leppäranta and Myrberg 2009).



(a)



(b)

Figure 2. (a) Raw data stations used in Palosuo (1963) study (b) Mean vertical salinity of ice on the Finnish coast of the Baltic Sea (Palosuo 1963).

As the basins of the Baltic Sea are big, solid ice lids cannot form on them. Landfast ice located in coastal and archipelago areas is stable and smooth during most of the winter. It is also supported by islands and grounded ice ridges on shoals. The landfast ice extension is to depths of 5-15 m which depends on the ice thickness, and it increases with time. In very extreme condition, the entire basin can be landfast ice covered for several weeks. The drift ice is located beyond the landfast ice boundary. The drift ice landscape includes leads, fields of ice floes, and deformed ice such as pressure ridges, rafted ice, and brash ice. (Lepparanta and Myrberg 2009)

Ridged ice is the most important drift ice type in the Baltic Sea. Ridge thickness is usually 5 to 15 m with a maximum around 30 m (Leppäranta and Hakala 1992). The maximum amount of ridging happens in the Bay of Bothnia next to the landfast ice boundary (Leppäranta and Hakala 1992). Ridges account for an average of 10-30% of the total ice mass over large areas

(Leppäranta and Hakala 1992). Open water areas are normally narrow linear formations, leads, which form particularly at the lee side of the landfast ice boundary (Lepparanta and Myrberg 2009). Narrow leads can also be found in the interior of drift ice fields. Leads are formed at weak points in the drift ice field by means of mechanical processes (Lepparanta and Myrberg 2009). The structural arrangements of leads present a lot of information about the background process (Goldstein et al. 2000; Lepparanta and Myrberg 2009). The closing and opening of leads are short-term phenomena in the Baltic Sea (Lepparanta and Myrberg 2009).

Sea ice types are defined based on historical and practical shipping activities in ice-covered water bodies (WMO 2014). Definitions of the various ice types have been gathered to form a sea ice nomenclature (Table 1) which is used on ice charting in the Baltic Sea. FIMR (Finnish Institute of Marine Research) and its operational part FIS (Finnish Ice Service) provide sea ice information for navigational purposes in the area of the Baltic Sea, especially in the Gulf of Bothnia and Gulf of Finland. The ice charts are based on several sources of information, e.g. NOAA (National Oceanic and Atmospheric Administration), AVHRR (Advanced Very High Resolution Radiometer) images, RADARSAT-1 and Sentinel-1 images and field observations (JCOMM Expert Team on Sea Ice 2017, Berglund and Eriksson 2015).

Table 1. General and common Baltic Sea ice types (Armstrong et al. 1966; WMO 2014).

| | |
|--------------|---|
| Sea ice | Any form of ice found at sea that has originated from the freezing of seawater. |
| New ice | A general term for recently formed ice. |
| Frazil ice | Fine spicules or plates of ice in suspension in water. |
| Nilas | A thin elastic crust of ice, easily bending by waves and swell and rafting under pressure; matt surface and thickness up to 10cm. |
| Young ice | Ice in the transition between new ice and FYI, 10-30cm thick. |
| FYI | Ice of not more than one year's growth developing from young ice, thickness 30 cm to 2 m. Level when undeformed but where ridges and hummocks occur they are rough and sharply angular. |
| Fast ice | Sea ice that remains fast along the coast or over shoals. Also called landfast ice. |
| Grounded ice | Floating ice, which is aground in shoal water. |
| Ice field | Area of drift ice at least 10 km across. |
| Pancake ice | Pieces of new ice usually approximately circular, about 30 cm to 3 m across, and with raised rims due to the pieces striking against each other. |
| Ice floe | Any relatively flat piece of ice 20m or more across. |

| | |
|---------------|--|
| Level ice | Sea ice which is unaffected by deformation; a substitute term is undeformed ice. |
| Deformed ice | A general term for ice that has been squeezed together and in places forced upwards and downwards; a substitute term is pressure ice. |
| Rafted ice | A form of pressure ice in which one floe overrides another. A type of rafting common in nilas whereby interlocking thrusts are formed-each floe thrusting "fingers" alternately over and under the other-is known as finger rafting. |
| Brash ice | Accumulations of ice made up of fragments not more than 2 m across, the wreckage of other forms of ice. |
| Hummocked ice | A form of pressure ice in which pieces of ice are piled haphazardly, one over another, to form an uneven surface. |
| Ridge | A ridge or wall of broken ice forced up by pressure; the upper (above water level) part is called sail and the lower part keel. |
| Fracture | Any break or rupture in ice resulting from deformation processes, length from meters to kilometers. |
| Crack | Any fracture that has not parted more than one meter. |
| Lead | Any fracture or passageway through sea ice which is navigable by surface vessels. |

2.4 Arctic sea ice (Alaska coast- Chukchi and Beaufort Seas)

Arctic sea ice is divided into two types: 1) seasonal ice or FYI, 2) perennial or MYI (Wadhams 2000). By beginning of satellite observations (1979), Arctic sea ice extent decreased a lot and this decline has accelerated from the early 2000s (Heo et al. 2021). In 2007 and 2012, sea ice extent reached to a record-breaking minimums during summer season (Overland et al. 2012).

The Chukchi and Beaufort Seas are located in the north of Alaska and are limited by U.S., Russian and Canadian coasts (Mahoney 2012). Both seas are different in bathymetry, ocean circulation, latitude, the alignment of the coast, and the dominant wind direction. Therefore, different sea ice regimes are found in these seas (Mahoney 2012). The most part of the Chukchi Sea is dominated by a wide and shallow shelf, the Chukchi Shelf, less than 50 m deep with shoals like Hanna Shoal and Herald Shoal rising to around 20 m (Mahoney 2012; Mahoney et al. 2014). Inversely, only a narrow coastal area (less than 100 km) is captured by water shallower than 50 m in the Beaufort Sea, and most of the basin is deeper than 1000 m and belongs to the Canadian Basin (Mahoney 2012; Mahoney et al. 2014). The Chukchi Sea is located farther south from the Beaufort Sea. It is linked to the Pacific Ocean by the Bering Strait where a net northward transport of heat results in increasing the early loss of ice (Woodgate et al. 2010). Therefore, this causes a later freeze-up and an earlier sea ice retreat in spring in the Chukchi Sea (Mahoney 2012). Conversely, circulation in the Beaufort Sea is controlled by the clockwise motion of the Beaufort Gyre (Mahoney 2012). This circulation transfers MYI from the north of the Canadian archipelago into the Beaufort Sea. Therefore, there is a perennial ice cover in the Beaufort Sea whereas, in general, the Chukchi Sea is covered with new-grown sea ice each year (Mahoney 2012).

SLIE (Seaward Landfast Ice Edge) usually faces drift ice but sometimes open water. There are no leads at the landfast ice edge in much of the Beaufort Sea (Mahoney 2012). Since the landfast ice zone is stable, so it is a proper habitat for ringed seals and polar bears by producing denning areas and access to prey (Laidre et al. 2008). Additionally, landfast ice is a platform for hunting and traveling for Arctic coastal communities (George et al. 2004). Landfast ice in the Beaufort Sea is used for ice roads to access drilling platforms (Potter et al. 1981; Masterson 2009). Landfast ice in the Chukchi and Beaufort Seas is a seasonal phenomenon which gradually advances from the coast in late fall or early winter (October–November). Then, it retreats rapidly in May–June (Mahoney 2012; Mahoney et al. 2014). The horizontal extent of landfast ice is closely related to bathymetry (Zubov 1945; Mahoney 2012). The modal water depth at SLIE in the Beaufort and the northern Chukchi seas is between 16 m and 22 m (Mahoney et al. 2007a). Therefore, the 20 m isobath is a reasonable approximation of the average stable extent of landfast ice, although landfast ice can extend to deeper waters for short periods based on atmospheric and oceanic conditions (Zubov 1945; Mahoney et al. 2007a; Mahoney 2012). The spatial and temporal variability of landfast sea ice retrieved from a 10-month satellite imagery on the Alaska coast are presented in Figure 3.

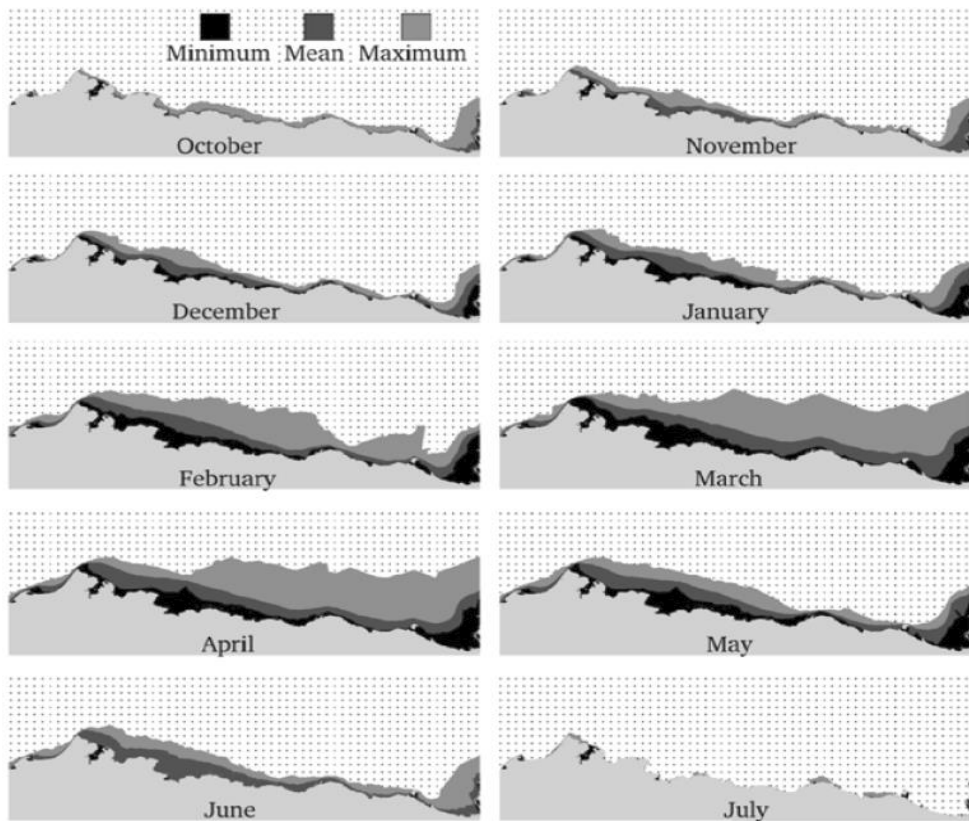


Figure 3. Monthly minimum, mean, and maximum landfast sea ice extents in the eastern Chukchi and western Beaufort seas. The dotted area indicates where landfast ice was never observed (Mahoney et al. 2007a).

Landfast ice formation starts in lagoons and sheltered embayments. Then, landfast ice can expand by grounded ridges to deeper water and remain stable (Mahoney et al. 2007b), which almost draws the relationship between the extent and the bathymetry. The availability of such ridges restricts the timing of stabilization because ridges created from thin, young ice tend to have shallower keels than ridges created from thicker ice (Amundrud et al. 2004). In a study by Mahoney et al. (2007a), it was shown that landfast ice in northern Alaska formed later and broke up earlier during the period 1996–2004 than during the 1970s (Barry et al. 1979).

3 Microwave remote sensing of sea ice

Microwave remote sensing uses radio waves with wavelengths approximately between 1 cm-1 m. It provides observations in day and night and under almost all weather conditions, including cloud cover and even rain. Microwave remote sensing can be divided into two main categories: passive sensors (for example radiometers) and active sensors (for example radars and scatterometers) (Figure 4). Active sensors equipped with transmitters for illuminating the target, and they can be divided into five classes, including SAR systems, SLAR (Side-Looking Airborne Radar), scatterometers, altimeters, and meteorological radars. SAR sensors use synthetic-aperture antenna-processing techniques, whereas the other sensors use real-aperture imaging techniques. (Ulaby et al. 2014)

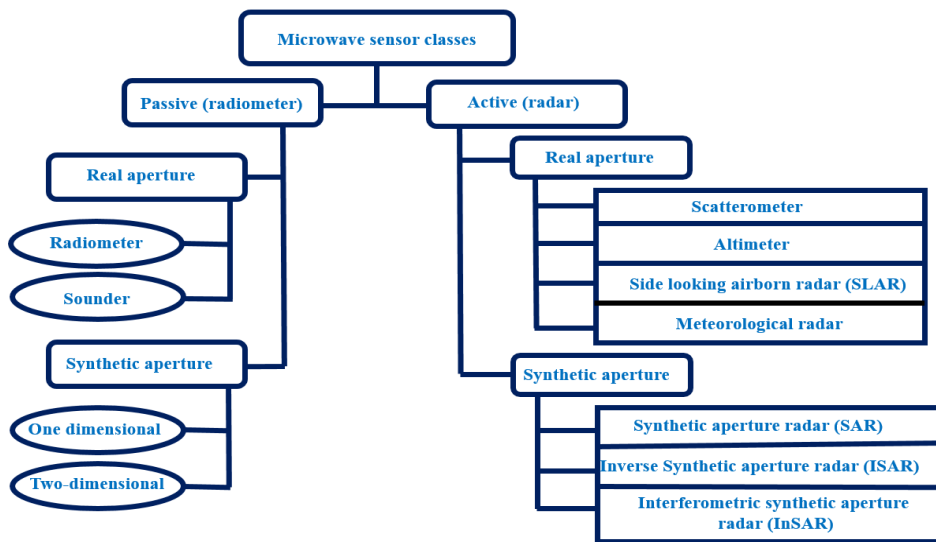


Figure 4. Classification of microwave remote sensing sensors. The figure is modified from (Ulaby et al. 2014).

3.1 Microwave radiometers

Microwave radiometers are passive microwave instruments, widely used for sea ice observations. Multiple satellite microwave sensor families offer long-term measurements from the 1970s up to now. These sensors detect the microwave radiation that is naturally emitted by the Earth. The intensity of emitted microwaves varies due to temperature and different emissivity of target materials. The emissivity of sea ice is influenced by the physical composition of ice and properties such as salinity, surface roughness, moisture contents, and crystalline structure. Ice crystals have typically higher emissivity than open water in the microwave region and therefore sea ice appears brighter to the sensor. (Shokr and Sinha 2015) Passive microwave observations have typically coarse resolution around 30-50 km (for higher frequencies up to 5 km) and are suitable for large-scale monitoring rather than for local observations (Ulaby et al. 2014).

3.2 Active microwave sensors

In active microwave remote sensing, sensors send microwaves signals toward the Earth's surface and then detect the backscattered and reflected signals from the surface (Ulaby et al. 2014). The backscatter intensity from sea ice depends mainly on sea ice roughness, but also on salinity, temperature, snow layers and presence of liquid water (e.g. Askne et al. 1992). Strong backscatter intensity is produced by rough surfaces or from a volume that has numerous scattering elements (Shokr and Sinha 2015). Three types of active microwave sensors are used in sea ice applications: imaging radar such as SAR, profile radar or scatterometer, and radar altimetry (Shokr and Sinha 2015).

Scatterometer

A scatterometer is a type of active microwave radar which measures the amount of reflected energy, or backscatter intensity, from the Earth's surface

(Ulaby et al. 2014). The backscattered signals are related to the surface size and properties like roughness (Ulaby et al. 2014). Data retrieved by spaceborne scatterometers are used to assess sea-ice extent directly by performing statistical discrimination of sea ice (Onstott 1992). Originally, the satellite-borne scatterometer was designed to measure the surface wind speed and direction over the ocean, but later, the usefulness in extracting sea ice information on a daily time scale with coarse resolution (25–50 km) was proved (Shokr and Sinha 2015). Scatterometers measure the radar backscatter very precisely. Their disadvantage in comparison with imaging radars is that scatterometers have lower spatial resolution data (Ulaby et al. 2014). Table 2 presents a list of several scatterometer sensors.

Table 2. List of several scatterometers.

| Sensor (operator) | Platform | Band | Temporal coverage | Resolution |
|-------------------|--------------------------|-----------------------|-------------------|---|
| SeaWinds (NASA) | QuikSCAT | Ku-band (13.4 GHz) | 1999-2009 | Best quality: 50 km Standard quality: 25 km Basic sampling: 12.5 km |
| OSCAT (ISRO) | OceanSat-2,3A, ScatSat-1 | Ku-band (13.4 GHz) | 2009-now | 25 km, or 50 km (for best quality data) |
| SCAT (CNSA) | CFOSAT | Ku-band (13.256 GHz), | 2018-now | High quality data: 50 km. Basic sampling: 10 km. |

Altimeters

Altimeters are simple radars which send a pulse of radiation to the Earth's surface and measure the time that it takes to return to the radar. The pulse's round-trip time shows the distance from the radar to the surface. The accuracy is on the order of 1 cm. (Ulaby et al. 2014)

Spaceborne altimeters have been used to measure the thickness of ice sheets, but their abilities were expanded to also measure sea ice and snow thickness. Another type of altimeter is a laser altimeter (laser pulses). Radar signals can penetrate into dry snow, and then the radar altimeter receives the signal that is reflected from the sea ice surface, but the laser altimeter receives the signal back from the top of the snow cover. Radar altimeters were used in some satellites like ERS-1 (European Remote sensing Satellite-1), ERS-2, and ENVISAT (Environmental Satellite) but their orbits were not optimized for sea ice observation. A dedicated satellite for ice remote sensing, CryoSat-2, was launched in April 2010 designed to detect sea ice cover and ice sheets over polar areas. The highest ground resolution was achieved with SAR mode by 250 m resolution with a swath width of 250 km. The first laser altimeter called GLAS (Geoscience Laser Altimeter System) was launched onboard ICESat (Ice, Cloud and land Elevation Satellite) (launch: 2003 - end: 2010). Surface elevation of FYI and MYI were provided from 2003 to 2009. The second generation of the orbiting laser altimeter ICESat-2 was launched in 2018 for measuring polar ice sheet elevation and sea ice freeboard. (Shokr and Sinha 2015)

Imaging radar

The purpose of imaging radar systems is generation of images using the radar backscatter from illuminated areas. Radar systems used for remote sensing fall into broad categories: imaging radars (SAR and SLAR), and nonimaging radars such as most scatterometers, altimeters, and meteorological radars. Two different types of SLAR are considered: real aperture SLAR and SAR. The difference between SLAR and SAR is how they form the image. The SLAR uses real aperture to form an image and the SAR synthesizes multiple measurements to one long virtual antenna. Airborne and spaceborne imaging

radars in remote sensing have several applications including geology, hydrology, agriculture, forestry, cartography, cryosphere, and oceanography. (Ulaby et al. 2014)

In real aperture systems, the along-track resolution is proportional to the product of the antenna beamwidth and the distance to the object. Therefore, the resolution changes with cross-track distance, and to achieve a high resolution, large antennas must be used. SAR systems were developed to overcome this problem. SAR resolution in the along-track direction is proportional to the length of the synthetic antenna and does not depend on the distance. SAR achieves high along-track resolution by combining data collected from multiple antenna positions to synthesize a longer effective antenna. (Ulaby et al. 2014)

SAR images are provided in resolution up to 1 m or even higher, depending on their acquisition mode. Normally, achieving a higher resolution or multi-polarization capability comes at the expense of losing the image coverage. The SAR imagery can be used to derive information on ice type, ridges and leads, and can be used to identify and trace individual ice floes from consecutive SAR images to produce ice motion maps (Askne et al. 1992; Sandven and Johannesen 2006; Shokr and Sinha 2015). Common SAR bands are X-band (9.4 GHz, 3.2 cm), C-band (5.3 GHz, 5.7 cm) and L-band (1.3 GHz, 24 cm) (Ulaby et al. 2014). Tables 3 and 4 give an overview of past and current space-borne SAR sensors used for sea ice applications.

Table 3. Past SAR sensors suitable for sea ice observation.

| Sensor (operator) | Platform | Polarization | Temporal coverage | Resolution |
|-------------------|-------------|----------------|-------------------|---|
| L-BAND | | | | |
| SAR (NASA) | SeaSat | HH | 1978 | SM mode: 25 m |
| PALSAR (JAXA) | ALOS | HH, VV, HV, VH | 2006-2011 | Fine mode: 7-44 m Fine mode: 14-89 m ScanSAR mode: 100 m Polarimetry mode: 24-89 m |
| SAR (JAXA) | JERS-1 | HH | 1992-1998 | 18 m |
| C-BAND | | | | |
| AMI-SAR (ESA) | ERS-1 | VV | 1991-2000 | IM mode: 30 m WV mode: 30 m |
| AMI-SAR (ESA) | ERS-2 | VV | 1995-2011 | IM mode: 30 m WV mode: 30 m |
| SAR (CSA) | RADAR SAT-1 | VV | 1995-2013 | Standard mode: 25 m Fine mode: 10 m ScanSAR wide mode: 100 m ScanSAR narrow mode: 50 m Polarimetric standard mode: 25 m Polarimetric fine mode: 10 m Multi-look fine mode: 10 m Ultra-fine mode: 3 m |
| SAR (CSA) | RADAR SAT-2 | HH, VV, HV, VH | 2007-today | Standard mode: 25 m Fine mode: 10 m ScanSAR wide mode: 100 m ScanSAR narrow mode: 50 m Polarimetric standard mode: 25 m Polarimetric fine mode: 10 m Multi-look fine mode: 10 m |

| | | | | |
|---------------------|--------------------------|-------------------|---------------|--|
| | | | | Ultra-fine mode: 3 m |
| ASAR (ESA) | ENVISAT | HH, VV, HV, VH | 2002- 2012 | IM mode: 30 m AP mode: 30 m WS mode: 150 m GM mode: 1km WV mode: 10m |
| SAR-C (ISRO) | RISAT-1 | HH, VV, HV, VH | 2012- 2017 | HRS mode:1 m FRS-1 mode: 3 m FRS-2 mode: 9 m MRS mode: 25 m CRS mode: 50 m |
| X-BAND | | | | |
| SAR (Bundeswehr) | SARLup e1,2,3,4, 5 | | 2006 | less than 1 meter |

Table 4. Current SAR sensors suitable for sea ice observation.

| Sensor (operator) | platform | Polarization | Temporal coverage | Resolution |
|----------------------|-------------------------|-------------------|----------------------|--|
| L-BAND | | | | |
| PALSAR-2 (JAXA) | ALOS-2 | HH, VV, HV, VH | 2014-now | SPOT mode: 1-3 m SM (ultra-fine) mode: 3 m SM (high-sensitive) mode: 6 m SM (fine) mode: 10 m ScanSAR mode: 100 m |
| SAR-L (CONAE) | SAOCOM-1,2-A, B | HH, VV, HV, VH | 2018-now | SM mode: < 10 m TopSAR narrow mode: < 30 m TopSAR wide mode: < 50 m, < 100 m |
| C-BAND | | | | |
| SAR-C (ESA) | Sentinel-1A/B/C/D | HH, VV, HV, VH | 2014-now | SM mode: $4 \times 5 \text{ m}^2$ ScanSAR (IW) mode: $5 \times 20 \text{ m}^2$ ScanSAR (EW) mode: $25 \times 80 \text{ m}^2$ WV mode: $20 \times 5 \text{ m}^2$ |
| X-BAND | | | | |
| SAR-X (DLR) | TerraSAR-X, TanDEM-X | HH, VV, HV, VH | 2007-now | SPOT mode: 1 m SM mode: 3 m ScanSAR mode: 16 m |
| SAR-2000 (ASI) | CSK-1,2,3,4 | HH, VV, HV, VH | 2007-now | SPOT mode: 1 m SM HIMAGE mode: 3 m |

| | | | | |
|-----------------------|------------------------------------|----------------|----------|--|
| | | | | ScanSAR wide swath mode: 30 m ScanSAR huge swath mode: 100 m SM ping-pong mode: 15 m |
| CSG-SAR (ASI) | CSG-1,2 | HH, VV, HV, VH | 2019-now | SPOT mode: $0.50 \times 0.35 \text{ m}^2$; $0.63 \times 0.63 \text{ m}^2$ SM mode: $3.0 \times 3.0 \text{ m}^2$ ScanSAR mode: $4 \times 20 \text{ m}^2$; $6 \times 40 \text{ m}^2$ |
| SAR-X (CDTI) | SEOSAR/Paz | HH, VV, HV, VH | 2018-now | SPOT mode: 1 m SM mode: 3 m ScanSAR mode: 16 m |
| ICEYE SAR (ICEYE) | ICEYE X1, X2, X4, X5 and follow on | VV | 2018-now | SM:2.5-3.0 m SPOT:0.2-1.0 m |
| COSI (KARI) | KOMPSAT-5,6 | HH, VV, HV, VH | 2014-now | SPOT mode:1 m SM mode: 3 m ScanSAR mode: 20 m |
| Capella SAR (Capella) | Capella | HH | 2019-now | SPOT mode:0.3 m SITE mode: 0.3 m SM mode: 0.3 m |
| SAR-X (ISA) | RISAT-2 | HH, VV, HV, VH | 2009-now | SPOT mode: $\leq 1 \text{ m}$ Super-ST mode:1.8 m SM mode:3 m ScanSAR mode: 8 m |
| S-BAND | | | | |
| SAR-S (UKSA) | NovaSAR-S | HH, VV, HV, VH | 2018-now | ScanSAR mode: 20 m Maritime Surveillance: 30 m SM mode: 6 m ScanSAR Wide mode: 30 m |
| SAR-S (CAST) | HJ-1C | HH,VV | 2013-now | SM mode: 5 m (single look) ScanSAR mode: 20 m (4 looks) |

Overall, optical instruments are not well-suited for polar or sub-polar regions because of cloud cover and polar night, and microwave radiometers are limited by the coarse spatial resolution. Currently, only SAR systems can overcome these problems. SAR systems have been used to monitor lake ice, sea ice,

glaciers and ice sheets. In operational services, SAR images are used for sea ice mapping and iceberg tracking in the polar regions. (Ulaby et al. 2014).

Several national institutes produce daily sea ice charts based on a combination of satellite imagery and in situ data. Ice charts generated by FIS include ice cover with polygons to which ice types and properties are assigned. A visual interpretation of SAR imagery is the principal source of ice information. Nowadays, RADARSAT-2 and Sentinel-1 C-band SAR images in ScanSAR Wide Swath Mode are acquired for this work (Berglund and Eriksson 2015).

Supporting datasets are visible and thermal infrared imagery, in particular MODIS (Moderate Resolution Imaging Spectroradiometer), surface sea ice information is reported by icebreakers and fixed observation sites as well as estimated by sea ice models. The sea ice area polygons are defined by sea ice experts. The parameters describing the sea ice properties in these polygons are ice concentration, average thickness, maximum and minimum level-ice thickness, and DIR (Degree of Ice Ridging). In the next step, ice charts are saved by using ice-charting software in numerical grids. Their resolution is about one NM (Nautical Mile). The ice thickness, ice concentration and DIR values are included in the numerical grids. A typical polygon size is around several hundred square kilometers. (Gegiuc et al. 2018)

4 Basics of Radar, SAR and InSAR

The basic principles of radar, SAR and InSAR are shortly explained in sections 4.1 and 4.2 as related to the context of this dissertation. Phase contribution to InSAR due to topography and displacements are explained in sections 4.3 and 4.4. The interferometric processing steps are also described in 4.5. More detailed explanations can be found e.g. in (Curlander and McDonough 1991; Elachi 1988).

4.1 Radar and SAR

Radar is an electromagnetic sensor that can detect, locate and track targets (Ulaby et al. 2014). It emits electromagnetic waves towards a target and then receives echoes from it (Ulaby et al. 2014). Radar is an active system that has its own source of illumination (Skolnik 2005; Ulaby et al. 2014). It operates in the microwave range of the electromagnetic spectrum (Skolnik 2005; Ulaby et al. 2014). Figure 5a shows the configuration of a side-looking RAR (Real Aperture Radar). The radar scans the ground in two dimensions (range and azimuth). Δr is the difference in range distance and is connected to a time difference $\Delta t = \frac{2\Delta r}{c}$ (Ulaby et al. 2014), where c is the speed of light. The smallest detectable time difference is the pulse length (τ). Therefore, the smallest range distance which can be resolved between the point targets is (Ulaby et al. 2014; Krieger et al. 2010):

$$X_r = \frac{c\tau}{2} = \frac{c}{2B_{rg}}, \quad (2)$$

where X_r is the slant range resolution and B_{rg} is the system bandwidth. The ground range resolution is defined as the minimal distance between two points

on the terrain and is given by $X_{gr} = \frac{c\tau}{2\sin\theta}$ (Ulaby et al. 2014). Azimuth resolution shows a sensor ability that separates two closely spaced scatterers in the direction parallel to the motion vector of the sensor and it is equal to (Ulaby et al. 2014):

$$X_a = \frac{\lambda}{L_p} \cdot \frac{h}{\cos\theta} = \frac{\lambda}{L_p} r, \quad (3)$$

where $\frac{\lambda}{L_p}$ is the azimuth beamwidth, h is the height of radar above the ground, λ is the wavelength, L_p is the antenna length, r is the distance from the sensor to the target, θ is incidence angle which is the angle between the direction of incident wave and the normal to the earth ellipsoid.

To increase azimuth resolution, a large antenna with narrow beam or footprint is required (Ulaby et al. 2014). For example, for ERS-1, an azimuth resolution of the same order of the range one, i.e. 20 m at mid swath by 23° , could be achieved only with an antenna having a length of about 2374 m (Ulaby et al. 2014). Building such a big antenna in reality is not possible, thus a so-called synthetic aperture is used to increase antenna length and azimuth resolution using advanced radar signal processing (Ulaby et al. 2014). The SAR principle is based on coherently combining echoes from the target during the passage of the sensor (Bamler and Hartl 1998). This is schematically shown in Figure 5b, with O, A and B being target and radar positions for the first and for the last time when the target is imaged. The maximum achievable azimuth resolution with this antenna length (L_S) is equal to (Ulaby et al. 2014):

$$X_{a,SAR} = \frac{\lambda}{2L_S} r = \frac{L_p}{2}. \quad (4)$$

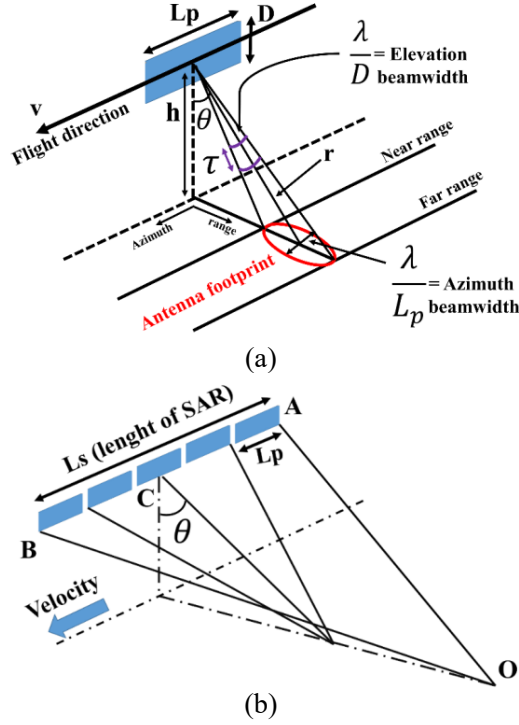


Figure 5. (a) The configuration of a real aperture, side-looking radar. (b) The principle of synthetic aperture radar. L_p , θ , h , r , λ , τ are the antenna length, incidence angle, height of radar above the ground, the distance from the sensor to the target, the wavelength and pulse length. The figures are modified from (Ulaby et al. 2014).

4.2 Interferometric SAR concepts

Every element of a complex SAR data contains two types of information, one of them is the signal amplitude A and the other one is its respective phase φ . The signal amplitude is a measure of the amount of energy reflected back from an object to the radar and is a function of the roughness of the observed object, the orientation of the area with respect to the look direction of the radar, and the dielectric properties of the material. The signal phase φ , modulo 2π , is a measure of the two-way distance from the sensor to a target on the ground. The phase of a SAR image is a random function of position due to variation

in the distance and reflective properties of each target at subpixel level. However, if two images are acquired from almost identical vantage points (requirement of InSAR approach), then the phase difference $\Delta\varphi$ between the two images shows information about surface topography and displacement although other phase contributions are also present. Some of these contributions need to be removed based on specific purpose of processing such as, e.g., topography or displacement. (Ulaby et al. 2014)

To extract $\Delta\varphi$, an interferogram I is formed via cross-multiplication of two co-registered complex SAR images C_1 and C_2 (Ulaby et al. 2014):

$$I = C_1 C_2^* = A_1 A_2 e^{j(\varphi_1 - \varphi_2)}, \quad (5)$$

where $C_1 = A_1 e^{-j\varphi_1} = A_1 e^{-j\frac{2p\pi}{\lambda}r}$, $C_2 = A_2 e^{-j\varphi_2} = A_2 e^{-j\frac{2p\pi}{\lambda}r + \Delta r}$, $e^{(\cdot)}$ is the exponential function, and j is imaginary unit.

The interferometric phase $\Delta\varphi = \varphi_1 - \varphi_2$ can be extracted from the complex interferogram as (Ulaby et al. 2014):

$$\Delta\varphi = \arg(I) = \varphi_1 - \varphi_2 = \frac{2\pi p}{\lambda} (r - r + \Delta r). \quad (6)$$

The interferometric phase $\Delta\varphi$ can be seen as a linear combination of the following contributions (Richards 2009):

$$\Delta\varphi = \varphi_{flat-earth} + \varphi_{topo} + \varphi_{displacement} + \varphi_{atmos} + \varphi_{noise} + 2\pi n. \quad (7)$$

This can be written in more detail as (Richards 2009):

$$\Delta\varphi = \varphi_{flat-earth} + \frac{2\pi p B_{\perp}}{\lambda r \sin(\theta)} * \Delta h + \frac{4\pi}{\lambda} \Delta r_r + \varphi_{atmos} + \varphi_{noise} + 2\pi n, \quad (8)$$

where, B_{\perp} is the perpendicular baseline, Δh represents the topographic height variation, Δr_r represents the relative scatterer displacement projected on the slant range direction (Dammert et al. 1998). Factor p takes into account whether the range difference is only due to the receive path or due to both the transmit and the receive paths. Therefore, $p = 1$ for a single-pass or bistatic SAR interferometer where only one antenna transmits and two antennas receive the scattered signals (standard mode), and $p = 2$ for a repeat-pass or monostatic SAR interferometer where each antenna transmits and receives its own signal (ping-pong mode). (Moreira et al. 2013)

The monostatic and bistatic modes have advantages and disadvantages. For example, the scattered signal in bistatic mode is recorded by both antennas simultaneously. Therefore, this simultaneous recording data avoids errors due to temporal decorrelation and atmospheric disturbances, which does not happen in monostatic mode. On the other hand, in monostatic mode, the two antennas are operated independently from each other, so this results in avoiding the need for synchronization whereas synchronization is necessary in bistatic mode. (Krieger et al. 2007)

The flat earth phase, $\varphi_{flat-earth}$, is the phase contribution due to growing distance between SAR sensor and ground target that should be removed by interferogram flattening (so called-flat-earth removal). Further, the interferometric phase includes both altitude (topography) and displacement contributions. The topography phase, $(\frac{2\pi p B_{\perp}}{\lambda r \sin(\theta)} * \Delta h)$, is the topographic/altitude contribution to the interferometric phase that is used to determine elevation. If an accurate DEM is available, φ_{topo} can be computed and subtracted from the interferometric phase. The displacement phase, $(\frac{4\pi}{\lambda} \Delta r_r)$, is the surface displacement between the images. The fourth source is

atmospheric phase (φ_{atmos}). It is a phase difference between the acquisitions caused by variation in atmospheric refraction index. Compensating atmospheric phase difference variations can be based on modelling and the use of multi-baseline interferometers. φ_{noise} accounts for uncertainty in the platform positions and baseline inaccuracies resulting from phase noise in the radar system and also any change in phase between the two radar acquisitions coming from a change in pixel reflectivity (temporal decorrelation). Temporal decorrelation is an important factor that limits the usefulness of repeat pass interferometry. The last term of Equation (8) is a 2π ambiguity with all phase measurements. (Richards 2009; Rosen et al. 2000)

Any mechanism that leads to statistical differences between the signals received by the two channels can decorrelate them (Richards 2009; Ulaby et al. 2014). These mechanisms include differences in the center frequency, mis-registration between the two images in range and azimuth, and noise in the phase measurements on reception (Richards 2009; Ulaby et al. 2014). The degree of correlation, or coherence, γ , between the two constituent images C_1 and C_2 of an interferometer is measured as the magnitude of the complex cross correlation between the images (Richards 2009; Ulaby et al. 2014):

$$\gamma = \frac{|\langle C_1 C_2^* \rangle|}{\sqrt{\langle |C_1|^2 \rangle \langle |C_2^*|^2 \rangle}}, 0 \leq |\gamma| \leq 1, \quad (9)$$

where C_1 and C_2 are two complex SAR image values, and $\langle \dots \rangle$ denotes a spatial averaging operation. The coherence magnitude shows the stability of the scattering process (Rosen et al. 2000). Therefore, buildings and fixed ground have very high coherence while vegetation and changing areas have low coherence (Veci 2017). Open sea loses the InSAR coherence completely within tens of milliseconds (Bamler and Hartl 1998). The landfast ice may exhibit both relatively high and low levels of coherence depending on the

actual situation and parameters of InSAR measurement (PI). Several factors contribute to the magnitude of coherence, each attributable to a separate decorrelation mechanism. The coherence γ can be written as (Richards 2009; Ulaby et al. 2014):

$$\gamma = \gamma_{baseline} * \gamma_{volume} * \gamma_{therm_noise} * \gamma_{processor} * \gamma_{temporal}, \quad (10)$$

where baseline decorrelation $\gamma_{baseline}$ refers to mainly surface scattering signal decorrelation caused by difference in viewing angle, characterized by distance between the measurement points or baseline. In order to have correlation, the baseline has to be smaller than the critical effective baseline which will be explained in more detail in section 4.3. The baseline decorrelation, depending on baseline, is given by (Richards 2009; Ulaby et al. 2014):

$$\gamma_{baseline} = 1 - \frac{2B_{\perp} \cos \theta_l}{\lambda r \sin \theta_l} = 1 - \frac{2B_{\perp} \cot \theta_l}{\lambda r}, \quad (11)$$

where θ_l is the local incidence angle which is the angle between the direction of incident wave and the normal to the scattering surface. Under flat target assumption (such as ice), θ_l equals to θ . γ_{volume} , is caused by scattering inside a medium (Ulaby et al. 2014). Thermal noise decorrelation, γ_{therm_noise} is related to SNR (Signal to Noise Ratio) of the system and caused by thermal noise in the receiver (Richards 2009; Ulaby et al. 2014):

$$\gamma_{thermal_noise} = \frac{1}{1 + SNR^{-1}}. \quad (12)$$

Processor decorrelation, $\gamma_{processor}$ is processing decorrelation coming from errors in image interpolation, co-registration or spectral filtering. The temporal decorrelation, $\gamma_{temporal}$ in the scattering space is the decorrelation factor for incoherent changes between satellite acquisitions. Temporal decorrelation is

the main source of decorrelation in repeat-pass systems while other parameters are small. (Zebker and Villasenor 1992; Meyer et al. 2011)

In general, SAR interferometry can be employed in two different modes: across-track interferometry and along-track interferometry (Rosen et al. 2000). Besides the classification in across-track and along-track methods, SAR interferometry can also be distinguished with respect to the number of antennas on the carrier platform in single-pass and repeat-pass interferometry (Table 5) (Richards 2009).

Table 5. Types of InSAR descriptions (Richards 2009).

| Across-track interferometry | Along-track interferometry | Single-pass interferometry | Repeat-pass interferometry |
|---|---|--|--|
| The antennas are spatially arranged in a manner that a baseline component in cross-track direction is introduced. | The antennas are arranged along-track, i.e. the baseline is parallel to the flight direction. | Two (or more) antennas receive signals at the same time. So, only a single pass over an area is needed to make an interferogram. | Two radars receive signals from different vantage points at different times. |

Figure 6 shows a combination of single pass, repeat pass, across and along track baselines that are used in different studies. Applications of these techniques include extraction of DEM or topography info, and detection of displacement or change (Richards 2009; Schmitt 2014).

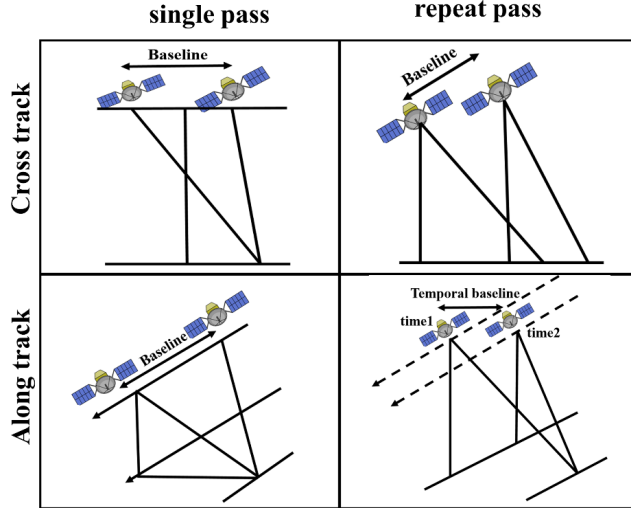


Figure 6. A combination of single pass, repeat pass, across and along track baselines in SAR interferometers. The figure is modified from (Richards 2009).

4.3 InSAR for DEM generation

The SAR sensor can be used with interferometric techniques for DEM generation using both repeat pass and across track systems (Henderson and Lewis 1998). However, the accuracy of DEMs generated by the repeat pass InSAR technique is decreased by loss of coherence due to movements of object between passes. Thus, single-pass across track is the more suitable option to derive the height surface information. Figure 7 presents a single-pass cross-track interferometer with two receivers. In case of large satellite-to-scene distances r and short baselines B_{\perp} , the measured range difference Δr will be proportional to the height difference Δh (Krieger et al. 2010). This proportionality can be expressed as (Rosen et al. 2000; Hanssen 2001):

$$\Delta r = \frac{B_{\perp}}{r \sin \theta_l} \cdot \Delta h. \quad (13)$$

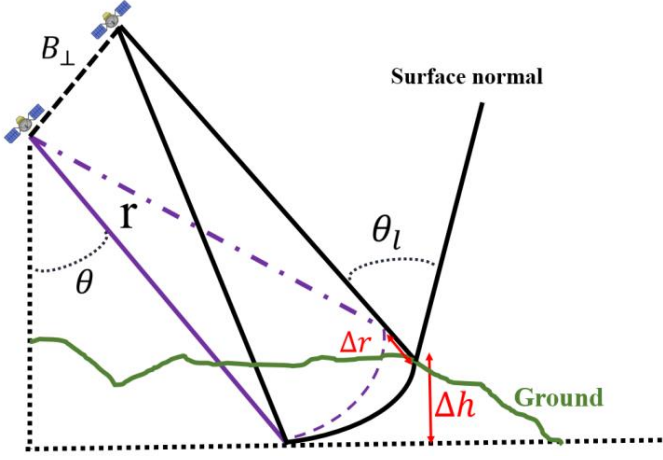


Figure 7. Across-track SAR interferometry. θ , θ_l , B_{\perp} , r , Δr , Δh are incidence angle, the local incidence angle, perpendicular baseline, the distance from the sensor to the target, difference in range distance and height difference respectively. The figure is modified from (Krieger et al. 2010).

Using the interferometric phase difference $\Delta\varphi$ given by Equation 6 (if the system is in standard mode $p = 1$ and in ping-pong $p = 2$), Equation 13 can be rewritten as:

$$\frac{\Delta\varphi}{\Delta h} = \frac{2p\pi B_{\perp}}{\lambda r \sin \theta_l}, \quad (14)$$

and the topographic phase

$$\varphi_{topo} = \Delta\varphi = \frac{2p\pi B_{\perp}}{\lambda r \sin \theta_l} \Delta h. \quad (15)$$

This equation shows the radar interferometer sensitivity to height differences Δh . It is clear that the sensitivity is increased by increasing the length of the perpendicular baseline B_{\perp} (Krieger et al. 2010). It means a high sensitivity to topography is achieved when the ambiguity height is small (Dierking et al.

2017). However, the baseline cannot be arbitrarily large and the maximum useful baseline length is constrained by two factors (Krieger et al. 2010). For the local incidence angle additional dependencies have to be taken into account (Dierking et al. 2017). The first limitation is baseline decorrelation (baseline uncertainty). When the baseline length increases, then the phase from each resolution cell will become increasingly different between two SAR images within an InSAR pair. Therefore, the correlation between the two complex SAR images decreases with increasing baseline length until it completely disappears. The corresponding baseline length is called the critical baseline $B_{\perp,crit}$ when the two SAR images become completely decorrelated. To avoid decorrelation, the baseline should be smaller than the critical baseline. For flat surfaces, this can be expressed mathematically as (Zebker and Villasenor 1992):

$$B_{\perp,crit} = \frac{\lambda r \tan(\theta_l)}{X_r} = \frac{2\lambda r B_{rg} \tan(\theta_l)}{c} = \frac{2\lambda h B_{rg} \tan \theta_l}{\cos \theta_l}. \quad (16)$$

In this dissertation, two types of satellites, namely Sentinel-1 (C-band, $B_{rg}=100$ MHz, $p=2$) and TanDEM-X (X-band, $B_{rg}=150$ MHz, $p=1$) have been used, with their $B_{\perp,crit}$ dependencies shown in Figure 8a. The second limitation of the large baseline is ambiguities in the phase-to-height conversion. Equation 15 is again considered and it shows that the interferometric measurement provides only phase values that are ambiguous by integer multiples of 2π . As a result, the height measurements are ambiguous by multiples of HoA (Height of Ambiguity) (Krieger et al. 2010; Bamler and Hartl 1998):

$$HoA = \frac{\lambda r \sin \theta_l}{p B_{\perp}}. \quad (17)$$

These ambiguities are usually resolved during phase unwrapping, which exploits spatial correlations between the height values of natural topography (Krieger et al. 2010). In addition, Figure 8b also shows HoA of both satellites versus the local incidence angles between 20 to 50 degrees.

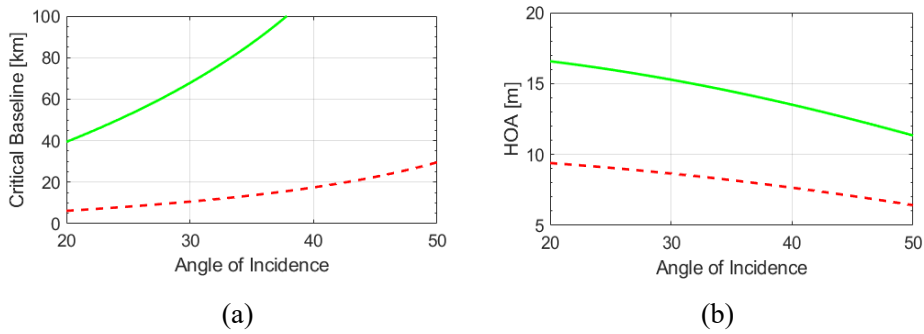


Figure 8. (a) Critical baseline and (b) ambiguous height as function of the angle of incidence for Sentinel-1 (green solid line) and TanDEM-X (red dashed line).

Optimal conditions for retrieving topography are given when two satellites fly as a tandem in close formation (Dierking et al. 2017). TanDEM-X started a new era in radar remote sensing by bringing an innovative formation flying mission (Dierking et al. 2017). The primary goal of the TanDEM-X mission is the acquisition of a global DEM with high accuracy (12 m horizontal and 2 m vertical resolution). The mission was launched in June 2010 and started operational data acquisition in December 2010 (Dierking et al. 2017). Bistatic, monostatic, and alternating bistatic operation are different types of image acquisition scenarios using the TanDEM-X and TerraSAR-X formation. The bistatic InSAR SM mode is used for operational DEM generation. In this mode, either TerraSAR-X or TanDEM-X transmits signals and then the returned signal is detected by both sensors simultaneously. Decorrelations due to temporal baseline and atmospheric disturbances are avoided (Krieger et al. 2007).

4.4 InSAR for displacement measurements

Another application of InSAR is detection of displacements between two image acquisitions. In this application, perpendicular baseline is very small or equals zero, as illustrated in Figure 9 (Richards 2009). As we see in Equation 8 the factor which contains baseline, equals to zero and thus, an interferometric phase difference is given in slant range by (Richards 2009):

$$\Delta\varphi_{change} = \frac{4\pi\Delta r_r}{\lambda}. \quad (18)$$

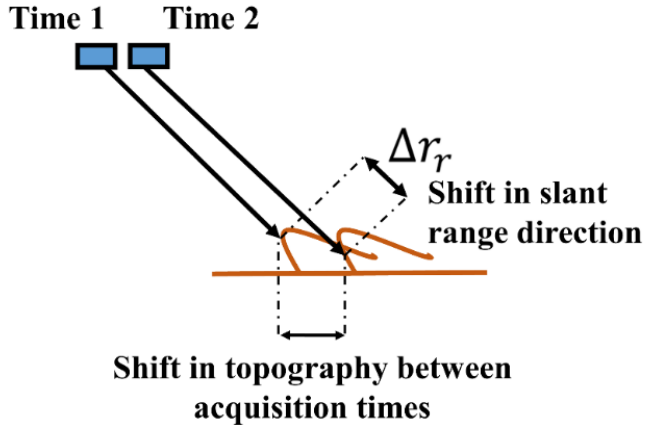


Figure 9. Measuring slant range topographic variations with repeat pass along track interferometry. The figure is modified from (Richards 2009).

Therefore, if the surface is changed even a fraction of wavelength during the time period between the two data takes, then the phase in the second image will also be shifted with respect to the first one and the shift provides an estimate of the surface displacements. (Ulaby et al. 2014) Figure 9 shows the simplest case of InSAR for displacement mapping that the perpendicular baseline equals zero. In this case, topographic mapping is not possible, as sensitivity to topographic differences is zero, and the phase difference is

caused only by surface displacements. However, there is a small perpendicular baseline in most repeat pass SAR missions that adds a very small topographic phase component info to the result. Therefore, the total interferometric phase difference is a function of both topography and displacement changes, thus (Richards 2009):

$$\Delta\varphi = \frac{2p\pi B_{\perp}}{\lambda r \sin\theta_l} \Delta h + \frac{4\pi}{\lambda} \Delta r_r. \quad (19)$$

To remove the topographic component, the DInSAR (Differential InSAR) technique (Gabriel et al. 1989) can be used in two ways (Richards 2009). First, using a pre-existing DEM to evaluate the topography part and then subtract it from the interferometric phase. The result is displacement between the SAR acquisitions. The second way is producing the second interferogram with two images taken over a time interval when no significant displacement or deformation occurred. The second interferogram is subtracted from the first one. This subtraction gives the displacement signal (Richards 2009). However, if topography is mostly flat and baseline is small, the topographic contribution to local changes is negligible.

In this context, the Sentinel-1 mission offers a good option to study displacement dynamics. It covers all the world with high resolution and dual polarization coverage over land. Each Sentinel-1 satellite has a very near-polar, sun-synchronous orbit, with a 12-day repeat cycle and 175 orbits per cycle. Both Sentinel-1A and Sentinel-1B share the identical orbit plane with a 180° orbital phasing difference. One Sentinel-1 satellite can potentially map whole Earth every 12 days. The two-satellite (Sentinel-1A and Sentinel-1B) can map with a 6-day exact repeat cycle at the equator. Since the orbit track spacing varies with latitude, the revisit rate is significantly greater at higher latitudes than at the equator. Operational modes in the Sentinel-1 mission are

SM, IW (Interferometric Wide swath), EW (Extra Wide swath) and WV modes. (User guide Sentinel-1 2021)

4.5 The interferometric processing

The mandatory steps in interferometric processing includes below steps, which can estimate interferometric phase and coherence magnitude (Interferometric SAR Processing):

- (a) Co-registration of the two complex images,

SLC (Single Look Complex) formatting products that include both master and slave images are used as input for the interferometric processing. The master and slave images do not overlap. So, a co-registration step is a strict requirement of interferogram formation and it ensures that pixels in the both master and the slave images perfectly match.

- (b) Interferogram generation,

The complex interferogram is generated from the cross-product of the co-registered SLCs. The result includes coherence magnitude (correlation between images) and InSAR phase.

- (c) Curved Earth phase removal,

In this step, the phase contribution due to growing distance between SAR sensor and ground target is removed by interferogram flattening.

- (d) Interferometric coherence estimation,

Coherence is calculated from the cross-product of the two co-registered SLCs. It provides a useful measure of the interferogram quality.

(e) Interferogram filtering,

The interferogram filtering is performed in order to reduce noise to help the phase unwrapping.

(f) Phase unwrapping,

The interferometric phase is wrapped by modulo 2π . In order to achieve the absolute phase difference, it should be unwrapped. This step is done by adding a correct multiple of 2π to the interferometric phase for each pixel.

These steps form the standard interferometric processing sequence, although, the sequences are not fully fixed and can be somewhat changed based on the interferometric products (topography or displacement measurements) and also quality of results. (Hanssen 2001; Ulaby et al. 2014; Werner et al. 2000)

4.6 Literature review in the context of the dissertation

SAR missions operating at various bands have been used for sea ice research in polar and subpolar seas such the Baltic Sea for several decades. Studied sea ice properties in the Arctic region and the Baltic Sea have included ice drift and dynamics (Leppäranta et al. 1998a; Hamidi et al. 2011; Karvonen 2012; Kwok et al. 2013; Dyrce 2020; Spreen et al. 2011; Sun 1996; Vesecky et al. 1988), sea state and wave propagation into sea ice (Liu et al. 1991; Shen et al. 2018), ice thickness (Karvonen et al. 2003, 2004; Kim et al. 2010; Nakamura et al. 2006), ice concentration and extent (Karvonen et al. 2017; Askne and Dierking 2008; Dinessen 2017), iceberg detection (Dierking and Wesche 2014), ice-type classification (Askne et al. 1992; Gegiuc et al. 2018; Soh and Tsatsoulis 1999; Soh et al. 2004; Bogdanov et al. 2005; Zakhvatkina et al. 2013; Clausi and Zhao 2002, 2003; Clausi and Yue 2004), sea ice deformation by InSAR (Dammert et al. 1998; Dierking et al. 2017; Berg et al. 2015; Dammann et al. 2017), and sea ice topography and ridges (Leppäranta and

Hakala 1992; Similä et al. 1992; Hutter et al. 2019). The focus of this dissertation is on ice-type classification and sea ice deformation using advanced SAR approaches such as the InSAR technique.

In this section, sea ice classification literature studies in the Baltic Sea using InSAR, sea ice deformation and topography in the Baltic Sea and Arctic area by the InSAR method are presented.

4.6.1 Sea ice classification studies

Ships are the primary users of sea ice charts in the Baltic Sea. FIS utilizes C-band SAR satellite images, including RADARSAT-2 and Sentinel-1 missions due to proper resolution (10-100 m) to produce ice chart maps for ship navigation (Berglund and Eriksson 2015). X-band sensors would have a better sensitivity compared to C-band sensors for assessing sea ice surface properties, small-scale surface roughness and sea ice inclusions (Ressel et al. 2015; Dierking 2013). Currently, sea ice classification and ice chart production by trained experts is laborious, time consuming and thus expensive. The same SAR data interpreted by different experts can, and often does, lead to somewhat different results. Therefore, automated classification can be a major help to solve these issues. Several studies have demonstrated the value of automatic sea ice classification using backscatter intensity data (Gegiuc et al. 2018; Clausi and Zhao 2003; Barber and LeDrew 1991; Clausi 2001) although the results are not accurate enough for practical use. Several studies have been conducted over the Baltic Sea to do sea ice classifications. An open water and sea ice discrimination algorithm for RADARSAT-1 ScanSAR images over the Baltic Sea was presented by Karvonen et al. (2005). This algorithm was based on segmentation and SAR intensity signal autocorrelation. The algorithm result was compared with results of operational digitized ice charts and showed 90% accuracy (Karvonen et al. 2005).

The type and value of edges present information on the ice types in addition to backscatter intensity values and statistics (Karvonen 2010). Karvonen (2010) used the Canny (1986) edge detection to discriminate sea ice classes by boundary selection using C-band SAR data, both RADARSAT and ENVISAT ASAR data over the Baltic Sea. The methods used in Karvonen et al. (2005) and Karvonen (2010) could distinguish between open water, various sea ice types and the areas with certain types of ice characteristics (e.g. cracks or ridges) very well. A test result for these two algorithms showed high classification accuracy (more than 89.4%) in comparison with manual sea ice maps of the Baltic Sea created by the FIS. NN (Neural Network) has been successful for algorithm developments in sea ice classification from satellite images (e.g. Heerman and Khazenie 1992; Atkinson and Tatnall 1997). Karvonen (2004) applied the pulse-coupled NN for ice edge detection, segmentation and ice classification over the Baltic Sea by using RADARSAT SAR images. New, level FYI, deformed and landfast ice were successfully classified although in some cases, there was some misclassification for thick landfast ice being classified as thin level ice (Karvonen 2004). This approach was extended by adding new data sets and modified techniques over the Baltic Sea in studies like Karvonen (2014; 2017). Karvonen (2014) developed a fully automated NN algorithm by combining of SAR segmentation data (RADARSAT-2 ScanSAR Wide mode data) and ice concentration estimates based using AMSR-2 (Advanced Microwave Scanning Radiometer 2) brightness temperature resulted in high-resolution ice concentration estimates. The concentrations are estimated by a MLP (Multi-Layer Perceptron) NN which has the AMSR-2 polarization ratios and gradient ratios of four radiometer channels as its inputs. Output results were compared with ice charts produced by FMI and high-resolution AMSR-2 ARTIST Sea Ice algorithm concentrations produced by the University of Hamburg. The differences were

on average small (Karvonen 2014). Some years later, Karvonen (2017) used another NN algorithm using Sentinel-1 SAR and AMSR-2 passive MWR (microwave radiometer) data to calculate SIC (Sea Ice Concentration) over the Baltic Sea. Input data were backscatter intensity values, several texture features, and gradient and polarization ratios of four AMSR-2. A comparison of four SIC estimation methods with reference data were presented in this study. SIC products from FMI daily ice charts were used as reference data. In addition to the combined SAR/MWR SIC estimation method, SIC estimates produced using SAR alone and two MWR-based methods have been compared (Karvonen 2017). The main goal was developing a high-resolution SIC estimation method for operational usage (Karvonen 2017). Different sea ice classes can have the same backscatter intensity, so using only a single image to do classification is insufficient (Leppäranta et al. 1992; Karvonen 2004) as indicated by Mäkynen and Hallikainen (2004) and Dierking (2010). Dierking (2010) suggested that using more image layers within higher order textural features is needed, and to train a classifier successfully a large feature space has to be created. Several previous studies have shown ability of textural information to solve uncertainties in sea ice classification (ice-water classification and multi-class sea ice type classification) (Holmes et al. 1984; Barber and LeDrew 1991; Shokr 1991; Soh and Tsatsoulis 1999; Clausi 2001, 2002; Deng and Clausi 2005). Holmes et al. (1984) studied the use of texture features in classification of sea ice types over the Beaufort Sea. The textural analysis, which included calculating the entropy and inertia of the image, indicated that first- and multiyear, smooth- and rough-ice types could be distinguished based on the textural values obtained from the data with an OA (Overall Accuracy) of 65%. Holmes also recommended combining more texture features in future research (Holmes et al. 1984). The potential of GLCM (Gray-Level Co-occurrence Matrix) for sea ice classification has been

examined and discussed by Barber and LeDrew (1991). The best sea ice discrimination was achieved when three GLCM features were used (Barber and LeDrew 1991). Several studies focusing on sea ice InSAR signatures showed that using coherence-magnitude and InSAR-phase help to explain sea ice mechanics (Dammert et al. 1998; Dierking et al. 2017; Berg et al. 2015; Laanemäe et al. 2016). Dammert et al. (1998) established relationships between backscatter intensity and coherence-magnitude features over low-salinity ice. Berg et al. (2015) further advanced understanding of the relationship between backscatter intensity and coherence. Higher coherence was observed along with high backscatter intensity at X-band, while lower coherence was detected along with high backscatter intensity at C-band (studied regions were partly overlapping) (Berg et al. 2015; Dammert et al. 1998). Therefore, coherence magnitude and backscatter intensity relationships seemed to be case dependent with several possible explanations that were explained in Berg et al (2015), although accurate field data are needed to give the interpretation.

In previous studies (e.g., Dierking et al. 2017), it has been shown that X-band InSAR-phase is suitable for mapping sea ice topography. As sea ice classes have different roughness and topography, this motivated us to study connections between backscatter intensity, InSAR coherence-magnitude, and InSAR-phase, as well as the added value of interferometry compared to using only backscatter intensity in the sea-ice classification. To date, there has been only one study over the Baltic Sea based on TanDEM-X imagery using both backscatter intensity and coherence-magnitude features for automated sea ice classification (Laanemäe et al. 2016). Their method was applied on a few sea ice classes including landfast ice, thin smooth ice, pancake ice and open water.

4.6.2 Sea ice topography studies

The landfast ice is a key component of many coastal Arctic ecosystems and provides essential services to marine biota and people (Eicken et al. 2009). Its stability has a vital role for landfast ice users and marine traffic due to the potential hazard of break-out events (Leppäranta 2013). Many factors determine landfast ice stability: ice thickness, coastal morphology, and anchoring points such as islands and grounded pressure ridges (Jones et al. 2016). Jones et al. (2016), Mahoney et al. (2007b), and Druckenmiller (2011), studied the stability of the landfast ice cover near the Utqiagvik in the context of the frictional force from grounded ridges. Many studies have been devoted to understanding of landfast ice dynamics (Dammann et al. 2019a), ridge formation (Weeks et al. 1971; Jones et al. 2016; Mahoney et al. 2007a), and impact of ridges on the traffic ability of the ice (Barker et al. 2006; Dammann et al. 2018b; Druckenmiller et al. 2013). For example, ridge height has been measured using helicopter-borne laser profilers (Dierking 1995), airborne laser scanners (Farrell et al. 2011), structure-from-motion (Dammann et al. 2018b), and spaceborne altimeters (Kwok et al. 2004). InSAR is a valuable tool for evaluation of sea ice topography and displacements from the phase difference between two scenes (Meyer et al. 2011; Dammann et al. 2016; Dierking et al. 2017). TanDEM-X is a bistatic SAR mission with no temporal baseline that has close formation (“single-pass InSAR”) to retrieve surface morphology, sea ice topography and height of grounded ridges. These data were used to evaluate surface roughness and ridge height estimation over landfast ice near Utqiagvik (Dammann et al. 2018b; Dierking et al. 2017), sea ice surface heights over fast and drifting ice in the Fram Strait (Yitayew et al. 2018), and iceberg topography in the Southern Ocean (Dammann et al. 2019b).

4.6.3 Sea ice displacement studies

Landfast ice conditions also change in the north of the Bay of Bothnia due to ice breakage and movement. Ice breakage results in sea ice bottom scouring, hazards for the coastline, man-made structures, beacons, and sea traffic. Overall, landfast ice mechanics are understood but there are details that are not clear. There are no suitable models or analysis methods about the lateral growth and deterioration of landfast ice. (Leppäranta 2013) Previous studies proved the feasibility of the InSAR technique for measurements of surface topography and displacements (Dammert et al. 1998; Meyer et al. 2011; Berg et al. 2015). The landfast ice displacements were evaluated using different bands (C, X and L) in several studies (Dammert et al. 1998; Berg et al. 2015). Dammert et al. (1998) used ERS-1 C-band SAR data to evaluate the relationships between backscatter intensity, coherence-magnitude, changes in InSAR-phase and forcing events over sea ice in the northern part of the Baltic Sea. The maximum displacement (94 cm) occurred in the ice cut off by the tracks of icebreakers. Meyer et al. (2011) mapped landfast ice extent in the Alaskan coastal zone using L-band InSAR data acquired by ALOS PALSAR with a temporal baseline of 46 days. There, both interferometric phase pattern and coherence images were used to extract the landfast ice extent (Meyer et al. 2011). Only ice that remained stationary over an entire 46-day interval was classified as landfast ice, corresponding to the minimum landfast ice extent during the observation period (Meyer et al. 2011). Regarding to checking landfast ice dynamics, we have to check coherence maps, if they have sufficient threshold of coherence and landfast ice can keep high coherence magnitude (near to one is better) then would be reliable for landfast ice edge mapping. By looking at interferograms, if landfast ice is stable enough like in case of study in Meyer 2011, you can even find deformations of up to 10 m. In a later study, Berg et al. (2015) used CSK X-band SAR data taken during

the winter of 2012 in the Baltic Sea, with a temporal baseline of one day. It was shown that some ice floes moved northward at a speed of 100 m/day, influencing and squeezing the landfast ice, in one day's time. The deformation of landfast ice in the LOS (Line Of Sight) direction was about 4.7 cm over a distance of 1800 ± 25 m (Berg et al. 2015).

5 Study areas, SAR, in situ, and validation datasets

This section introduces the study sites over the Baltic Sea and Arctic region in this dissertation. The satellite data including TanDEM-X and Sentinel-1, meteorological data, ice charts and validation datasets are described.

5.1 Baltic Sea

The study area was located near the Hailuoto island in the Bay of Bothnia, the northern part of the Baltic Sea in Finland. In PI, we selected a representative pair of Sentinel-1 IW SLC images acquired on 6 and 18 February 2015 (Figure 10a). IW swath mode includes three sub-swaths, called IW1, IW2, and IW3. A part of the IW2 sub-swath with high coherence was used in the study. Its location was between Oulu and Kemi on the Finnish coast of the Bay of Bothnia. As the landfast ice extent did not change between the two acquisitions, to present the landfast ice condition, one ice chart on 7 February was used (Figure 10b). SAR backscatter intensity images for the 6 and 18 February 2015 are presented in Figure 11. The normal (perpendicular) baseline for acquired images is 51.21 m, and incidence angle θ for IW2 is from 36.47° to 41.85° . Characteristics of Sentinel-1 interferometric are shown in Table 6.

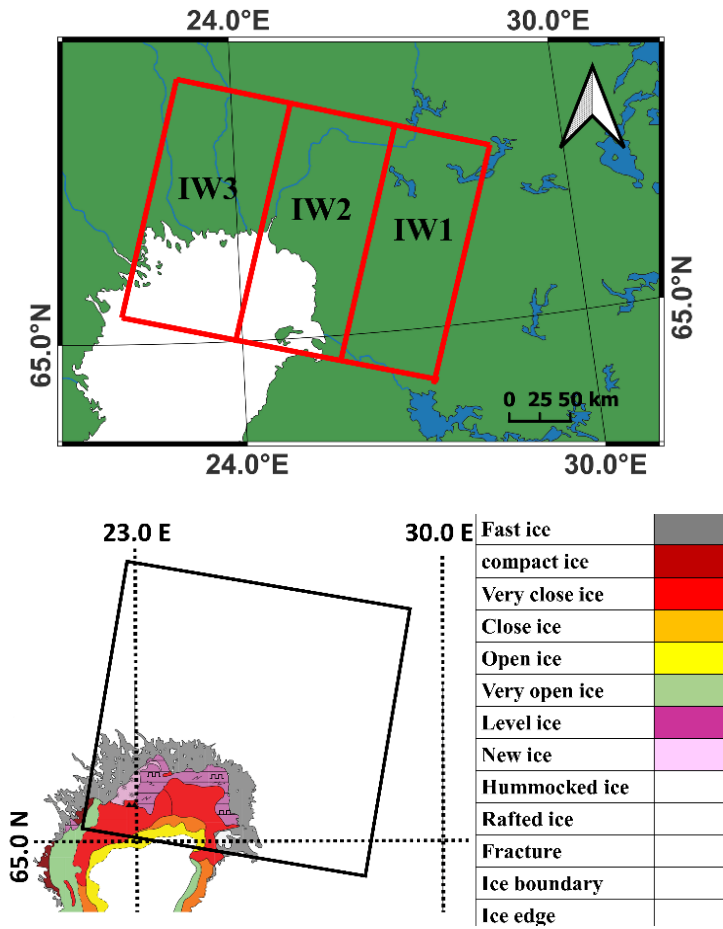


Figure 10. (a) An overview of the northern part of the Baltic Sea with IW image in PI. (b) Ice chart of 7 February 2015 for the Bay of Bothnia (FIS 2015). The SAR images cover a 250 km swath at 5 m by 20 m spatial resolution. The IW swath is marked with a square. Landfast ice is shown by the grey area. Figure adapted from PI.

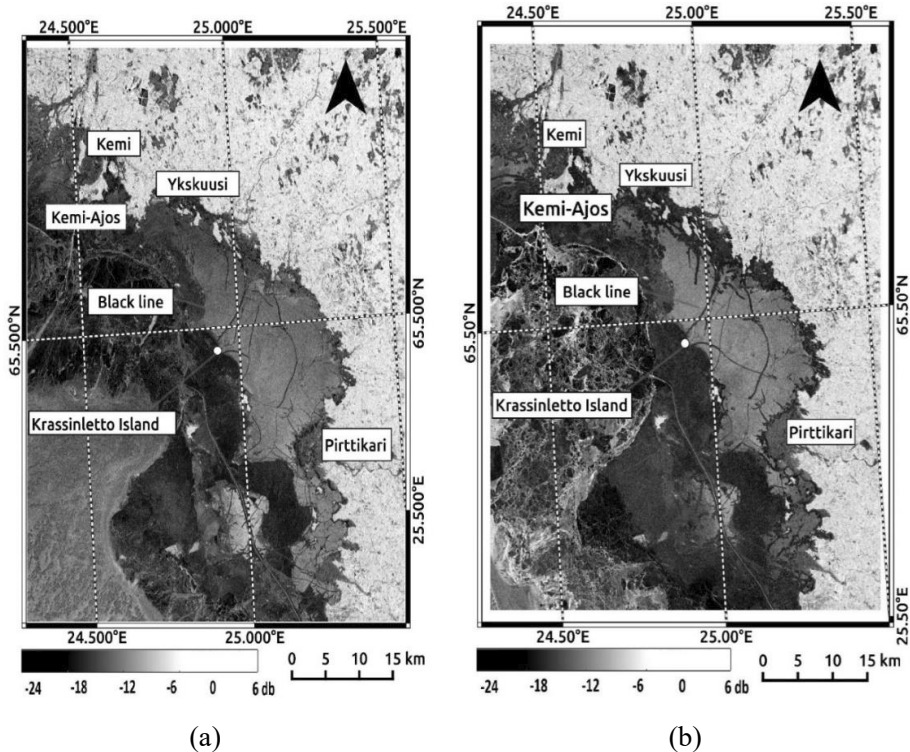


Figure 11. Backscatter intensity on 6 February (a), and on 18 February (b). Figure adapted from PI.

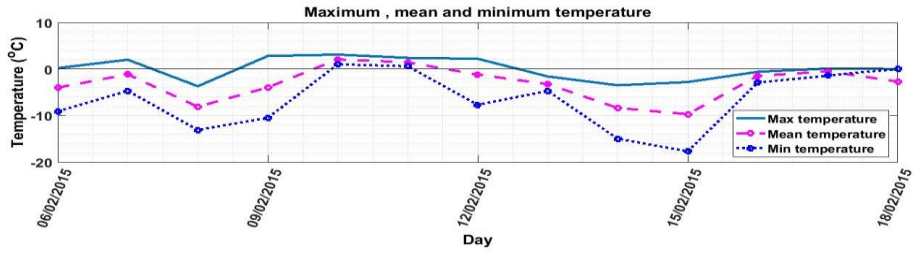
Table 6. Characteristics of Sentinel-1 interferometric mode (Torres et al. 2012; User guide Sentinel-1 2021).

| Characteristic | Value |
|--|--|
| Swathwidth | 250 km |
| Incidence Angle Range | 29.1°–46.0° |
| Sub-Swaths | 3: IW1, IW2, IW3 |
| Azimuth Steering angle | $\pm 0.6^\circ$ |
| Azimuth and Range looks | Single |
| Polarization Options | Dual HH + HV, VV + VH Single HH, VV |
| Maximum Noise Equivalent Sigma Zero (NESZ) | –22 dB |
| Radiometric Stability | 0.5 dB (3σ) |
| Radiometric Accuracy | 1 dB (3σ) |
| Phase Error | 5° |
| Spatial resolution | 5 m \times 20 m (single look) |

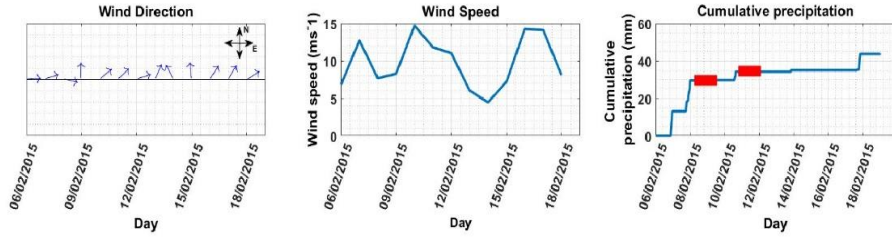
The winter 2015 was mild in the Baltic Sea. The maximum ice extent was 51,000 km² on the 23rd of January, and the whole Bay of Bothnia was then ice-covered. Sea ice formation in the innermost bays of the northern Bay of Bothnia started in the middle of November. There was 1-10 cm thick level ice in the inner archipelago at the beginning of December. Then a period of cold weather began and lasted until the 23rd of January. Another cold period occurred around the 5th of February, and the sea ice extent reached 50,000 km².

Thereafter, the weather became milder, and southerly winds pushed the ice pack toward the northeast. The rest of February was unusually mild. The ice extent was only 20,000 km² in the beginning of March. The maximum landfast ice thickness was 55 cm in the Bay of Bothnia and the drift ice thickness was 15-40 cm. (FIS 2015).

The weather information including temperature, wind direction and speed and precipitation were collected at the station Kemi harbor, Ajos (Figure 12). Two sea level stations, Kemi and Oulu provided sea level information for the period of the study. The plots are based on hourly data (Figure 13).



(a)



(b)

Figure 12. Weather information recorded by the Kemi Ajos weather station during the experiment. (a) Mean, minimum and maximum temperature information. (b) Wind direction, wind speed and cumulative precipitation information. The red squares in precipitation subfigure represent missing data (FIS 2015). Figure adapted from PI.

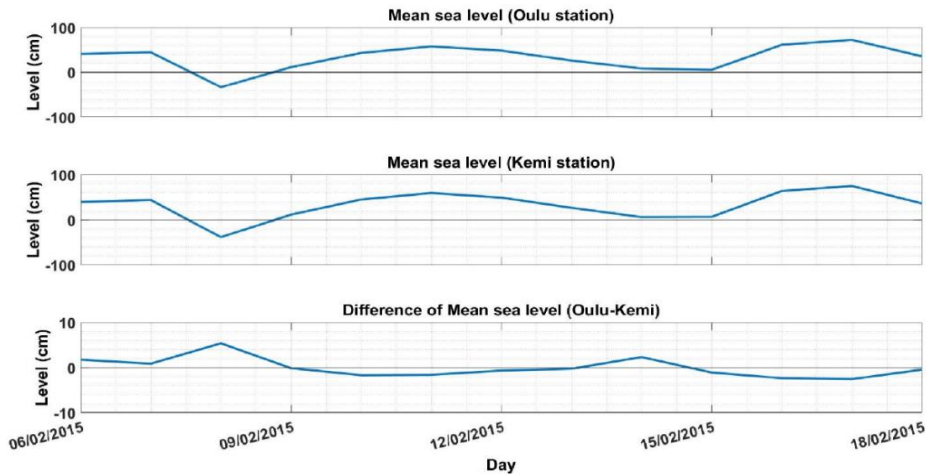


Figure 13. Sea level and sea level differences in Kemi and Oulu stations between the 6 and the 18 February 2015 (FIS 2015). Figure adapted from PI.

In PII and PIV, we investigated all TanDEM-X images between 2010 and 2019 acquired using standard bistatic imaging mode over the Baltic Sea to find a proper case of study. The best TanDEM-X data to study sea ice topography was captured in TanDEM-X Science phase between September 2014 and February 2016 due to large baselines resulting in very high sensitivity for object elevations of the order of decimeters (Maurer et al. 2016). Unfortunately, no proper data was found over the Baltic Sea in the Science phase, and we had to switch to standard operation mode with a somewhat lower topographic mapping accuracy compared to the Science phase. In PII and PIV, the data selection criteria were a nearly stable sea ice, no melting, and both sea ice and open water in the scene. This made strong limitations for the data selection. In addition, there were not many acquisitions over the Baltic Sea in comparison with the Arctic region. Finally, a bistatic CoSSC (Coregistered single-look slant-range complex) SM acquisition (TanDEM-X) in the HH polarization over the Bothnian Bay on 30th March of 2012 was taken. Figure 14a shows the TanDEM-X image footprint over the Baltic Sea on 30 March 2012.

Winter 2012 was a mild winter, but the northern and eastern basins of the Baltic Sea froze completely. The ice in the Bay of Bothnia was tightly packed to the northeast part at the end of March (Figure 14b) and the used SAR scene covered very close drift ice and landfast ice. In the frame of the study area, landfast ice thickness was 35-60 cm, and the drift ice largely included deformed ice. Weather information was recorded by the Hailuoto ($65^{\circ} 2' 23.1''\text{N}$ and $24^{\circ} 33' 40.248''\text{E}$) and Kemi Ajos ($65^{\circ} 40' 23.48''\text{N}$ and $24^{\circ} 30' 54.72''\text{E}$) stations on 30 March 2012. The daily mean temperature and wind speed were around -6.2°C , -8.2°C and 4 m/s, 2.6 m/s for the Hailuoto and Kemi Ajos stations respectively. (FIS 2012)

SAR backscatter intensity image of the 30 March 2012 is presented in Figure 15 and image parameters of the studied CoSSC scene are shown in Table 7.

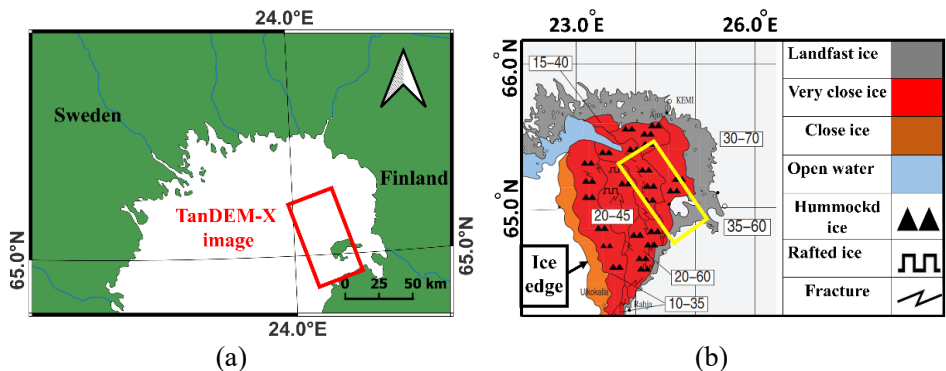


Figure 14. (a) An overview of the Bay of Bothnia with TanDEM-X image footprint shown with red rectangle. The image was acquired on 30 March 2012. (b) Ice chart over the Bay of Bothnia on 30 March 2012. The yellow rectangle shows the TanDEM-X footprint. Figure adapted from PIV.

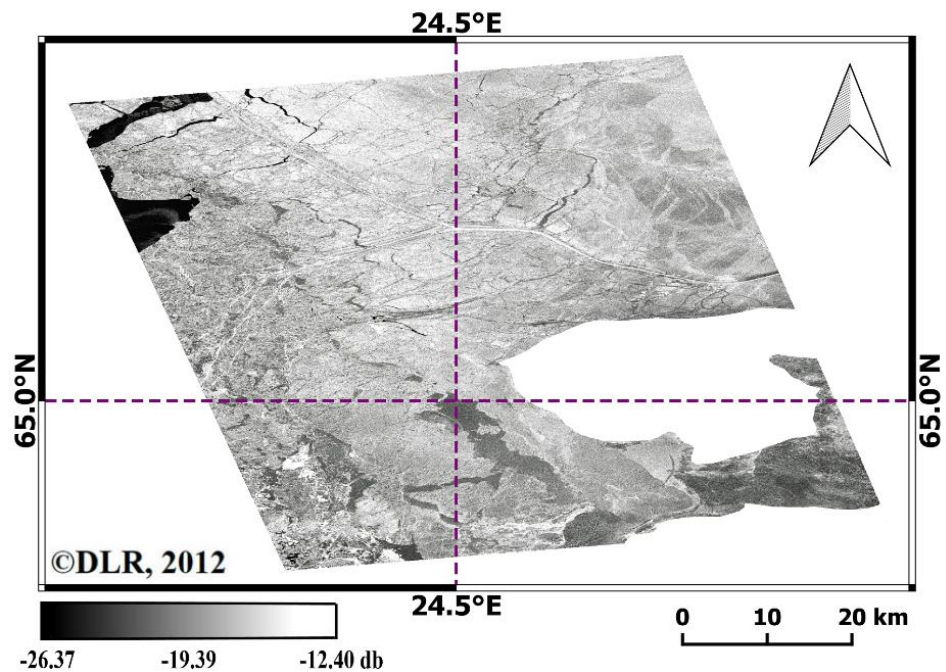


Figure 15. Backscatter intensity value on 30 March 2012 (one image from bistatic pair is shown here).

Table 7. TanDEM-X image parameters acquired on the 30 March 2012.

| | |
|------------------------|-------------|
| Acquisition date | 30 Mar 2012 |
| Acquisition start time | 15:55:37 |
| Mode | SM |
| Polarization | HH |
| Orbit cycle | 167 |
| Relative orbit | 24 |
| Effective baseline (m) | 240.38 |
| Resolution (m) | 2.51 |
| HoA (m) | -30.84 |
| Average coherence | 0.81 |
| Incidence angle (o) | 43.41 |

In PII and PIV, the operational ice chart presented in Figure 14b was not detailed enough for our study. So, an independent high-resolution reference ice chart (Figure 16) was prepared by a sea ice expert in FMI ice service based on TanDEM-X features (backscatter intensity, interferometric coherence magnitude, and interferometric phase) which are not used in operational ice charting by FIS. Adding TanDEM-X features to operational ice charting can help experts to make more accurate ice charts and also distinguish ice ridges, heavily deformed ice and new ice formation. Two different sea ice type classifications (Figure 16 and Table 8) were used in PII and PIV. In PII, the goal was to assess ice properties on the scale used in ice charting, with ice types based on ice concentration and sea ice morphology, while in PIV, a detailed small-scale analysis of sea ice properties for the sea ice classification was performed. The reference chart in PII is a standard ice chart which is prepared manually by sea ice expert, and the reference chart in PIV is also a

standard ice chart but with small-scale structures in the ice cover also illustrating the history behind the ice situation. Sea ice classes in the reference maps (Figure 16) based on the TanDEM-X products were somewhat different from the sea ice types in ice charts by FIS. However, the properties chosen to characterize the ice situation were connected to ice charting in both publications. Table 8 shows the relation between sea ice classes used in daily FIS ice charts and sea ice classes used in PII and PIV.

Table 8. Connection between sea ice classes used in daily FIS ice charts and sea ice classes used in PII and PIV.

| Ice chart | PII | PIV |
|---|--|---|
| Open water | Open water | Open water |
| New ice | New ice | New ice |
| Level ice (undeformed ice) | Thin smooth ice | Thick level ice, Undeformed ice |
| Landfast ice | not included since fast/non-fast ice could not be identified | |
| Brash ice | Ship track | Brash ice |
| Ridged ice | Ridged ice, heavily ridged ice | Moderately deformed ice, ridged ice |
| Rafted ice | not present in the ice situation | |
| Features -fractures -strips and patches -floe-bit, floeberg | Could be recognized but not included in the study | |
| Ice concentration A -close ice A = 7 – 8/10 -very close ice A = 9 – 9+/10 | -close ice, -very close ice | Because of the small pixel size ice concentration is not well defined and open water class is sufficient. Rather close and very close ice were replaced by ice quality. |

In both publications, TanDEM-X features were used by sea ice experts to produce the reference maps of sea ice classes (Figure 16).

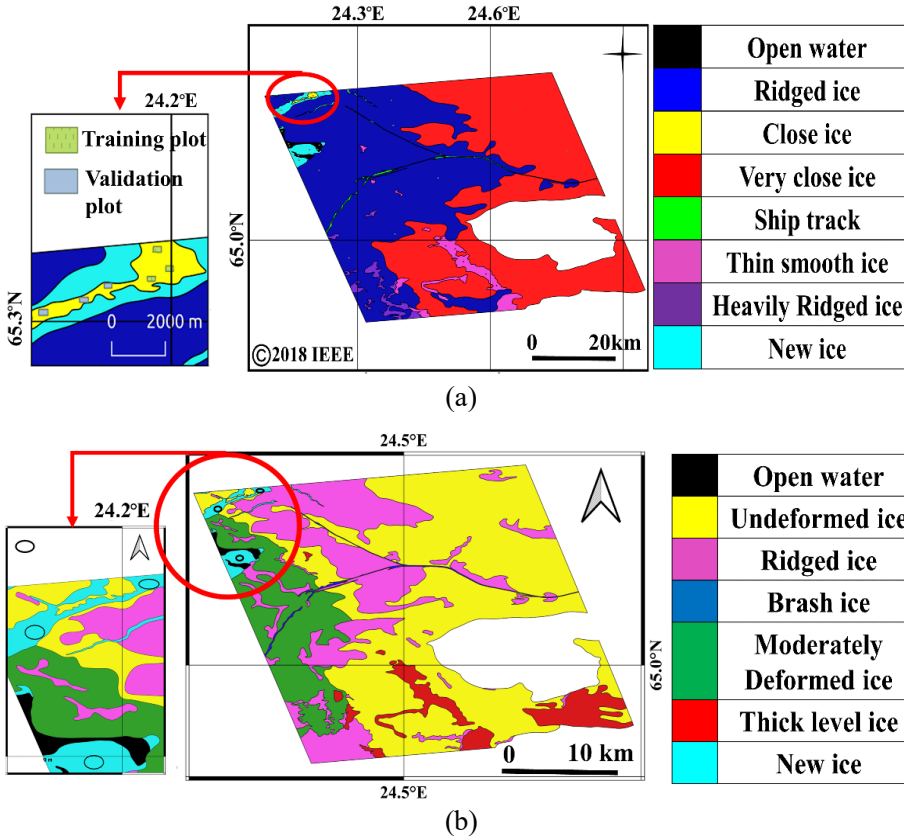


Figure 16. Reference classification map for 30 March 2012 in (a) PII (b) PIV. New ice class with training plots are shown in the left side of the image. Figures adapted from PII and PIV.

5.2 Arctic region

The focus of PIII was the landfast ice near Utqiagvik, Alaska on the coast of the Beaufort Sea. The study site and the mass balance site which have monitored landfast sea ice properties and relevant environmental conditions for over a decade are shown in Figure 17. The lack of larger baselines to achieve smaller HoA as in PII and PIV also made it difficult to select a proper dataset for ridge assessments over the Arctic sea ice. In this study, to evaluate ridge formation and movements, two bistatic CoSSC SM acquisitions (TanDEM-X) with HH polarization in the standard operation mode on 13 and

24 January 2012 with a repeat interval of 11 days were used. Sea ice thickness measurements were made by an auger on 9, 11, and 12 January, resulting in values between 0.86 and 1.02 m. The air temperature was between -13°C and -38°C for 13–24 Jan 2012. The wind direction was regularly toward the coast. The wind speed was between 3 and 12 m/s based on measurements by NWS (National Weather Service) in Barrow. No snow accumulation was recorded during the study period at the mass balance site.

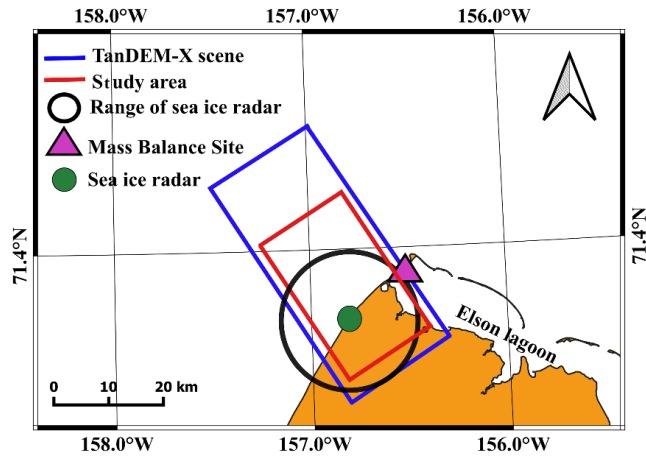


Figure 17. Study area with the TanDEM-X scene outlined in blue. The subset used (i.e. study area) is marked with a red rectangle. The black circle indicates the nominal range of the sea ice radar. Land is masked out in orange. Figure adapted from PIII.

The results were compared and validated with backscatter intensity data, coastal radar data, and SAR-derived ice drift. The backscatter intensity depends on the sea ice surface characteristics including the dielectric properties and surface roughness (Askne et al. 1992; Onstott 1992). Therefore, ridges were detectable in the backscatter intensity data and were used to do comparisons in the study. The coastline area was monitored every five minutes by a marine radar (Furuno FAR-2127 25 kW, X-band (3 cm, 10 GHz)) located at an altitude of 22.5 m near Utqiagvik, Alaska (Mahoney et al. 2015). The radar coverage was up to 10 km (Jones et al. 2016; Jones 2013). Bright linear

features show landfast ice and ridges in the radar (Figure 18a) but the radar data do not have any physical units due to the nature of the signal processing by the radar system. The 8-bit pixel values are stretched between 0 and 255. Open water, smooth ice and shadow zones behind large ridges represent low backscatter intensity (Jones et al. 2016).

The interaction of drifting pack ice with landfast ice results in cm-scale ice fracturing or large m-scale deformation in rafting and ridging events. Sea ice drift can be assessed by using SAR backscatter intensity (Griebel and Dierking 2017) through ice drift algorithms (Berg and Eriksson 2013; Demchev et al. 2017; Muckenhuber et al. 2016). An algorithm was built based on SAR backscatter intensity and specific areal matching by phase correlation and feature tracking (Berg and Eriksson 2013). The drift vectors were calculated within a grid spacing of 10 pixels, i.e., 80 m. Figure 18b shows the sea ice drift between 13 and 24 January. Based on the drift field, the convergence zones over the image were derived in the result of coastline compression (Figure 18c). SAR-derived ice drift shows likely areas of ridge formation.

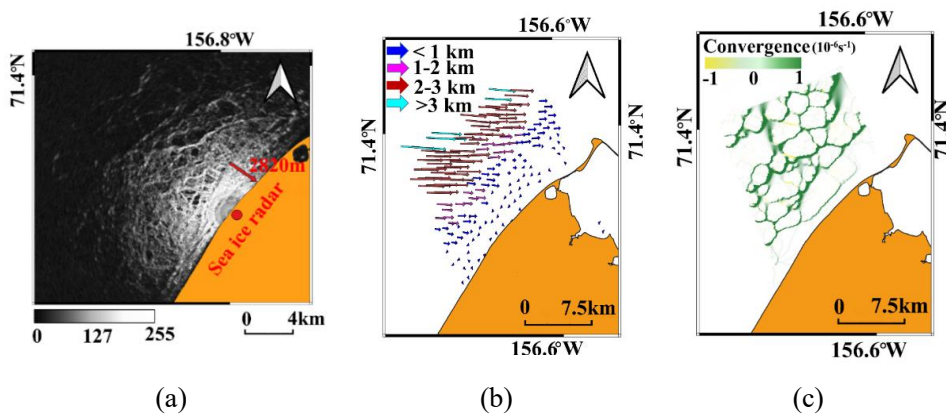


Figure 18. (a) Coastal radar images 13 January 2012, 03:18 UTC. Land is masked out in orange, (b) SAR-derived ice drift vectors (only every 20 vector shown) and (c) convergence during 13-24 January 2012. Land is displayed in orange. Figure adapted from PIIL.

6 Methodology

In this section, methodologies for publications I-IV are summarized and discussed. Section 6.1 presents the InSAR methodological approach to retrieve sea ice displacements. The proposed classifications approach in sea ice classification in both PII and PIV are shown in section 6.2. Section 6.3 present the InSAR methodology approach used in PIII to generate a HDM (Height Difference Map).

6.1 InSAR methodological approach to retrieving sea ice displacements

In PI, the repeat-pass InSAR pair acquired by Sentinel-1 with a small perpendicular baseline was used to generate a displacement map. Processing the SAR data including coherence calculation, and the interferogram production were done using SNAP (Sentinel's Application Platform) software. Based on the area of interest, IW2 sub-swath was selected. While two polarizations (VH and VV) were available, only one VV-pololarization channel was chosen because of its higher coherence magnitude level.

Firstly, two SAR images were co-registered. Then, the orbit correction was applied. The interferogram formation and the coherence estimation were the next steps. Then, the demarcation area between every two bursts were removed by applying TOPSAR deburst. Multi-looking and filtering interferogram phase to to reduce phase noise were the next steps. Phase-filtering was done using a Goldstein phase filter (Goldstein and Werner 1998). There were areas with low coherence measurements, such as water and changed ice surface. Therefore, an area with high coherence was extracted to produce a reliable and high quality unwrapped phase. The phase unwrapping was done using SNAPHU (Statistical-cost Network-flow Algorithm for PHase

Unwrapping). (Veci 2017) Then, the unwrapped phase was converted to a displacement map. The final steps were terrain correction, re-projection and re-sampling to produce a geocoded map. Range doppler terrain correction was done choosing GETASSE30 as DEM, bilinear interpolation as DEM and image resampling method. Then the result was re-projected in WGS 84/ UTM (Universal Transverse Mercator) zone 34 (EPSG: 32604, WGS 84/UTM 34N) with a bilinear resampling method. The last step was resampling done using bilinear interpolation with 20-meter pixel size. The methodology is presented in Figure 19 (User guide Sentinel-1 2021).

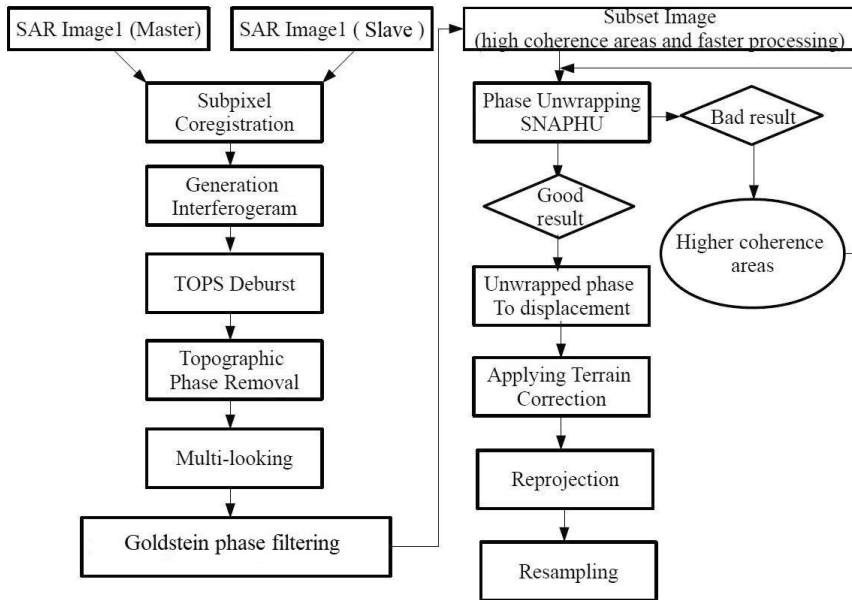


Figure 19. Methodology steps: A schematic block diagram for producing an interferogram and displacement map. Figure adapted from PI.

6.2 Proposed classifications approach in sea ice classification

In PII and PIV, the TanDEM-X image with backscatter intensity, interferometric coherence magnitude, and interferometric phase as classification features were used to do sea ice classification. The image was

orthorectified using ESA SNAP software. The interferometric phase of TanDEM-X had a ramp that initially was not removed from the InSAR-phase feature in PII (affecting the result in this study). It was removed from the phase in the follow-up study in PIV. The phase ramp in the TanDEM-X data could result from possible orbit and atmospheric inaccuracies and it was reported in several studies before (Hanssen 2001; Sadeghi et al. 2014; Solberg et al. 2013, 2015). In PII, PIII and PIV, this effect is most likely due to inaccuracies in the across-track baseline. The phase ramp can deteriorate classification performance and ridge height estimation as shown in PII, PIV and PIII, respectively. The common approach was to remove the phase ramp by averaging all pixels that cover land for each pixel row in the along-track direction. Then, the average was removed for each full row, resulting in a phase image without a ramp and reduced noise. All features were filtered using a (7×7) boxcar filter. The land area was removed by applying land masking. In the last step, linear stretching to the dynamic range $[0;255]$ for any features before doing classification was applied. Single features were backscatter intensity, interferometric coherence magnitude, and interferometric phase. Four combination features were produced from single features by using two or three features in classifiers input. Backscatter intensity & coherence magnitude (the 1st combination), backscatter intensity & InSAR-phase (the 2nd combination), coherence magnitude & InSAR-phase (the 3rd combination), and backscatter intensity & coherence-magnitude & InSAR phase features (the 4th combination) were combination features. The pre-processing steps were the same in PII and PIV but sea ice classes, reference maps, and sampling design were different. The projection was WGS 84/EPSSG:4326 in both publications. (PII and PIV)

In PII, the training plots were selected from the reference map produced by the sea ice expert. The reference map included eight types of sea ice (including

water). Six rectangular plots were selected per each class (three plots for training and three others for validation). RF and ML classification methods were used. In PII, OTB (Orfeo ToolBox) software implementation of RF was used. The number of trees in the forest and the maximum depth of the trees were 100 and 5, respectively. For ML, implementation provided by ESA SNAP was used to perform the supervised ML pixel-based image classification in both publications. In the last step, to filter the classification result, the majority voting in a ball-shaped neighborhood was applied. (PII)

To assure equal representation of classes, a stratified sampling method was used in validation. CM (Confusion matrix) was calculated for all ice classes, and the following accuracy measures including OA, UA (User's Accuracy), PA (Producer's Accuracy) and Kappa coefficient of determination were used (PII):

$$OA = \frac{\text{Number of correct pixels}}{\text{Total number of pixels}}, \quad (20)$$

$$UA = \frac{\text{Number of correctly identified pixels in a map class}}{\text{Number of pixels claimed to be in that map class}}, \quad (21)$$

$$PA = \frac{\text{Number of correctly identified pixels in reference plots of a map class}}{\text{Number of pixels claimed to be in that map class}}, \quad (22)$$

$$\text{Kappa coefficient} = \frac{\text{Observed accuracy} - \text{Chance agreement}}{1 - \text{Chance agreement}}. \quad (23)$$

In PIV, a different sampling design was used. Based on feature properties, a sea ice expert chose 2000 pixels per each class randomly (overall, 14000 pixels for all classes). RF and ML classifiers were applied using SNAP software, and additionally, the SVM classifier was applied using MATLAB. To evaluate the added value of InSAR features (coherence-magnitude and InSAR-phase) compared to backscatter intensity, seven classification experiments have been

performed for each classifier (each feature separately, and their different combinations). After classification, each pixel was assigned to a specific sea ice type or open water. To achieve homogeneous results, a majority voting filter with 5×5 aperture was additionally applied. Classified classes were validated with all classes in the reference map. Normalization to an equal number of samples from each class was performed. Similar to PII, CM was calculated for all ice classes, and OA, UA, PA, and Kappa coefficients were reported. Figure 20 shows the workflow of the proposed algorithm for open water and sea ice type classification in PIV. The workflow in PII was the same as in PIV aside from the phase ramp removal and SVM classification that were added in PIV.

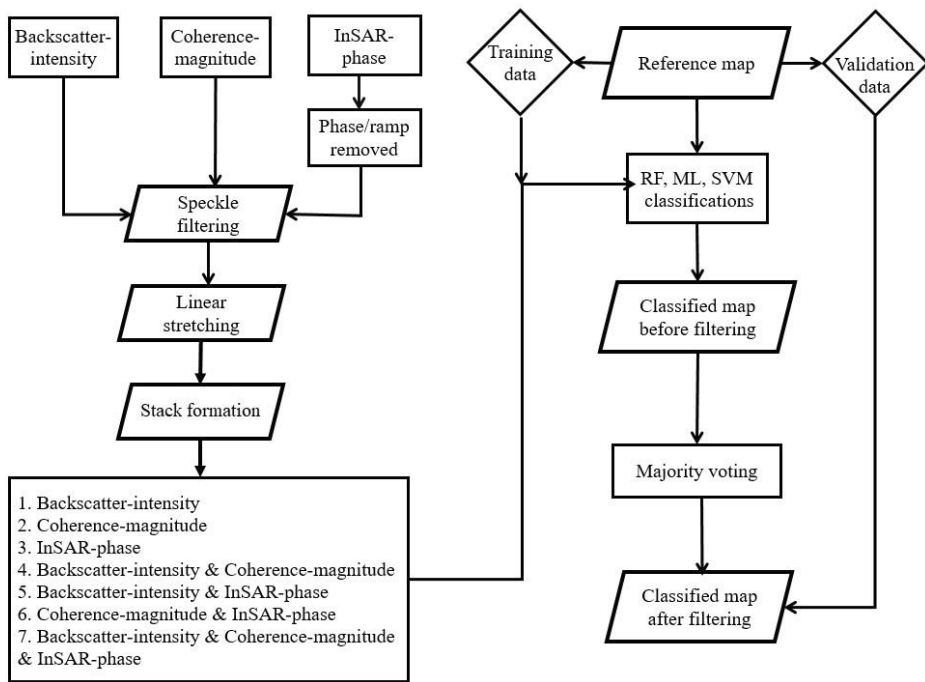


Figure 20. Flowchart of the proposed approach for open water and sea ice-type classification. Figure adapted from PIV.

Further, RF, ML and SVM classification approaches and corresponding classification parameters are briefly explained.

RF classification: RF is a machine learning algorithm that grows multiple decision trees on random subsets of the training data. RF lets any tree vote for the class membership, assigning the respective class according to the majority of the votes (Stumpf and Kerle 2011; Breiman 2001). There are software tools in both SNAP and OTB to perform RF pixel-based image classification. A classifier model is produced by training the RF classifier using various image data feature layers and training data. The training data are represented by polygons with class labels. In the next step, the image classification is performed with corresponding features, with each pixel assigned to a class label (OTB Cook Book 2018). In PII, the following values of RF classifier parameters were set in OTB: the maximum training sample size per class was 1000, and maximum number of trees in the forest was 100. In PIV, SNAP was used to perform RF classification. The overall number of training samples per any class and trees were 2000 and 100, respectively.

ML Classification: The ML classifier is one of the most popular and widely used classification methods (Richards and Jia 2006). The ML estimation determines parameters that best fit a distribution given a set of data. The goal of ML estimation is to estimate the probability distribution which makes the observed data most likely. The SNAP software was used to perform ML pixel-based image classification in both publications. The number of training samples were 1000 and 2000 per each class in PII and PIV respectively.

SVM classification: SVMs are a set of supervised learning methods which are used for classification, regression and outlier detection (Pedregosa et al. 2011). The goal of SVM is to find a hyperplane in a high-dimensional space which delivers optimal separation of the training samples. A kernel and the

kernel parameters control the trade-off between minimizing the training error and the complication of the decision function (Friedrichs and Igel 2005). Solving two-class (binary) classification is easy by using basic SVM. However, multiclass strategy should be used to solve multi-class problems like sea ice classification in PIV. Two of the common methods to enable this adaptation are OVO (One-Vs-One) and OVA (One-Vs-All) (Gidudu et al. 2007; Han et al. 2015). The OVA approach involves the division of a K class dataset into K two-class cases while the OVO approach involves constructing a machine for each pair of classes resulting in $K(K - 1)/2$ machines. The OVO technique was used in PIV (Gidudu et al. 2007). MATLAB was used to train an ECOC (Error-Correcting Output Codes) multiclass model based on SVM binary learners (PIV). Seven sea ice and open water classes were present, thus the OVO model included 21 binary learners. A set of 2000 pixels per each class resulted in overall 14000 pixels used for training the model (PIV). For accuracy assessment of the classification results in PII and PIV, two high-resolution reference maps (Figure 16) were used.

6.3 InSAR methodological approach to generate a Height Difference Map (HDM)

Two single-pass bistatic X-band SAR image pairs (13 and 24 January 2012) were used to evaluate the phase signatures near Utqiagvik, Alaska in PIII. The temporal decorrelation is absent in bistatic mode, so displacement ($\varphi_{displacement}$) and atmospheric phase (φ_{atmos}) were removed automatically from Equation 8. The goal was to generate HDM and involved deriving a DEM for both days using the following processing steps: interferogram formation, multilooking (3×3) to reduce phase noise, flat-earth removal, phase unwrapping using SNAPHU, DEM generation based on the HoA, and filtering (boxcar 5×5) of the elevation maps to improve ridge detection.

DEMs were co-registered before calibrating from relative to absolute heights. This was done based on a known reference point (the Utqiagvik airport). Then the resulting image was projected to UTM zone 4N (WGS 84/UTM zone 4N, EPSG: 32604). A notable elevation gradient or phase ramp in the range direction was visible over DEMs. Next, the difference between the two DEMs was calculated resulting in HDM presented in Figure 21a. A phase ramp generated from TanDEM-X data was assumed due to possible inaccuracies in the across-track baseline over Figure 21a which was removed and the result was filtered by 3×3 boxcar filter. The final output was an HDM without a noticeable height ramp and reduced noise (Figure 21b). The HDM spatial resolution was 7 meters. (PIII)

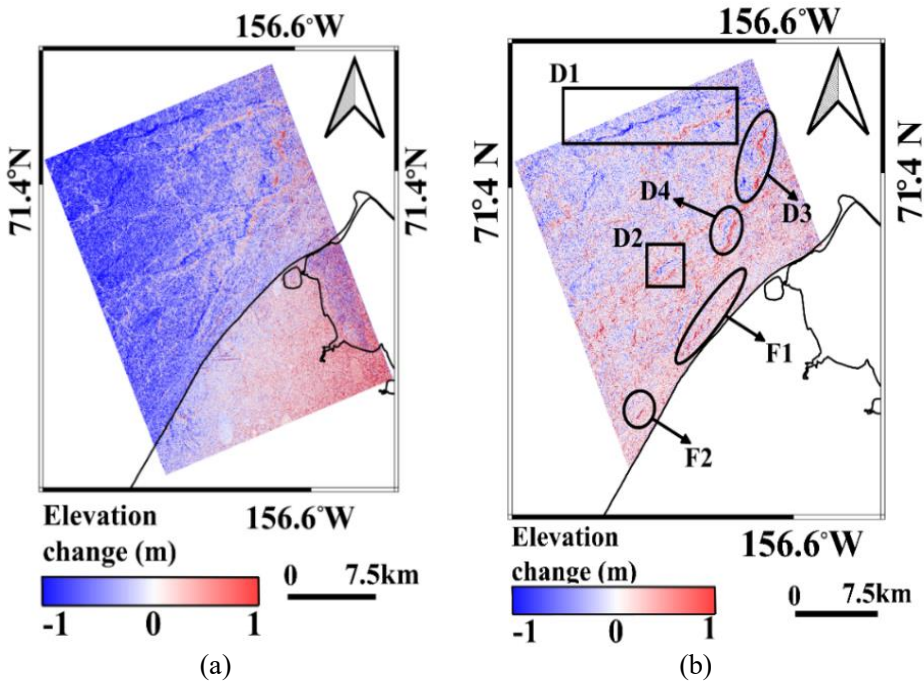


Figure 21. HDM before (a) and after (b) removing the ramp in elevation change. Locations of ridge displacements are marked D1–4 and formation F1–2 in (b). The coastline is outlined in black and was used to mask out land and the ice in Elson Lagoon (b). Figures adapted from PIII.

For validation, coastal radar data, backscatter intensity and SAR based sea ice drift data were used as explained in detail in section 5.2.

7 Results and discussion

In this section, the most important findings from Publications I-IV are summarized and discussed. Section 7.1 presents the results from PI, where sea ice displacement was in the order of 40 cm in the study area and displacements factors were evaluated. Section 7.2 and 7.3 present results from PII and PIV respectively and discuss the relative performance of different SAR features and their combinations over various sea ice types in different classifiers in both publications. Ridge displacement and formation estimation over landfast ice near Utqiagvik Alaska (PIII) are presented and discussed in section 7.4.

7.1 Displacement analysis over Baltic landfast ice

The coherence (Figure 22a), interferogram (Figure 22b) and displacement maps (Figure 23) are products of methodology flowchart (Figure 19). The fringes in the interferogram were converted to displacements in the LOS in Figure 23. One fringe corresponds to an approximately 27.5 mm displacement in LOS. The resulting displacements were from -10 cm to 30 cm over landfast ice. The negative sign indicates that the ice has moved away from the satellite by either sinking or moving to the west, and positive indicates movement towards the satellite by either lifting up or moving to the east. (PIII)

The southern part of the polygon was moving away, and the northern part was getting closer to the satellite. These movements created a converging zone between the southern and northern parts and the projected strain was approximately 40 cm across a 20 km distance (Figure 23).

The movements are due to horizontal or vertical changes, or a combination of both. As a descending pair was used, it is not possible to separate the horizontal and vertical changes. One reason for a vertical displacement could be sea level tilt. Absolute sea level elevation could not affect interferogram fringes because the landfast ice is afloat, but sea level tilting might affect fringes according to $\Delta R = \varphi/2k$, where φ is the interferometric phase, and $k = \frac{2\pi}{\lambda}$ is the wave number, which was equal to 114.20 m^{-1} (PI).

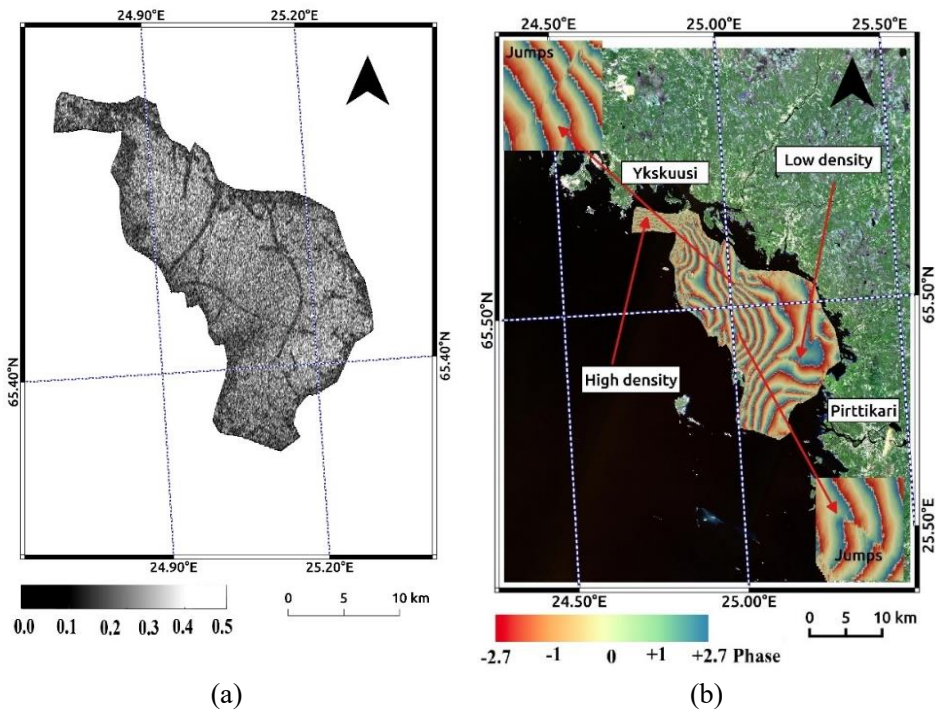


Figure 22. (a) The extracted polygon with high coherence (0.2-0.46) for the image pair of 6 and 18 February 2015 over the Baltic Sea. (b) The interferometric phase. The Sentinel-2 image was used as background. Water and land are shown in black and green respectively. Figures adapted from PI.

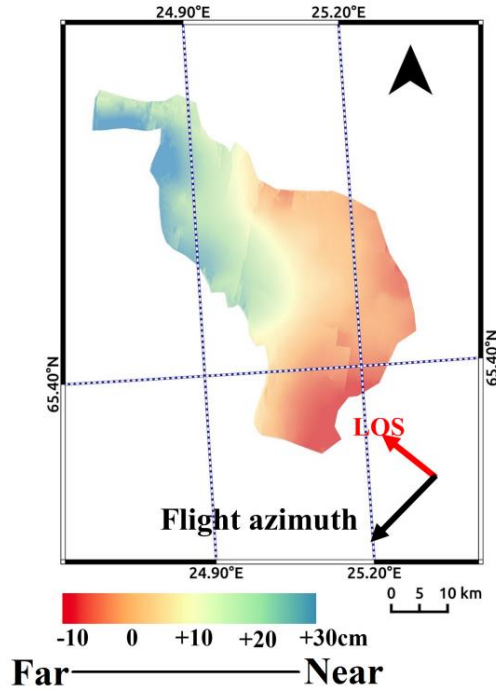


Figure 23. Displacement map from the unwrapped 6-18 interferogram. ‘Near’ and ‘Far’ means close to the satellite and far away from the satellite respectively. Figure adapted from PI.

The sea level data showed that in this case, sea level could make only small relative vertical displacements. In the period of study, from 6 to 18 February, the sea level decreased from 41.4 to 36.0 cm in Oulu and from 39.7 to 36.5 cm in Kemi. Thus, the maximum relative change in sea level was 2.2 cm and the distance between the sea level stations was 82 km (PI). The absolute sea level ranged within ± 50 cm in the period of study, but the whole water body moved up and down almost coherently leaving tilts across the basin below 5 cm over a 100-km distance. The sea level information was presented in Figure 13. Another possible reason is ice growth but here changes of freeboard could make vertical displacements only less than one centimeter. Regarding the lateral displacement, that may happen due to thermal expansion. However, one

would not expect to see simultaneous thermal expansion and contraction here, as Figure 23 would suggest. (PI)

The only possible reason to have the observed lateral displacements is mechanical forcing by winds or water currents. Water currents were not measured but they tended to be small below the landfast ice. The location of the study area (Figure 23) was within the landfast ice regime during the period. The landfast ice thicknesses at that time were around 30-50 cm, and in that sheltered part of the archipelago, landfast ice of that thickness remains quite firmly in place (Leppäranta 2013). Outside the landfast ice regime and the study area, there was thin level ice and close ice, based on the operational ice charts (Figure 10b). By overlaying both backscatter intensity images on 6 and 18 February (Figure 11), it was shown that on 6 February, the offshore area in the west of the study area was covered with mainly thin level ice. As could be expected from wind records on 10, 16 and 17 February (Figure 12), with predominantly strong south-westerly winds with high speed, on the order of 15 m/s, the drift ice was compressed towards the landfast ice edge and deformed to ridges and rafted ice. This deformation can be seen as features with bright backscatter intensity on 18 February 2015 (Figure 11b) and as very close or consolidated drift ice with ridge symbols in the operational ice charts. The southwest wind had a minor influence on the inner part of the landfast ice zone where the fringes were shown. There was a simultaneous dilatation along the boundary, as typically takes place in such forcing conditions (Goldstein et al. 2009).

Landfast ice had heavier deformation with ridging further out near the landfast ice boundary. This area was away from the landfast ice boundary suggesting that the main load of the southwest storm did not reach the study area.

There were some small phase jumps in the fringe pattern showing shearing and cracking (Figure 22b). However, these phase jumps were not strong enough to make changes in the fringe pattern. There were also black lines in Figure 22a with low coherence, even 600 meters long. Some of them match the phase jumps in Figure 22b. There are two possibilities to have these phase jumps over the area of study: a) Fractures due to landfast ice displacement, and b) Ice roads. The latter option was evaluated by overlaying one of the SAR backscatter intensity scenes on Google Earth, and it was seen that the lines could be routes between islands used by people for fishing. By looking at Krassinletto island, it was clear that most of the black lines finished there. There were some tracks that did not seem to reach an island, but they could represent fishing camps on the ice. (PI)

7.2 Relative performance of different SAR features and their combinations over sea ice in RF and ML classifiers

PII was the first effort to evaluate the possibility to use the InSAR technique in sea ice classification. This work was later expanded in PIV with additional classification approaches and with different sea ice types. Fourteen classification experiments were calculated for seven types of single and combinations of features by using RF and ML classifiers. The best OAs achieved by combining backscatter intensity & InSAR-phase and backscatter intensity & coherence-magnitude were 76.9% and 75.8% with RF and ML classifiers, respectively. The best classification result with the largest OA is shown in Figure 24.

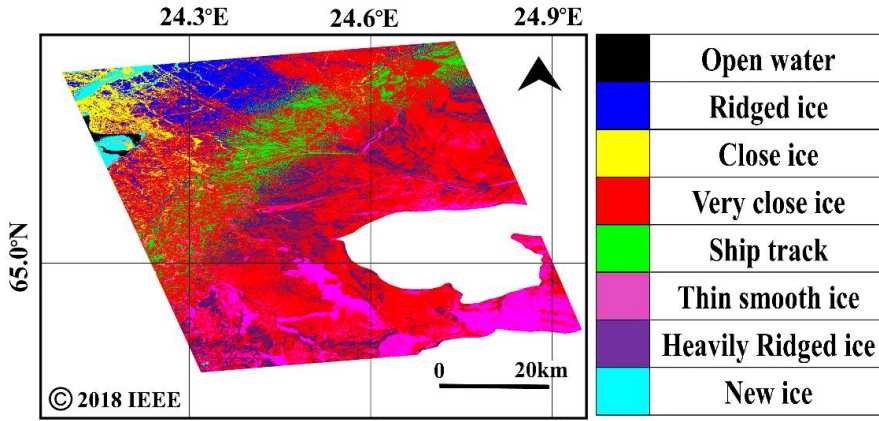


Figure 24. RF classification map (backscatter intensity & InSAR-phase combination). Figure adapted from PII.

Accuracy assessment was performed for the different combinations of features (Table 9). OAs for produced maps in RF experiments indicated that the combined backscatter intensity & InSAR phase had the largest OA of 76.9%, while the backscatter intensity & coherence-magnitude and coherence-magnitude & InSAR phase were the second and third with 70.1% and 67.5%. The computation time for RF classification was almost two minutes for each single feature and somewhat increased for combinations of two and three features. OAs in ML experiments indicated that backscatter intensity & coherence-magnitude and backscatter intensity & InSAR phase had the largest OAs of 75.8% and 75.6%. The coherence magnitude had the third largest OA of 73.5% in ML experiments. The computation time for ML classification was more than three minutes for each feature and increased a bit when two or three features were used. (PII)

Table 9. OAs of RF and ML in PII (classification features: B = Backscatter intensity, C = Coherence-magnitude, I = InSAR-phase).

| Single/combinations features | OA_{RF}(%) | OA_{ML}(%) |
|-------------------------------------|---------------------------|---------------------------|
| B | 61.7 | 63.5 |
| C | 63.7 | 73.5 |
| I | 53.3 | 58.2 |
| B-C | 70.1 | 75.8 |
| B-I | 76.9 | 75.6 |
| C-I | 67.5 | 65.9 |
| B-C-I | 66.8 | 67.0 |

Based on UAs in ML and RF classifiers for each water and sea ice classes (Tables 1, 2 in PII), open water and new ice were classified with 100% UA in both classifiers. Ridged ice was not classified by using the InSAR-phase feature and combination of InSAR phase with other features (almost 0%). Close ice had better UA when features were combined. Heavily ridged ice was very well classified when features were combined. Thin smooth ice was extremely well classified using coherence magnitude & InSAR phase. As ship track had the lowest UA accuracies, the suggestion was to use other methods such as segmentation and shape feature detection (Berthod et al. 1996).

Overall, backscatter intensity & InSAR phase and backscatter intensity & coherence magnitude in the RF and ML classification experiments gave the largest accuracies. However, in the end, the backscatter intensity & InSAR-phase combination was suggested because of 1) the largest OA among all RF and ML experiments and 2) shorter processing and run time in comparison with ML experiments. The results showed advantage of InSAR features in combination with backscatter intensity in sea ice classification (PII). Although the expectation was to achieve the largest OA with a combination of three features in PII that was not possible likely due to a ramp over the InSAR phase. This limitation was removed in PIV. Discrimination of open water from new

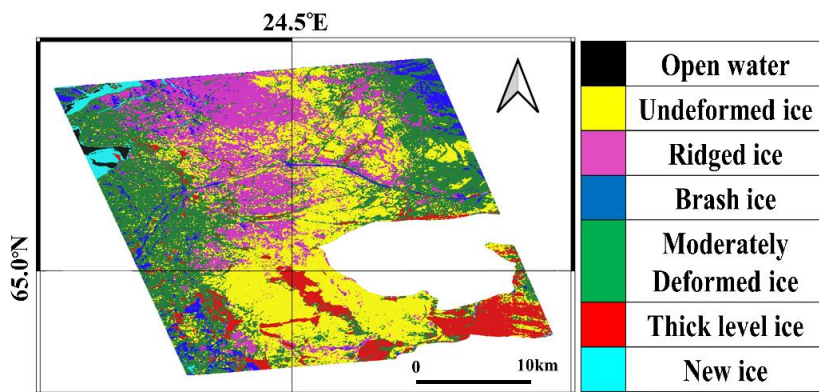
ice was done in PII and it was examined in more detail in PIV (more details in section 7.3.3).

7.3 Analyses and discussion of sea ice classification using InSAR features in RF, ML and SVM classifiers

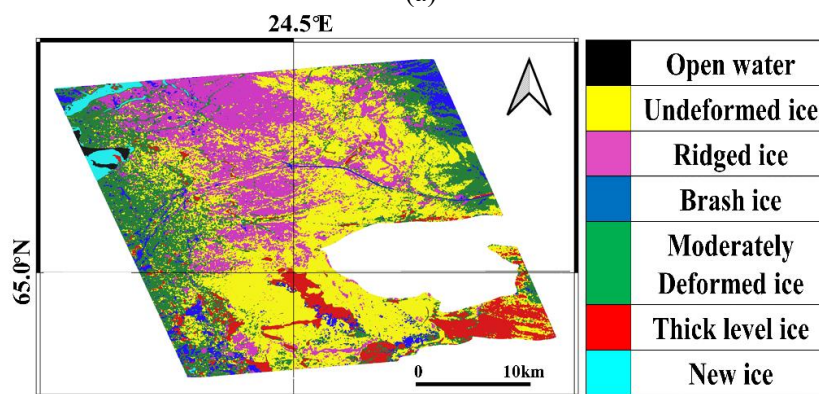
In PIV, twenty-one CMs were calculated for seven types of single and combinations of features in several classification experiments. Values of OA, Kappa (Table 10), UA and PA assessments (shown in Figure 7, 8, 9 in PIV) for all experiments were shown alongside CMs. The largest OA in RF and SVM experiments were 72.9% and in ML was 71.6% (all three features combined). The best classification maps by any classifiers are shown in Figure 25. These results confidently suggested that a combination of features are strongly better than single features for sea ice classification. The computation time for ML, RF and SVM classifications were 12 to 15 seconds, 5 minutes and 30 seconds per any image feature respectively, and it slightly increased when using a combination of two or three features.

Table 10. OAs of RF, ML and SVM and Kappa coefficients (classification features: B = Backscatter intensity, C = Coherence-magnitude, I = InSAR-phase) in PIV.

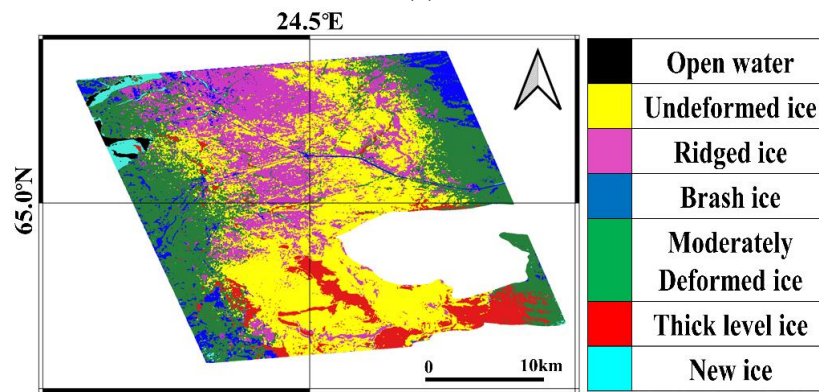
| Classification features | OA _{RF} (%) | Kappa (RF) (%) | OA _{ML} (%) | Kappa (ML) (%) | OA _{SVM} (%) | Kappa (SVM) (%) |
|-------------------------|----------------------|----------------|----------------------|----------------|-----------------------|-----------------|
| B | 66.5 | 60.9 | 62.3 | 56.0 | 63.1 | 56.9 |
| C | 61.6 | 55.2 | 59.7 | 52.9 | 61.9 | 55.5 |
| I | 43.0 | 35.0 | 50.9 | 42.7 | 52.6 | 46.2 |
| B-C | 72.4 | 68.7 | 70.0 | 65.0 | 72.2 | 68.4 |
| B-I | 71.8 | 67.1 | 70.3 | 65.3 | 72.8 | 68.2 |
| C-I | 64.1 | 58.1 | 62.0 | 55.6 | 61.9 | 55.5 |
| B-C-I | 72.9 | 68.4 | 71.6 | 66.8 | 72.9 | 68.4 |



(a)



(b)



(c)

Figure 25. Final classification map using combined backscatter intensity & coherence magnitude & InSAR phase with (a) RF; (b) ML; (c) SVM classifications. Figures adapted from PIV.

7.3.1 OAs, UAs and PAs comparisons and class-wise performance for all classifiers (RF, ML, SVM)

RF had higher OAs than ML in all single and combination features except the InSAR phase. RF was better than ML in all cases including backscatter intensity (4.2%), coherence-magnitude (2.0%), backscatter intensity & coherence-magnitude (2.5%), backscatter intensity & InSAR-phase (1.6%), coherence-magnitude & InSAR-phase (2.1%) and backscatter intensity & coherence-magnitude & InSAR-phase (1.4%) combinations. (PIV)

OAs were almost the same in RF and SVM classifiers and differences in coherence magnitude, backscatter intensity & coherence magnitude, backscatter intensity & InSAR phase and backscatter intensity & coherence magnitude & InSAR phase were close to zero. RF acted better than SVM for experiments with backscatter intensity (3.5%) and coherence magnitude & InSAR phase (2.2%) except in the InSAR-phase feature where it was 9.7% units less than SVM classification. (PIV)

UA and PA calculations showed a strong difference between all classifiers (RF, ML, SVM) for sea ice classes including undeformed ice, ridged ice, moderately deformed ice and brash ice, whereas no significant differences were found between RF-ML and RF-SVM classifiers for sea ice classes including new ice, thick level ice and open water (PIV).

Table 11 shows the highest and lowest UAs and PAs for input data in RF, ML and SVM. The best detected class was open water with UA 97.7% by using combination features backscatter intensity & coherence magnitude (SVM classifier) whereas brash ice was the hardest class to discriminate with UA zero by using only the InSAR phase (ML and SVM classifiers).

Regarding PA, the best detected class was open water with PA 97.1% using combination features backscatter intensity & coherence magnitude (ML classifier) whereas brash ice was the hardest class to discriminate with zero by using only InSAR phase (ML and SVM classifiers) such as UA part. (PIV)

Table 11. The highest and lowest UAs and PAs for input data in RF, ML and SVM classifiers. Classification features: B = Backscatter intensity, C = Coherence-magnitude, I = InSAR-phase. Water and sea ice classes (U = Undeformed ice, R = Ridged ice, M = Moderately deformed ice, B = Brash ice, T = Thick level ice, N = New ice, O = Open water.

| Classification features | Classes with highest/lowest UA in RF (%) | Classes with highest/lowest PA in RF (%) | Classes with highest/lowest UA in ML (%) | Classes with highest/lowest PA in ML (%) | Classes with highest/lowest UA in SVM (%) | Classes with highest/lowest PA in SVM (%) |
|-------------------------|--|--|--|--|---|---|
| B | O (95.5)/ M(35.1) | N (96.1) / U (37.4) | O (94.6) / M (11.5) | O (93.1) / M (20.4) | O (94.9) / M (19.8) | N(96.0)/ M (27.6) |
| C | O (95.6)/ U (29.9) | N (92.3) / U (37.3) | N (93.9) / U (2.6) | O (96.0) / R (36.9) | O (95.9) / R (37.4) | N (92.8) / U (39.2) |
| I | O (84.2)/ U (2.9) | O (82.5) / U (10.4) | O (88.7) / B (0) | N (83.1) / B (0) | O (87.8) / B (0) | N (82.7) / B (0) |
| B - C | O (96.4)/ U (51.3) | N (94.7) / M (50.9) | O (94.6) / M (48.8) | O(97.1)/ U (48.6) | O (97.7) / R (55.6) | N(96.2)/ R (52.7) |
| B - I | O (94.1)/ U (50.9) | N (95.4) / M (48.6) | O (92.6) / B (49.5) | N (94.9) / U (49.4) | O (92.9) / R (56.9) | N (95.2) / R (52.3) |
| C - I | O (94.7)/ U (42.9) | N (92.3) / M (40.5) | N (94) / B (15.8) | O (95.8) / R (38.4) | O (94.5) / B (22.4) | N (91.8) / R (42.9) |
| B - C - I | O (93.9)/ U (51.2) | N (92.8) / M (50.8) | O (94.6) / B (51.0) | O (96.7) / R (49.9) | O (96.9) / R (55.6) | N (95.4) / R (52.8) |

7.3.2 Role of SAR interferometry in classification performance

Using three features did not help to better classify brash ice, thus, using other methods for discriminating brash ice from the rest of the ice is strongly suggested (Berthod et al. 1996). However, adding InSAR features helped to discriminate most sea ice classes better compared to using backscatter intensity alone. For example, using InSAR features with backscatter intensity

increased classification accuracy for moderately deformed ice (UA: 43.2%, PA: 13.3%) in RF, (UA: 51.2%, PA: 32.7%) in ML and (UA: 58.5%, PA: 27.0%) in SVM classifiers. Increased PA accuracies are visible in undeformed ice (PA_{RF} : 26.9%, PA_{ML} : 19.6%, PA_{SVM} : 32.4%), ridged ice (PA_{RF} : 6.6%, PA_{ML} : 5.2%, PA_{SVM} : 7.1%) and thick level ice (PA_{RF} : 3.8%, PA_{ML} : 3.5%, PA_{SVM} : 3.7%).

Backscatter intensity classification results (OAs of RF, ML and SVM) were on the order of 66.5%, 62.3% and 63.1% respectively. By adding coherence-magnitude and InSAR-phase features to the backscatter intensity feature, OA improvements have been detectable in all results by 6.4% in RF, 9.3% in ML and 9.9% in SVM. Based on these results, overall, InSAR features show that they are valuable in sea ice classification and can be used as an option in future in sea ice operational mapping services. (PIV)

7.3.3 Open water and sea ice discrimination

Before further discussion about open water and sea ice discrimination, it is worth mentioning that the terms of thin smooth ice and thin ice in previous studies (Laanemäe et al. 2016; Geldsetzer and Yackel 2009) and new ice in PII and PIV essentially mean the same thing. Open water and new ice (thin smooth ice in Laanemäe et al (2016) and thin sea ice in Geldsetzer and Yackel (2009)) are common surface types in previous studies and ours.

Reliable discrimination of open water and new ice is one of the key questions in sea ice remote sensing that is difficult due to the similarity of backscatter intensities for those classes (Geldsetzer and Yackel 2009). The only study with a combination of intensity and coherence of TanDEM-X over the Baltic Sea has been reported by Laanemäe et al. (2016). Landfast ice, pancake ice, open water, and new ice were sea ice classes presented in Laanemäe et al. (2016). Several incidence angles have been examined although separation between

different ice types was not possible with low incidence angles (Laanemäe et al. 2016). The best result was achieved by using a high incidence angle (44.9°). Open water had low coherence (approximately 0.3 to 0.4) but the coherence of landfast ice was much higher, around 0.6 to 0.7. Therefore, the open water/ice classification is accurate in high incidence angles, although separation between new ice and open water was not achieved in this study.

In PII and PIV, a similar and high incidence angle (43.41°) image was used to discriminate between sea ice types and open water. Open water and new ice were common sea ice types in Laanemäe et al. (2016), PII and PIV.

The wind speed in three studies, ((Laanemäe et al. 2016), PII and PIV), did not exceed 7 m/s. The coherence magnitude for open water was the same and on the order of 0.2 in three studies whereas the new ice coherence value in Laanemäe et al. (2016) was almost 0.2 but it increased a lot in PII and PIV (around 0.6). Discrimination between open water and new ice with backscatter intensity and coherence-magnitude features was done in PII and PIV. This discrimination was also visible in other sea ice types. Although backscatter intensity values were near each other for new ice and open water, a significant difference is visible in the coherence features in Figure 26.

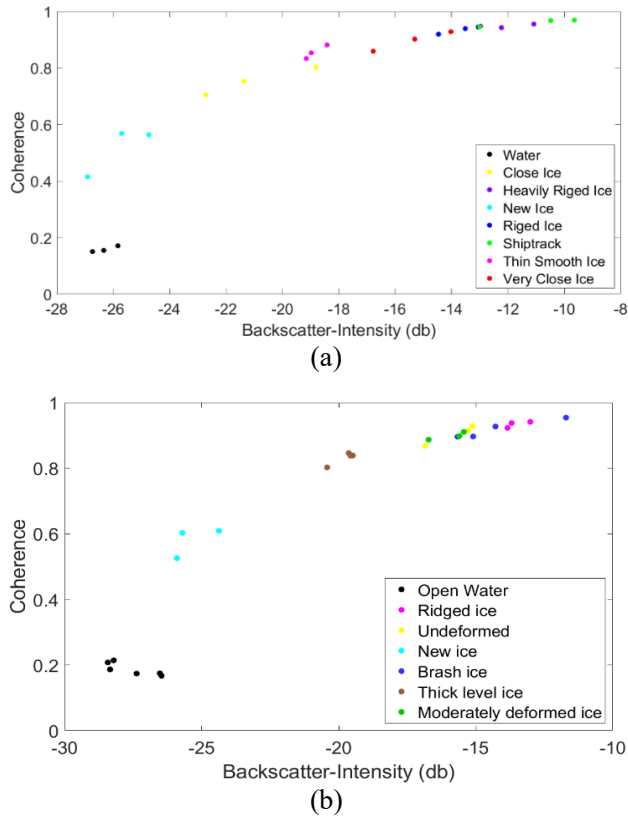


Figure 26. Coherence-magnitude and backscatter intensity values of water and sea ice types for plots using pair HH-bistatic data for coherence-magnitude calculation and HH-bistatic data for backscatter intensity calculations in (a) PII and (b) PIV. Figure b adapted from PIV.

The reason for this success compared to Laanemäe et al. (2016) was in monostatic mode in Laanemäe et al. (2016), new ice can move due to few seconds temporal changes which can decrease coherence magnitude but in bistatic mode in PII and PIV due to very small temporal changes then new ice is not moving or drifting so, we have higher coherence. So, in overall, in bistatic acquisition, wind speed does not cause temporal decorrelation of interferometric coherence in comparison with the monostatic mode. Figure 26a, b shows discrimination results in both PII and PIV, respectively. There are some prior studies (Leppäranta et al. 1992; Hyypä and Hallikainen 1992;

Mäkynen and Hallikainen 2004; Eriksson et al. 2010), where they also used only the backscatter intensity without coherence magnitude in X-band for sea ice classification. The BEPERS (Bothnian Experiment in Preparation for ERS-1) pilot study was carried out in 1987 using the French VARAN-S X-band SAR to learn about using ERS-1 data (Leppäranta et al. 1992). X-band frequency with 9.375 GHz with horizontal polarization, flight altitude about 6000 m, incidence angle from 11 to 67 (right-look direction), spatial resolution in single look $3 \text{ m} \times 3 \text{ m}$, nine looks $9 \text{ m} \times 9 \text{ m}$, and quick look 70 mm black-and-white film was used during the research. Eight ice types were defined: (1) lead (open water), (2) bare smooth ice, (3) patchy (ice-snow) level ice, (4) snow covered ice, (5) frozen uneven ice, (6) old ridges, (7) young ridges, and (8) brash ice. The first four sea ice types represent water or undeformed ice surfaces and the other four are deformed ice surfaces with broken ice pieces. Only discrimination between open water/undeformed ice and deformed ice was possible but a finer classification was difficult. (Leppäranta et al. 1992). In a study by Hyypä and Hallikainen (1992), helicopter-borne scatterometer measurements HUTSCAT (Helsinki University of Technology Scatterometer) were used at 5.4 GHz and 9.8 GHz (C- and X- band) with an incidence angle of 23° off nadir to investigate the backscattering behavior of the Baltic Sea ice. Based on the results, C-band was a bit better than X-band in sea ice mapping (Hyypä and Hallikainen 1992). Ice ridges were the only sea ice type that could be clearly recognized in co-polarization data (HH, VV) but thick level ice, hummocked ice, new ice, and open water had overlapped with each other. The discrimination between three sea ice groups including new ice – open water, thick level ice, and hummocks – ice ridges was possible using cross-polarization (HV, VH). Based on this study, improving sea ice discrimination is possible efficiently by the parallel use of co- and cross-polarized channels, although the dataset used in Hyypä and Hallikainen

(1992) was almost limited. In a more comprehensive study by Mäkynen and Hallikainen (2004), the HUTSCAT scatterometer was used again with C- and X-band (5.4 and 9.8 GHz) data during six ice research campaigns in 1992–1997. HUTSCAT measurements were applied over test locations including different sea ice types with incidence angles of 23° and 45°. Most of the data was captured when the snow was moist or wet. Eight sea ice classes were investigated including (OW (Open Water leads), nilas, SLI (Smooth Level Ice), RLI (Rough Level Ice), SDI (Slightly Deformed Ice), HDI (Highly Deformed Ice), LBI (Loose Brash Ice) and FBI (Frozen Brash Ice)). It is good to mention that SLI and RLI are in a main group titled ‘level ice’, SDI and HDI are in the ‘deformed ice’ and LBI and FBI are in the ‘brash ice’ groups. Sea ice discrimination was not successful reliably by using an automated procedure using only the radar intensity as a criterion. The best results for discrimination of deformed ice, level ice (including slightly deformed ice), and nilas were achieved at C-band with an incidence angle of 45°. The standard deviation of intensity values for different sea ice classes were included. However, the classification performance of X-band was almost similar to C-band (Mäkynen and Hallikainen 2004). Mäkynen and Hallikainen (2004) had a 45° incidence angle in their scatterometer study, about the same as in PII and PIV, and also, there is overlap between the sea ice types in three studies. This could be a good case for comparison, however, the data about the liquid water content snow is limited in PII and PIV. According to weather data from the stations in Hailuoto and Kemi Ajos, the snow surface was frozen but a knowledge about deeper snow is necessary to know about snow wetness or dryness. Based on reports from the Hailuoto and Kemi Ajos stations, Ajos data indicates that in mid-March there was max 25-30 cm of snow on ice and thereafter the snow thickness decreased and snow-ice increased. The data suggest that on 26 March–2 April, flooding occurred for the slush and

consequent snow-ice production. In Hailuoto station, there was no snow-ice formation but snow was deep enough for a possibility of slush formation. Thus, from these data we cannot say whether the snow was dry or wet but both options are possible (FIS 2012). Eriksson et al. (2010) presented a study by using satellites in L, C and X bands to evaluate their usefulness for sea-ice monitoring in the Baltic Sea. SAR data was captured by the ALOS and the ENVISAT, RADARSAT-2, and TerraSAR-X satellites. Radar signature characteristics with different frequencies, polarizations, and spatial resolutions are available for three dates in 2009 (19-20 February, 21-22 March and 23-24 April). Pros and cons of the different SAR systems and imaging modes were identified. One of the results was that discrimination between sea ice and open water improved when using cross-polarized SAR data compared to co-polarized data. Algorithms for SIC retrieval improved by using a combination of co-polarized and cross-polarized SAR data. Sea ice ridges are better identified in cross-polarization although it should be taken into account that the SNR ratio is rather low, in particular for new ice. Sea ice ridges are also easier to distinguish in L-band in comparison with C- and X-bands. While retrieved information from X- and C-band images is mostly equivalent, the L-band data present complementary information. In addition, L-band SAR is less sensitive to wet snow cover on the ice compared to C- and X-bands. Incidence angles for TerraSAR-X band was on an order of 20° to 21.8° , 21° to 22° , 26.4° to 30.1° for three examples from 2009 including Feb (19-20), Mar (21-22) and Apr (23-24) respectively which are not comparable with our studies within the incidence angle on an order of 43° (Eriksson et al. 2010).

7.4 Ridge displacement and formation estimations over landfast ice near Utqiagvik Alaska

Locations of ridge displacement or formation events that took place between 13 and 24 January 2012 are shown as D1-4 (ridge displacement) and F1-2

(ridge formation) over HDM (Figure 21b). Ridge displacement was detected via a positive elevation change (red) near a similar pattern of negative elevation change (blue) where the displaced ridge was previously located. Blue and red features on HDM present locations of ridges on 13 and 24 January, respectively. Drift vectors of the used ice drift algorithm (green arrow in Figure 27e) were chosen from the starting point of the blue-colored area. Further on, their average was calculated, shown using yellow arrows. Five control points were chosen on each ridge to explain ridge displacements shown in different figures. The 'a' and 'b' labels of control points denote prior and posterior location of ridges respectively (Figures 27). Distances between 'a' and 'b' were measured and then, for each displacement, averages were calculated (not shown in figures). Next, averaged control points were compared with the drift vector averages (yellow arrows). To identify ridge formation, a positive elevation change without a similar nearby negative response was detectable on HDM. (PIII)

7.4.1 Detection of ridge displacement

D2 is one of the ridge displacements in this study that was checked using three cross-validation tools (backscatter intensity, coastal radar, and the drift algorithm). Five control points (Figure 27a and b in backscatter intensity images and Figure 27c and d in coastal radar images) with a displacement average of 1.0 km was identified. Thirteen vectors were identified with the drift algorithm indicating an average displacement of 1.0 km (yellow vector in Figure 27e), nearly identical to what was derived based on the backscatter intensity data and coastal radar control points (control point averages were also near 1 km). (PIII)

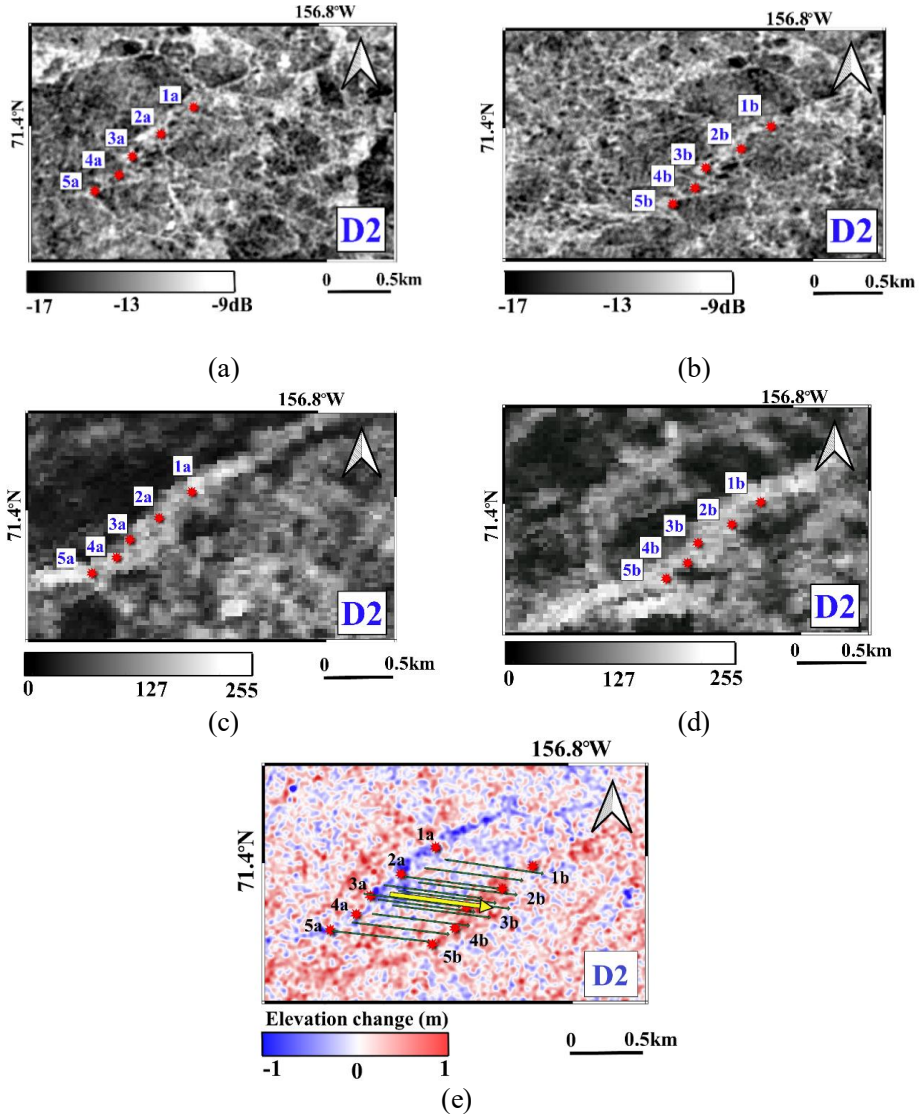


Figure 27. D2: SAR backscatter intensity on 13 January (a) and 24 January 2012 (b). Coastal radar images on 13 January (c) and 24 January 2012 (d). HDM is displayed in (e) with individual displacement vectors in green and average displacement vector in yellow. Control points 1a-5a and 1b-5b represent ridge features that can be recognized before and after the displacement. Figures adapted from PIII.

D1 was another displacement case that was only checked by backscatter intensity and the drift algorithm because ridges were not well detectable in coastal radar. Five control points represented ridge features on both backscattering images and also HDM. The averaged displacement between control points over the SAR backscatter intensity images and the HDM was 3.7 km. We also tried to compare displacement between control points with vectors of the drift algorithm for the whole D1 displacement, but due to limited performance of the ice drift algorithm in the image border, only 7 vectors were detectable with an average of 3.4 km, which is the same as the displacement measured based on two control points over HDM, i.e. 3.4 km. (PIII)

D3 and D4 were located along the same ridge and the same as D1, they were checked with backscatter intensity and the drift algorithm. In both cases, five control points were identified over their backscatter intensities and the HDM. In D3, the averaged displacement between control points over the SAR backscatter intensity images and the HDM was 0.9 km. The drift algorithm also presented same amount of displacement, 0.9 km, by a total of 41 vectors. In D4, a displacement corresponding to the shift indicated by the control points at 0.7 km was indicated by the HDM. The drift algorithm identified a total of 46 vectors along the ridge with a resulting mean displacement of 0.6 km for similar to what is indicated in the control points and HDM. (PIII)

7.4.2 Detection of ridge formation

Two ridge formations (F1 and F2) were analyzed in PIII. One of them (F1) is presented in this dissertation. F2 was studied in detail in PIII. Cross-validation of HDM was done using backscatter intensity and coastal radar data. Convergence/divergence zones identified by the drift algorithm (Figure 18c) were included into the cross-validation dataset. F1 was the result of a combination of several ridges forming near to the coast, which were already there. This made it difficult to detect any ridge development in this area. Backscatter intensity somewhat increased on 24 January (shown as a red outline in Figure 28b) compared to 13 January (red outline in Figure 28a) from -12.4 to -12.2 dB.

However, the elevation change presented in Figure 28e (black outline) showed that the ridge has increased up to one meter during the study period. In addition, evaluation of the convergence results from the drift algorithm (Figure 28f) showed substantial convergence of roughly 10^{-6} s^{-1} within ~ 200 m of the location of the stark elevation changes (black outline in Figure 28e). This corresponded to a convergence rate of ~ 1 during the 11-day timespan indicating that for every meter of ice, it was compressed by roughly one meter. Ice thickness was almost one meter (described in section 5.2). Based on this discussion, it is possible to increase the ridge height up to one meter by assuming the resulting rubble/small ridge ends up resting on surrounding ice leading to minimal draft. As is clear in Figure 28f, the convergence area is not well overlapped with ridge formation due to a combination of ridge buildup and displacement in one event. (PIII).

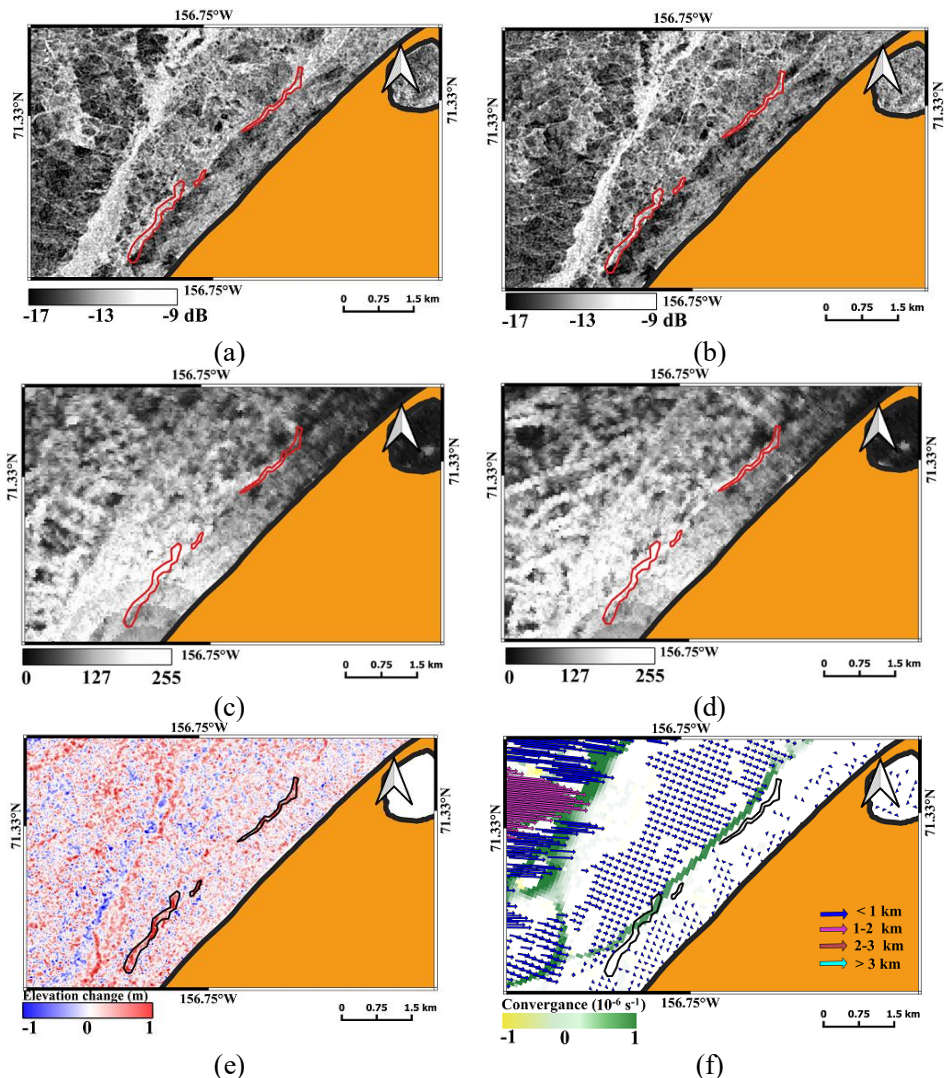


Figure 28. SAR backscatter intensity on 13 January (a) and 24 January 2012 (b). Coastal radar images on 13 January (c) and 24 January 2012 (d). HDM is displayed in (e). Results from the drift algorithm are displayed as motion vectors and convergence zones (f). Red and black outlines in panel a-f signify the area of ridge development. Land is masked out in orange. Figure adapted from PIII.

7.4.3 Ridge formation and displacement discussions

Ample studies evaluated landfast ice deformations by using repeat-pass InSAR (Dammert et al. 1998; Berg et al. 2015). In PIII, the focus was over

landfast ice but this time, single pass TanDEM-X data were used with no limitations such as temporal and atmospheric decorrelations.

The technique used is feasible for landfast ice studies. It is also suitable for drifting ice with a few limitations, such as:

- 1) Avoiding coherence loss by using only the SAR acquisitions with short enough temporal baseline (single-pass InSAR for generation of the height maps).
- 2) Co-registration of individual ridges as they are likely to shift between acquisitions.
- 3) Removing the impacts of motion of drift ice on the interferometric phase from the analysis to avoid significant reductions in accuracy.

Using this method over non-stationary ice can be suitable in locations where sea ice motion is limited, such as fjords or bays. Particularly, it was possible to identify ridges in two consecutive TanDEM-X acquisitions spanning an 11-day time period. However, the method still needs image geometries with higher spatial baseline on the order of several hundred meters such as the Science Phase mode to decreasing HoA, which further limits data availability. The use of this technique for non-restricted free-drifting ice is challenging at present, but theoretically possible for ice floes that can be identified in two different TanDEM-X acquisitions and co-registered to enable ridge formation analysis. If more single-pass InSAR systems appear in future, evaluation of the difference between height maps from different satellite systems might be possible. This can enable time intervals shorter than 11 days that are dictated by the TanDEM-X repeat cycle. The ridge height measurement using InSAR methods has also been studied earlier (Dierking et al. 2017; Dammann et al. 2018b), particularly in the dm-scale accuracy of TanDEM-X-derived ice topography (Dammann et al. 2019b). In a more advanced work in PIII, extraction of relative HDMs between two InSAR-generated DEMs each with

an accuracy of one meter was done. The method is suitable to evaluate volumetric changes in ridges by integrating over the ridge. Such research helps to understand dynamics and formation of ridges, relationships between sea ice thickness, convergence, ridge development, density, size and morphology. However, extensive in-situ measurements are needed for validation. At present, TanDEM-X is the only single-pass satellite for sea ice topography but hopefully, it will change in future with an increasing number of upcoming satellites like TanDEM-L. (PIII).

8 Conclusions and directions for future work

In this dissertation, the benefits and possibilities of the utilization of InSAR (SAR Interferometry) imagery as a tool to detect cm-scale landfast ice displacements and topography have been investigated in the Baltic Sea and an Arctic region. Usage of InSAR features (coherence-magnitude and InSAR-phase) in sea ice classification have been evaluated and the results suggest that they provide informative features for automated sea ice classification by ice services.

PI was the first study with Sentinel-1 IW (Interferometric Wide swath) mode products that employed the InSAR technique for evaluating a long-term (12 days) landfast ice change in the Baltic Sea. The advantage of this work was in using a long temporal baseline to separate drift ice from landfast ice. A displacement of 40 cm in the LOS (Line Of Sight) was measured over an area of 400 km². This displacement was mainly due to the drift ice compression by southwest winds on the boundary of landfast ice. Sea ice displacement maps tell about landfast ice deformation that can be used to make sea ice hazard maps with cracking and the opening of leads which can be used by local people

for traveling and transportation on ice. Some low-coherence lines were caused by landfast ice fractures or ice routes.

The purpose of this study was to demonstrate that the InSAR approach is feasible to map landfast ice changes. This was achieved, although finding a stable and high coherence area with 12 days' temporal baseline was difficult due to snowfall, rain, ice growth, melting events and sea level variations. The temporal baseline decreased from 12 days to 6 days with the launch of Sentinel-1B in 2016 that increases possibilities of finding suitable study cases over the Baltic Sea landfast ice. In future work, a better ground truth data should be acquired for more detailed analysis. Another suggestion for future work has been to use interferograms from both ascending and descending orbits to solve two movement components (vertical and horizontal movements) (Tofani et al. 2013) and understand landfast ice processes better. Wang Zh et al. (2020) used our suggestion over the Baltic Sea and was successful in solving two movement components over the landfast ice by establishing the deformation transformed model according to the geometric relationship of multi-orbits deformation measurements. Then, the deformations of LOS direction were transformed into horizontal and vertical displacements.

The next study (PII) was done using different features of TanDEM-X (TerraSAR-X Add-on for Digital Elevation Measurement) including backscatter intensity, coherence-magnitude and InSAR-phase and their combinations for discriminating between different sea ice classes (ridged ice, close ice, very close ice, ship-track, thin smooth ice, heavily ridged ice and new ice) and open water over the Baltic Sea. RF (Random Forests) and ML (Maximum Likelihood) classifiers were applied. The best results were achieved by combined backscatter intensity & InSAR-phase and combined backscatter intensity & coherence-magnitude. RF was a preferable algorithm

due to short runtime, higher overall and user accuracies. The limitation of PII was a ramp over the classification map which was solved in PIV by removing the ramp.

PIV continued and expanded PII using the same experimental dataset. Different sea ice classes with a more detailed small-scale analysis of sea ice properties were used, and different features of TanDEM-X imagery were used for assessment of sea ice classes (undeformed ice, ridged ice, moderately deformed ice, brash ice, thick level ice, new ice) and open water. In addition to RF and ML classifiers, SVM (Support Vector Machine) classifier was applied over InSAR features and their combinations. The output of combined features had higher OA (Overall Accuracy) than single features. The RF and SVM classifiers were better than ML classifiers because of higher OAs, although, their processing times were higher. PIV showed the advantages of using interferometric features (coherence-magnitude & InSAR-phase) in combination with the backscatter intensity feature over a single backscatter intensity feature. The improvement of UAs (User's Accuracy) was much higher for most of the separated classes. Good discrimination of brash ice was not achieved, and therefore other methods should be applied. Also undeformed ice, ridged ice, moderately deformed ice, and brash ice had strong differences in UAs and PAs (Producer's Accuracies) between RF, ML and SVM. These differences were not remarkable for new ice, thick level ice and open water classes.

This study and PII were the first efforts for sea ice classification by backscatter intensity, coherence-magnitude, and InSAR-phase features at X-band, as well as in benchmarking RF and ML classifiers over all possible SAR (Synthetic Aperture Radar) feature combinations. The results proved InSAR to be helpful tool for sea ice classification in sea ice services as inputs to improve sea ice classification. Also, PII and PIV were successful in discrimination of between

new ice and open water which has been a challenge in sea ice classification due to similar backscattering values (Laanemäe et al. 2016; Geldsetzer and Yackel 2009). This success was due to using the bistatic InSAR imaging mode with no temporal decorrelation of InSAR coherence.

More cases in different weather conditions (e.g., wind speed induced roughness for open water) should be tested in future to improve the credibility of the present results. An other limitation is the sparsity of InSAR pairs with longer baselines to achieve smaller HoA (Height of Ambiguity), with nearly stable sea ice with no melting. Future opportunities can be offered by potential small-sat constellations now actively pursued by several companies including DLR (Deutsches Zentrum für Luft- und Raumfahrt), ICEYE or other datasets. As a future work, using various advanced texture feature extraction techniques GLCM (Gray-Level Co-occurrence Matrix) (Barber et al. 1993), autocorrelation methods (Karvonen 2012), wavelet-based features (Liu et al. 1997; Yu et al. 2002, Similä and Helminen 1995), Gabor wavelet techniques (Clausi 2002), MRF (Markov random fields) (Maillard et al. 2005; Clausi and Yue 2004; Deng and Clausi 2005) can be tested.

For the first time, assessing ridge formation and displacement over landfast ice using interferometric change detection was done in PIII. The phase signatures of two single-pass bistatic X-band SAR image pairs acquired by the TanDEM-X satellite near Utqiagvik, Alaska were analyzed. The elevation change result or HDM (Height Difference Map) was compared with backscatter intensity features, coastal radar imageries, and ice drift information generated by a SAR-based sea ice tracking algorithm. Four cases of ridge displacement and two cases of ridge formation were recognizable. Ridges were displaced from 0.6 to 3.7 km and ridge formations were the result of one meter vertically upward buildup. It seems possible to use the InSAR

technique to evaluate sea ice deformation and background mechanisms. This will help to understand sea ice properties across large spatial scales, which are difficult to determine based on in-situ or laboratory experiments. In addition, this method can be used in future to evaluate different forcing conditions created by ice, atmosphere and ocean under which various kind of ridges form and where/when convergence leads to ridge displacement, formation of new ridges, or development of existing features. Currently, retrieving or evaluating this kind of information is difficult.

InSAR can bring valuable information that can be used to better understand sea ice properties and stability, to apply in operational ice charting, and to further develop sea ice models. One of the limitations of this work was the lack of access to data for ice management and operational applications. Another limitation was the lack of suitable single-pass TanDEM-X datasets for sea ice topography research. Longer baselines, on the order of several hundred meters, would be more suitable for studying ridges but these were only available during the Science Phase in 2015. Similar datasets would be needed for further research, and opportunities offered by prospective small-sat constellations should be explored. In future work, in-situ measurements are needed for detailed accuracy assessment of this approach. In addition, it's worth studying various acquisition geometries and ice regimes like salinity, morphology and season to examine the potentials of this technique. This will help to evaluate the potential of volumetric changes that is important for porosity estimation, landfast ice stability, and possible impact on fixed structures and vessels.

References

- Amundrud, T. L., H. Melling, and R. G. Ingram. 2004. "Geometrical constraints on the evolution of ridged sea ice." *Journal of Geophysical Research Oceans* 109 (C6). DOI:[10.1029/2003JC002251](https://doi.org/10.1029/2003JC002251).
- Armstrong, T., B. Roberts, and C. Swithinbank. 1966. *Illustrated Glossary of Snow and Ice*. Cambridge, U.K: Scott Polar Research Institute.
- Arst, H., A. Erm, M. Lepparanta, and A. Reinart. 2006. "Radiative characteristics of icecovered freshwater and brackish water bodies." *In Proceedings of the Estonian Academy of Sciences Geology* 55 (1): 3-23. DOI:[10.3176/geol.2006.1.01](https://doi.org/10.3176/geol.2006.1.01).
- Askne, J., M. Leppäranta and T. Thompson. 1992. "Bothnian Experiment in Preparation for ERS-1, 1988 (BEPERS-88) – An Overview." *International Journal of Remote Sensing* 13(13): 2377–2398. DOI:[10.1080/01431169208904277](https://doi.org/10.1080/01431169208904277).
- Askne J., and W. Dierking. 2008. "Sea Ice Monitoring in the Arctic and Baltic Sea Using SAR." In: Barale V., Gade M. (eds) *Remote Sensing of the European Seas*. Springer, Dordrecht: 383-398. DOI:[10.1007/978-1-4020-6772-3_29](https://doi.org/10.1007/978-1-4020-6772-3_29).
- Aslan, G., Z. Çakir, L. Lasserre, R. Renard. 2018. "Analysis of Secular Ground Motions in Istanbul from a Long-Term InSAR Time-Series (1992-2017)." *Remote Sensing* 10 (3): 408. DOI:[10.3390/rs10030408](https://doi.org/10.3390/rs10030408).
- Aslan, G., C. Lasserre, Z. Çakir, S. Ergintav, S. Özarpaci, U. Dogan, R. Bilham, F. Renard. 2019. "Shallow creep along the 1999 Izmit earthquake rupture (Turkey) from GPS and high temporal resolution interferometric synthetic-aperture radar data (2011-2017)." *Journal of Geophysical Research: Solid Earth* 124: 2218–2236. DOI: [10.1029/2018JB017022](https://doi.org/10.1029/2018JB017022).

- Atkinson, P. M., and A. R. L. Tatnall. 1997. "Introduction Neural networks in remote sensing." *International Journal of Remote Sensing* 18 (4): 699-709. DOI:[10.1080/014311697218700](https://doi.org/10.1080/014311697218700).
- Balzter, H. 2017. *Earth Observation for Land and Emergency Monitoring*. New Jersey: John Wiley & Sons Inc.
- Bamler, R., P. Hartl. 1998. "Synthetic aperture radar interferometry." *Inverse Problems* 14, R1–R54.
- Barber, D. G., and E. F. LeDrew. 1991. "SAR Sea Ice Discrimination Using Texture Statistics: A Multivariate Approach." *Photogrammetric Engineering and Remote Sensing* 57 (4): 385–395. DOI:[10.1016/0169-2046\(91\)90082-W](https://doi.org/10.1016/0169-2046(91)90082-W).
- Barber, D. G., M. Shokr, E. Soulis, R. Fernandes, D. Flett, E. F. LeDrew. 1993. "A comparison of second order texture classifiers for SAR sea ice." *Photogrammetric Engineering & Remote Sensing* 59 (9):1397-140.
- Barker, A., G. Timco, and B. Wright. 2006. "Traversing grounded rubble fields by foot—Implications for evacuation." *Cold Regions Science and Technology* 46 (2): 79-99. DOI:[10.1016/j.coldregions.2006.06.001](https://doi.org/10.1016/j.coldregions.2006.06.001).
- Barry, R. G., R. E. Moritz, and J. C. Rogers. 1979. "The fast ice regimes of the Beaufort and Chukchi Sea coasts, Alaska." *Cold Regions Science and Technology* 1 (2): 129–152. DOI:[10.1016/0165-232X\(79\)90006-5](https://doi.org/10.1016/0165-232X(79)90006-5).
- Berg, A., and L. E. Eriksson. 2013. "Investigation of a hybrid algorithm for sea ice drift measurements using synthetic aperture radar images." *IEEE Transactions on Geoscience and Remote Sensing* 52 (8): 5023–5033. DOI:[10.1109/TGRS.2013.2286500](https://doi.org/10.1109/TGRS.2013.2286500).
- Berg, A., P. B. G. Dammert, and L. E. Eriksson. 2015. "X-Band Interferometric SAR Observations of Baltic Fast Ice." *IEEE Transactions on Geoscience and Remote Sensing* 53 (3): 1248–1256. DOI: [10.1109/TGRS.2014.2336752](https://doi.org/10.1109/TGRS.2014.2336752).

- Berglund, R., P. B. Eriksson. 2015. "National Ice Service Operations and Products around the World." In Book Cold Regions Science and Marine Technology, edited by Hayley H. Shen. France: UNESCO-EOLSS.
- Berthod, B., Z. Kato, S. Yu, J. Zerubia. 1996. "Bayesian image classification using Markov random fields." *Image and Vision Computing* 14 (4): 285-295. DOI:[10.1016/0262-8856\(95\)01072-6](https://doi.org/10.1016/0262-8856(95)01072-6).
- Bogdanov, A. V., S. Sandven, O. M. Johannessen, V. Y. Alexandrov, and L. P. Bobylev. 2005. "Multisensor Approach to Automated Classification of Sea Ice Image Data." *IEEE Transactions on Geoscience and Remote Sensing* 43 (7): 1648–1664. DOI:[10.1109/TGRS.2005.846882](https://doi.org/10.1109/TGRS.2005.846882).
- Breiman, L. 2001. "Random Forests." *Machine Learning* 45 (1): 5–32. DOI:[10.1023/A:1010933404324](https://doi.org/10.1023/A:1010933404324).
- Canny, J. 1986. "A computational approach to edge detection." *IEEE Transactions on Pattern Analysis and Machine Intelligence* 8(6): 679–698. DOI: [10.1109/TPAMI.1986.4767851](https://doi.org/10.1109/TPAMI.1986.4767851).
- Chunxia, Z., G. Linlin, E. Dongchen & Ch. Hsingchung. 2005. "A case study of using external DEM in InSAR DEM generation". *Geo-spatial Information Science* 8(1):14-18. DOI:[10.1007/BF02826985](https://doi.org/10.1007/BF02826985).
- Clausi, D. A. 2001. "Comparison and Fusion of Co-occurrence, Gabor, and MRF Texture Features for Classification of SAR Sea Ice Imagery." *Atmosphere Ocean* 39 (3): 183–194. DOI:[10.1080/07055900.2001.9649675](https://doi.org/10.1080/07055900.2001.9649675).
- Clausi, D. A. 2002. "An analysis of co-occurrence texture statistics as a function of grey level quantization." *Canadian Journal of Remote Sensing* 28 (1): 45–62. DOI: [10.5589/m02-004](https://doi.org/10.5589/m02-004).
- Clausi, D. A., and B. Yue. 2004. "Comparing Co-occurrence Probabilities and Markov Random Fields for Texture Analysis of SAR Sea Ice Imagery." *IEEE*

Transactions on Geoscience and Remote Sensing 42 (1): 215–228.
DOI:[10.1109/TGRS.2003.817218](https://doi.org/10.1109/TGRS.2003.817218).

Clausi, D. A., and Y. Zhao. 2002. “Rapid Extraction of Image Texture by Co-occurrence Using a Hybrid Data Structure.” *Computers & Geosciences* 28 (6): 763–774. DOI: [10.1016/S00983004\(01\)00108-X](https://doi.org/10.1016/S00983004(01)00108-X).

Clausi, D. A., and Y. Zhao. 2003. “Grey Level Co-occurrence Integrated Algorithm (GLCIA): A Superior Computational Method to Rapidly Determine Co-occurrence Probability Texture Features.” *Computers & Geosciences* 29 (7): 837–850. DOI: [10.1016/S00983004\(03\)00089-X](https://doi.org/10.1016/S00983004(03)00089-X).

Cox, G. F. N., and W. F. Weeks. 1983. “Equations for determining the gas and brine volumes in sea ice samples.” *Journal of Glaciology* 29 (102): 306–316. DOI:[10.1017/S0022143000008364](https://doi.org/10.1017/S0022143000008364).

Curlander, J. C., and R. N. McDonough. 1991. *Synthetic aperture radar: systems and signal processing*. United state: John Wiley & Sons.

Dammann, D. O., H. Eicken, F. Meyer, and A. Mahoney. 2016. “Assessing small-scale deformation and stability of landfast sea ice on seasonal timescales through L-band SAR interferometry and inverse modeling.” *Remote Sensing of Environment* 187: 492–504. DOI:[10.1016/j.rse.2016.10.032](https://doi.org/10.1016/j.rse.2016.10.032).

Dammann, D. O., L. B. Eriksson, A. R. Mahoney, C. W. Stevens, J. Sanden, H. Eicken, F. J. Meyer, and C.E. Tweedie. 2017. “Mapping Arctic Bottomfast Sea Ice Using SAR Interferometry.” *Remote Sensing* 10 (5): 720. DOI:[10.3390/rs10050720](https://doi.org/10.3390/rs10050720).

Dammann, D. O., H. Eicken, A. Mahoney, F. Meyer, S. Betcher. 2018a. “Assessing sea ice trafficability in a changing Arctic.” *Arctic* 71 (1): 59–75. DOI:[10.14430/arctic4701](https://doi.org/10.14430/arctic4701).

- Dammann, D. O., H. Eicken, A. R. Mahoney, E. Saiet, F. J. Meyer, and J. C. George. 2018b. "Traversing Sea Ice—Linking Surface Roughness and Ice Trafficability Through SAR Polarimetry and Interferometry." *IEEE Journal of Selected Topics in Applied Earth Observations and Remote Sensing* 11(2): 416–433. DOI:[10.1109/JSTARS.2017.2764961](https://doi.org/10.1109/JSTARS.2017.2764961).
- Dammann, D. O., L. E. B. Eriksson, A. R. Mahoney, H. Eicken, and F. J. Meyer. 2019a. "Mapping pan-Arctic landfast sea ice stability using Sentinel-1 interferometry." *Cryosphere* 13 (2): 557–577. DOI:[10.5194/tc-13-1-2019](https://doi.org/10.5194/tc-13-1-2019).
- Dammann, D. O., L. E. B. Eriksson, S. V. Nghiem, E. C. Pettit, N. T. Kurtz, J. G. Sonntag, T. E. Busche, F. J. Meyer, and A. R. Mahoney. 2019b. "Iceberg topography and volume classification using TanDEM-X interferometry." *Cryosphere* 13 (7):1861–1875. DOI:[10.5194/tc-13-1861-2019](https://doi.org/10.5194/tc-13-1861-2019).
- Dammert, P. B. G., M. Leppäranta, and J. Askne. 1998. "SAR Interferometry over Baltic Sea Ice." *International Journal of Remote Sensing* 19 (16): 3019–3037. DOI:[10.1080/014311698214163](https://doi.org/10.1080/014311698214163).
- Demchev, D., V. Volkov, E. Kazakov, P. F. Alcantarilla, S. Sandven, and V. Khmeleva. 2017. "Sea Ice Drift Tracking From Sequential SAR Images Using Accelerated-KAZE Features." *IEEE Transactions on Geoscience and Remote Sensing* 55(9): 5174 – 5184. DOI:[10.1109/TGRS.2017.2703084](https://doi.org/10.1109/TGRS.2017.2703084).
- Deng, H., and D. A. Clausi. 2005. "Unsupervised segmentation of synthetic aperture Radar sea ice imagery using a novel Markov random field model". *IEEE Transactions on Geoscience and Remote Sensing* 43 (3): 528–538. DOI:[10.1109/TGRS.2004.839589](https://doi.org/10.1109/TGRS.2004.839589).
- Devaraj, S., and K. Yarrakula. 2018. "InSAR based Deformation Mapping of Earthquake using Sentinel 1A Imagery". *Geocarto International* 35 (5): 1-17. DOI:[10.1080/10106049.2018.1544289](https://doi.org/10.1080/10106049.2018.1544289).

- Dierking, W. 1995. "Laser profiling of the ice surface topography during the Winter Weddell Gyre Study." *Journal of Geophysical research Oceans* 100 (C3): 4807–4820. DOI: [10.1029/94JC01938](https://doi.org/10.1029/94JC01938).
- Dierking, W. 2010. "Mapping of Different Sea Ice Regimes Using Images from Sentinel-1 and ALOS Synthetic Aperture Radar." *IEEE Transactions on Geoscience and Remote Sensing* 48 (3): 1045–1058. DOI:[10.1109/TGRS.2009.2031806](https://doi.org/10.1109/TGRS.2009.2031806).
- Dierking, W. 2013. "Sea Ice Monitoring by Synthetic Aperture Radar." *Oceanography* 26 (2): 100–111. DOI:[10.5670/oceanog.2013.33](https://doi.org/10.5670/oceanog.2013.33).
- Dierking, W., O. Lang, and T. Busche. 2017. "Sea Ice Local Surface Topography from Single-pass Satellite InSAR Measurements: A Feasibility Study." *The Cryosphere* 11: 1967–1985. DOI:[10.5194/tc-11-1967-2017](https://doi.org/10.5194/tc-11-1967-2017).
- Dierking, W., and C. Wesche. 2014. "C-Band Radar polarimetry–Useful for Detection of Icebergs in Sea Ice?" *IEEE Transactions on Geoscience and Remote Sensing* 52 (1): 25–37. DOI:[10.1109/TGRS.2012.2234756](https://doi.org/10.1109/TGRS.2012.2234756).
- Dinessen, F. 2017. "Operational multisensor sea ice concentration algorithm utilizing Sentinel-1 and AMSR 2 data." *In Proceedings of 19th EGU General Assembly*, Vienna, Austria, 23-28 April.
- Doke, R, M. Harada, K. Mannen, K. Itadera, and J. Takenaka. 2018. "InSAR analysis for detecting the route of hydrothermal fluid to the surface during the 2015 phreatic eruption of Hakone Volcano, Japan." *Earth Planets Space* 70: 63. DOI:[10.1186/s40623-018-0834-4](https://doi.org/10.1186/s40623-018-0834-4).
- Druckenmiller, M. L. 2011. "Alaska Shorefast Ice: Interfacing Geophysics with Local Sea Ice Knowledge and Use." PhD diss., University of Alaska Fairbanks, Fairbanks, AK, USA.

- Druckenmiller, M. L., H. Eicken, J. C. George, and L. Brower. 2013. "Trails to the whale: Reflections of change and choice on an Iñupiat icescape at Barrow, Alaska." *Polar Geography* 36 (1-2): 5–29. DOI:[10.1080/1088937X.2012.724459](https://doi.org/10.1080/1088937X.2012.724459).
- Dyrcz, C. 2020. "Ice Drift in the Arctic Ocean." *Scientific Journal of Polish Naval Academy* 222 (3): 68–85. DOI:[10.2478/sjpna-2020-0011](https://doi.org/10.2478/sjpna-2020-0011).
- Elachi, Ch. 1988. *Spaceborne radar remote sensing: applications and techniques*. New York: IEEE Press.
- Eicken, H. and M. A. Lange. 1989. "Development and properties of sea ice in the coastal regime of the southern Weddell Sea." *Journal of Geophysical Research Atmospheres* 94 (C6): 8193-8206. DOI:[10.1029/JC094iC06p08193](https://doi.org/10.1029/JC094iC06p08193).
- Eicken, H., A. L. Lovecraft, and M. L. Druckenmiller. 2009. "Sea-ice system services: A framework to help identify and meet information needs relevant for Arctic observing networks." *Arctic* 62 (2): 119–136. DOI:[10.14430/arctic126](https://doi.org/10.14430/arctic126).
- Eriksson, L. E. B., K. Borenäs, W. Dierking, A. Berg, M. Santoro, P. Pemberton, H. Lindh, and B. Karlson. 2010. "Evaluation of New Spaceborne SAR Sensors for Sea-ice Monitoring in the Baltic Sea." *Canadian Journal of Remote Sensing* 36 (sup1): S56–S73. DOI:[10.5589/m10-020](https://doi.org/10.5589/m10-020).
- Farrell, S. L., T. Markus, R. Kwok, and L. Connor. 2011. "Laser altimetry sampling strategies over sea ice." *Annal Glaciology* 52 (57): 69–76. DOI:[10.3189/172756411795931660](https://doi.org/10.3189/172756411795931660).
- Finnish Ice Service (FIS) of the Finnish Meteorological Institute (FMI). Bathymetry, Ice Thickness, Ice Condition Information and Ice Chart 2012 are received from FMI. 2012. Available online: <http://en.ilmatieteenlaitos.fi/>.

- Finnish Ice Service (FIS) of the Finnish Meteorological Institute (FMI). Bathymetry, Ice Thickness, Ice Condition Information and Ice Chart 2015 are received from FMI. 2015. Available online: <http://en.ilmatieteenlaitos.fi/>.
- Friedrichs, F., and C. Igel. 2005. "Evolutionary Tuning of Multiple SVM Parameters." *Neurocomputing* 64: 107–117. DOI:[10.1016/j.neucom.2004.11.022](https://doi.org/10.1016/j.neucom.2004.11.022).
- Gabriel, A. K., R. M. Goldstein, and H. A. Zebker. 1989. "Mapping small elevation changes over large areas: differential radar interferometry." *Journal of Geophysical Research* 94 (B7): 9183–9191. DOI:[10.1029/JB094iB07p09183](https://doi.org/10.1029/JB094iB07p09183).
- Gegiuc, A., M. Similä, J. Karvonen, M. Lensu, M. Mäkynen, and J. Vainio. 2018. "Estimation of Degree of Sea Ice Ridging Based on Dual-Polarized C-band SAR Data." *The Cryosphere* 12 (1): 343–364. DOI:[10.5194/tc-12-343-2018](https://doi.org/10.5194/tc-12-343-2018).
- Geldsetzer, T., and J. Yackel. 2009. "Sea Ice Type and Open Water Discrimination Using Dual Co-polarized C-band SAR." *Canadian Journal of Remote Sensing* 35 (1): 73–84. DOI:[10.5589/m08-075](https://doi.org/10.5589/m08-075).
- George, J. C., H. P. Huntington, K. Brewster, H. Eicken, D. W. Norton, and R. Glenn. 2004. "Observations on Shorefast ice dynamics in Arctic Alaska and the responses of the inupiat hunting community." *Arctic* 57 (4): 363–374. DOI:[10.14430/arctic514](https://doi.org/10.14430/arctic514).
- Geymen, A. 2012. "Digital elevation model (DEM) generation using the SAR interferometry technique". *Arabian Journal of Geosciences* 7(2): 827–837. DOI:[10.1007/s12517-012-0811-3](https://doi.org/10.1007/s12517-012-0811-3).
- Gidudu, A., H. Greg, and M. Tshilidzi. 2007. "Classification of Images Using Support Vector Machines." arXiv preprint [arXiv:0709.3967](https://arxiv.org/abs/0709.3967).

- Goldstein, R. M., C. L. Werner. 1998. "Radar interferogram filtering for geophysical applications." *Geophysical Research Letters* 25 (2): 4035–4038. DOI: [10.1029/1998GL900033](https://doi.org/10.1029/1998GL900033).
- Goldstein, R., N. Osipenko, and M. Leppäranta, 2000. "Classification of large-scale sea-ice structures based on remote sensing imagery." *Geophysica* 36 (1-2): 95-109.
- Goldstein, R.V., N. M. Osipenko, and M. Leppäranta. 2009. "Relaxation scales and the structure of fractures in the dynamics of sea ice." *Cold Regions Science and Technology* 58(1-2): 29–35. DOI:[10.1016/j.coldregions.2009.03.003](https://doi.org/10.1016/j.coldregions.2009.03.003).
- Granskog, M., H. Kaartokallio, H. Kuosa, D. N. Thomas, and J. Vainio. 2006. "Sea ice in the Baltic Sea- A review." *Estuarine Coastal and Shelf Science* 70 (1-2): 145-160. DOI:[10.1016/j.ecss.2006.06.001](https://doi.org/10.1016/j.ecss.2006.06.001).
- Griebel, J., and W. Dierking. 2017. "A Method to Improve High-Resolution Sea Ice Drift Retrievals in the Presence of Deformation Zones." *Remote Sensing* 9, 718. DOI:[10.3390/rs9070718](https://doi.org/10.3390/rs9070718).
- Grönvall, H., and A. Seinä. 1999. "The IMSI results in the Baltic Sea - digital sea ice products to the users at sea." *In Proceedings of POAC '99*, Helsinki, Finland, August 23-27.
- Haas, C., S. Hendricks, and M. Doble. 2006. "Comparison of the sea-ice thickness distribution in the Lincoln Sea and adjacent Arctic Ocean in 2004 and 2005." *Annals of Glaciology* 44: 247–252. DOI:[10.3189/172756406781811781](https://doi.org/10.3189/172756406781811781).
- Haas, C., S. Hendricks, H. Eicken, and A. Herber. 2010. "Synoptic airborne thickness surveys reveal state of Arctic sea ice cover." *Geophysical Research Letter* 37 (9): L09501. DOI:[10.1029/2010GL042652](https://doi.org/10.1029/2010GL042652).
- Hamidi, D., S. Lehner, T. König, and A. Pleskachevsky. 2011. "On the Sea Ice Motion Estimation with Synthetic Aperture Radar." *In Proceedings of the 4th*

TerraSAR-X Meeting 2011, Oberpfaffenhofen, Germany, 14–16 February 2011, Volume Vortrags-Nr. CAL0166, pp. 1–10. Item URL in elib: <https://elib.dlr.de/72252/>.

Han, Y., J. Ren, Z. Hong, Y. Zhang, L. Zhang, W. Meng, and Q. Gu. 2015. “Active Learning Algorithms for the Classification of Hyperspectral Sea Ice Images.” *Mathematical Problems in Engineering* 2015. Article ID: 124601. DOI:[10.1155/2015/124601](https://doi.org/10.1155/2015/124601). 2015:1–10.

Hanssen, R. F. 2001. *Radar interferometry – Data Interpretation and Error Analysis*. New York, NY, USA: Kluwer Academic Publishers.

Heerman, P. D., and N. Khazenie. 1992. “Classification of Multispectral Remote Sensing Data Using a Back-Propagation Neural Network.” *IEEE Transactions on Geoscience and Remote Sensing* 30 (1): 81–88. DOI:[10.1109/36.124218](https://doi.org/10.1109/36.124218).

Henderson, F. M., and A. J. Lewis. 1998. *Principles and Application of Imaging Radar. Manual of Remote Sensing*. New York: John Wiley and Sons.

Heo, E.-S., M.-K. Sung, S.-I. An, and Y.-M. Yang. 2021. “Decadal phase shift of summertime Arctic dipole pattern and its nonlinear effect on sea ice extent.” *International Journal of Climatology* 41(9): 4732–4742. DOI: <https://doi.org/10.1002/joc.7097>.

Holmes, Q. A., D. R. Nuesch, and R. A. Shuchman. 1984. “Textural Analysis and Real-Time Classification of Sea-Ice Types Using Digital SAR Data.” *IEEE Transactions on Geoscience and Remote Sensing* GE-22 (2): 113–120. DOI:[10.1109/TGRS.1984.350602](https://doi.org/10.1109/TGRS.1984.350602).

Horner, R., S. F. Ackley, G. S. Dieckmann, B. Gulliksen, T. Hoshiai, L. Legendre, I. A. Melnikov, W. S. Reeburgh, M. Spindler and C. W. Sullivan. 1992. “Ecology of sea ice biota - 1. Habitat, terminology, and methodology.” *Polar Biology* 12 (3-4): 417-427. DOI:[10.1007/BF00243113](https://doi.org/10.1007/BF00243113).

- Hutter, N., L. Zampieri, and M. Losch. “Leads and ridges in Arctic sea ice from RGPS data and a new tracking algorithm.” *The Cryosphere* 13 (2): 627–645. DOI:[10.5194/tc-13-627-2019](https://doi.org/10.5194/tc-13-627-2019), 2019.
- Hyypä, J., and M. Hallikainen. 1992. “Classification of low-salinity sea ice types by ranging scatterometer.” *International Journal of Remote Sensing* 13 (13): 2399–2413. DOI:[10.1080/01431169208904278](https://doi.org/10.1080/01431169208904278).
- Ikävalko, J. 1997. “Studies of nanoflagellate communities in the sea ice of the Baltic and the Greenland Sea.” PhD diss., University of Helsinki, Helsinki, Finland.
- JCOMM Expert Team on Sea Ice. 2017. *Sea ice information services of the world, Edition 2017*. Geneva, Switzerland, World Meteorological Organization, 103pp. (WMO-No.574). DOI:[10.25607/OBP-1325](https://doi.org/10.25607/OBP-1325).
- Jevrejeva, S. 2001. “Severity of winter seasons in the northern Baltic Sea between 1529 and 1990: reconstruction and analysis.” *Climate Research* 17 (1): 55–62. DOI:[10.3354/cr017055](https://doi.org/10.3354/cr017055).
- Jevrejeva, S., V. V. Drabkin, J. Kostjukov, A. A. Lebedev, M. Leppäranta, Ye. U. Mironov, N. Schmelzer, and M. Sztobryn. 2004. “Baltic Sea ice seasons in the twentieth century.” *Climate Research* 25 (3): 217–227. DOI:[10.3354/cr025217](https://doi.org/10.3354/cr025217).
- Jevrejeva, S. and J. C. Moore. 2001. “Singular spectrum analysis of Baltic Sea ice conditions and large-scale atmospheric patterns since 1708,” *Geophysical Research Letters* 28 (23): 4503–4506. DOI:[10.1029/2001gl013573](https://doi.org/10.1029/2001gl013573).
- Jones, J. M. 2013. “Landfast Sea Ice Formation and Deformation Near Barrow.” Master diss., University of Alaska Fairbanks, Fairbanks, AK, USA.
- Jones, J., H. Eicken, A. Mahoney, M. V. Rohith, Ch. Kambhamettu, Y. Fukamachi, and K. Ohshima, J. C. George. 2016. “Landfast sea ice breakouts: Stabilizing

ice features, oceanic and atmospheric forcing at Barrow, Alaska.” *Continental Shelf Research* 126: 50–63. DOI:[10.1016/j.csr.2016.07.015](https://doi.org/10.1016/j.csr.2016.07.015).

Karvonen, J. 2004. “Baltic Sea Ice SAR segmentation and classification using modified pulse-coupled neural networks.” *IEEE Transactions on Geoscience and Remote* 42 (7):1566-1574. DOI:[10.1109/TGRS.2004.828179](https://doi.org/10.1109/TGRS.2004.828179).

Karvonen, J. 2010. “C-band sea ice SAR classification based on segmentwise edge features.” In *Geoscience and Remote Sensing New Achievements*, edited by P. Imperatore & D. Riccio. Croatia: IntechOpen. DOI:[10.5772/9093](https://doi.org/10.5772/9093).

Karvonen, J. 2012. “Operational SAR-based Sea Ice Drift Monitoring over the Baltic Sea.” *Ocean Science* 8 (4): 473–483. DOI:[10.5194/os-8-473-2012](https://doi.org/10.5194/os-8-473-2012).

Karvonen, J. 2014. “A sea ice concentration estimation algorithm utilizing radiometer and SAR data.” *Cryosphere* 8 (5): 1639–1650. DOI:[10.5194/tc-8-1639-2014](https://doi.org/10.5194/tc-8-1639-2014).

Karvonen, J. 2017. “Baltic Sea ice concentration estimation using SENTINEL-1 SAR and AMSR2 microwave radiometer data.” *IEEE Transactions on Geoscience and Remote Sensing* 55 (5): 2871–2883. DOI:[10.1109/TGRS.2017.2655567](https://doi.org/10.1109/TGRS.2017.2655567).

Karvonen, J., M. Similä, J. Haapala, C. Haas, and M. Mäkynen. 2004. “Comparison of SAR data and operational sea ice products to EM ice thickness measurements in the Baltic Sea.” In *Processing of IEEE International Geoscience and Remote Sensing Symposium*, Anchorage, Alaska, USA, 20-24 Sept. DOI:[10.1109/IGARSS.2004.1370333](https://doi.org/10.1109/IGARSS.2004.1370333).

Karvonen, J., M. Similä, I. Heiler. 2003. “Ice thickness estimation using SAR data and ice thickness history.” In *Processing of IEEE International Geoscience and Remote Sensing Symposium*, Toulouse, France, 21-25 July. DOI:[10.1109/IGARSS.2003.1293683](https://doi.org/10.1109/IGARSS.2003.1293683).

- Karvonen, J., M. Similä, and M. Mäkynen. 2005. "Open water detection from Baltic Sea ice Radarsat-1 SAR imagery." *IEEE Geoscience and Remote Sensing Letters* 2 (3): 275–279. DOI:[10.1109/LGRS.2005.847930](https://doi.org/10.1109/LGRS.2005.847930).
- Kim, J. W., D-j. Kim, and B. J. Hwang. 2010. "Estimation of sea ice thickness in the Arctic Sea using polarimetric parameters of C- and X-band space-borne SAR data." *In Processing of IEEE International Geoscience and Remote Sensing Symposium*. Honolulu, HI, USA, 25-30 July. DOI:[10.1109/IGARSS.2010.5650103](https://doi.org/10.1109/IGARSS.2010.5650103).
- Krieger, G., I. Hajnsek, K. P. Papathanassiou, M. Younis, and A. Moreira. 2010. "Interferometric Synthetic Aperture Radar (SAR) Missions Employing Formation Flying." *Proceedings of the IEEE* 98(5): 816–843. DOI:[10.1109/JPROC.2009.2038948](https://doi.org/10.1109/JPROC.2009.2038948).
- Krieger, G., A. Moreira, H. Fielder, I. Hajnsek, M. Werner, M. Younis, and M. Zink. 2007. "TanDEM-X: A satellite formation for high-resolution SAR interferometry." *IEEE Transactions on Geoscience and Remote Sensing* 45 (11): 3317 – 3341. DOI:[10.1109/TGRS.2007.900693](https://doi.org/10.1109/TGRS.2007.900693).
- Kuraoka, S., Y. Nakashima, R. Doke and K. Mannen. 2018. "Monitoring ground deformation of eruption center by ground-based interferometric synthetic aperture radar (GB-InSAR): a case study during the 2015 phreatic eruption of Hakone volcano". *Earth, Planets and Space* 70 (1): 181. DOI:[10.1186/s40623-018-0951-0](https://doi.org/10.1186/s40623-018-0951-0).
- Kwok, R., G. Spreen, and S. Pang. 2013. "Arctic Sea Ice Circulation and Drift Speed: Decadal Trends and Ocean Currents." *Journal of Geophysical Research Atmospheres* 118 (5): 2408–2425. DOI:[10.1002/jgrc.20191](https://doi.org/10.1002/jgrc.20191).
- Kwok, R., H. J. Zwally, and D. Yi. 2004. "ICESat observations of Arctic sea ice: A first look." *Geophysical Research Letter* 31 (16): 1–5. DOI:[10.1029/2004GL020309](https://doi.org/10.1029/2004GL020309).

- Laanemäe, K., R. Uiboupin, and S. Rikka. 2016. "Sea Ice Type Classification in the Baltic Sea from TanDEM-X Imagery." In *Proceedings of EUSAR: 11th European Conference on Synthetic Aperture Radar*, Hamburg, Germany, 6-9 June.
- Laidre, K. L., I. Stirling, L. F. Lowry, Ø. Wiig, M. P. Heide-Jørgensen, and S. H. Ferguson. 2008. "Quantifying the sensitivity of arctic marine mammals to climate-induced habitat change." *Ecological Applications* 18 (2): S97-S125. DOI:[10.1890/06-0546.1](https://doi.org/10.1890/06-0546.1).
- Leppäranta, M. 2009. "Sea ice dynamics." In *Encyclopedia of Ocean Sciences* edited by John H. Steele. Steve Thorpe, Karl Turekian. Boston: Elsevier Academic Press.
- Leppäranta, M. 2011. *The drift of sea ice*, 2nd ed. Heidelberg, Germany: Springer-Praxis.
- Leppäranta, M. 2013. "Land-ice interaction in the Baltic Sea." *Estonian Journal of Earth Sciences* 62 (1): 2–15. DOI:[10.3176/earth.2013.01](https://doi.org/10.3176/earth.2013.01).
- Leppäranta, M., and R. Hakala. 1992. "The Structure and Strength of First-year Ice Ridges in the Baltic Sea." *Cold Regions Science and Technology* 20 (3): 295–311. DOI:[10.1016/0165232X\(92\)90036-T](https://doi.org/10.1016/0165232X(92)90036-T).
- Leppäranta, M., R. Kuittinen, and J. Askne. 1992. "BEPERS pilot study: an experiment with X-band synthetic aperture radar over Baltic Sea ice." *Journal of Glaciology* 38 (128): 23-35. DOI:[10.3189/s0022143000009564](https://doi.org/10.3189/s0022143000009564).
- Leppäranta, M., and T. Manninen. 1988. *The Brine and Gas Content of Sea Ice with Attention to Low Salinities and High Temperatures*. Finnish Institute of Marine Research. Internal Report 2, 14 pp.
- Leppäranta, M., K. Myrberg. 2009. *Physical Oceanography of the Baltic Sea*. United States: Springer.

- Leppäranta, M., Y. Sun, and J. Haapala. 1998a. "Comparisons of Sea-Ice Velocity Fields from ERS-1 SAR and a Dynamic Model." *Journal of Glaciology* 44 (147): 248–262. DOI:[10.3189/S0022143000002598](https://doi.org/10.3189/S0022143000002598).
- Leppäranta, M., M. Tikkanen and, P. Shemeikka. 1998b. "Observations of ice and its sediments on the Baltic coast." *Nordic Hydrology* 29 (3): 199–220. DOI:[10.2166/nh.1998.0011](https://doi.org/10.2166/nh.1998.0011).
- Liu, A. K., B. Holt, and P. W. Vachon. 1991. "Wave Propagation in the Marginal Ice Zone: Model Predictions and Comparisons with Buoy and Synthetic Aperture Radar Data." *Journal of Geophysical Research* 96 (C3): 4605–4621. DOI:[10.1029/90JC02267](https://doi.org/10.1029/90JC02267).
- Liu, A.K., S. Martin, and R. Kwok. 1997. "Tracking of ice edges and ice floes by wavelet analysis of SAR images." *Journal of Atmospheric and Oceanic Technology* 14 (5): 1187–1198. DOI:[10.1175/1520-0426\(1997\)014<1187:TOIEAI>2.0.CO;2](https://doi.org/10.1175/1520-0426(1997)014<1187:TOIEAI>2.0.CO;2).
- Madjidian J., S. Björk, A. Nilsson, T. Halén. 2013. *CLEANSHIP – final project report. CLEAN-SHIP Project Report*. Interes sources: <http://www.cleanship-project.eu/>.
- Mahoney, A.R. 2012. Sea ice conditions in the Chukchi and Beaufort Seas. Prepared by Andrew r. Mahoney November 2012 for The Pew Charitable Trusts, Fairbanks: University of Alaska Fairbanks.
- Mahoney, A. R., H. Eicken, Y. Fukamachi, K. I. Ohshima, D. Simizu, C. Kambhamettu, M. Rohith, S. Hendricks, and J. Jones. 2015. "Taking a look at both sides of the ice: Comparison of ice thickness and drift speed as observed from moored, airborne and shore-based instruments near Barrow, Alaska." *Annals of Glaciology* 56 (69): 363–372. DOI:[10.3189/2015AoG69A565](https://doi.org/10.3189/2015AoG69A565).

- Mahoney, A., H. Eicken, A. Graves-Gaylord, and L. Shapiro. 2007a. "Alaska landfast sea ice: Links with bathymetry and atmospheric circulation." *Journal of Geophysical Research Atmospheres* 112 (C2): 1–18. DOI:[10.1029/2006JC003559](https://doi.org/10.1029/2006JC003559).
- Mahoney, A. R., H. Eicken, A. G. Gaylord and R. Gens. 2014. "Landfast sea ice extent in the Chukchi and Beaufort Seas: The annual cycle and decadal variability." *Cold Regions Science and Technology* 103: 41–56. DOI: [10.1016/j.coldregions.2014.03.003](https://doi.org/10.1016/j.coldregions.2014.03.003).
- Mahoney, A., H. Eicken, and L. Shapiro. 2007b. "How fast is landfast sea ice? A study of the attachment and detachment of nearshore ice at Barrow, Alaska." *Cold Regions Science and Technology* 47(3): 233–255. DOI:[10.1016/j.coldregions.2006.09.005](https://doi.org/10.1016/j.coldregions.2006.09.005).
- Maillard, P., D. A. Clausi, and H. Deng. 2005. "Map-guided sea ice segmentation and classification using SAR imagery and a MRF segmentation scheme." *IEEE Transactions on Geoscience and Remote Sensing* 43 (12): 2940–2951. DOI:[10.1109/TGRS.2005.857897](https://doi.org/10.1109/TGRS.2005.857897).
- Mäkynen, M., and M. Hallikainen. 2004. "Investigation of C-and X-band Backscattering Signatures of Baltic Sea Ice." *International Journal of Remote Sensing* 25 (11): 2061–2086. DOI:[10.1080/01431160310001647697](https://doi.org/10.1080/01431160310001647697).
- Maslanik, J., J. Stroeve, C. Fowler, and W. Emery. 2011. "Distribution and trends in Arctic sea ice age through spring 2011." *Geophysical Research Letter* 38 (13). DOI:[10.1029/2011GL047735](https://doi.org/10.1029/2011GL047735).
- Masterson, D. M. 2009. "State of the art of ice bearing capacity and ice construction." *Cold Regions Science and Technology* 58 (3): 99–112. DOI:[10.1016/j.coldregions.2009.04.002](https://doi.org/10.1016/j.coldregions.2009.04.002).

- Maurer, E., R. Kahle, F. Mrowka, G. Morfill, A. Ohndorf, and S. Zimmermann. 2016. "Operational Aspects of the TanDEM-X Science Phase," *In Proceedings of 14th International Conference on Space Operations*, Daejeon, Korea, 16–20 May 2016. AIAA 2016–2459. DOI:[10.2514/ 6.2016-2459](https://doi.org/10.2514/6.2016-2459).
- Meyer, F. J., A. R. Mahoney, H. Eicken, C. L. Denny, H. C. Druckenmiller, and S. Hendricks. 2011. "Mapping arctic Landfast-ice extent using L-band synthetic aperture radar interferometry." *Remote Sensing of Environment* 115 (12): 3029–3043. DOI:[10.1016/j.rse.2011.06.006](https://doi.org/10.1016/j.rse.2011.06.006).
- Moreira, A., P. Prats-Iraola, M. Younis, G. Krieger, I. Hajnsek, and K. P. Papathanassiou. 2013. "A Tutorial on Synthetic Aperture Radar." *IEEE Geoscience and Remote Sensing Magazine* 1 (1): 6–43. DOI:[10.1109/MGRS.2013.2248301](https://doi.org/10.1109/MGRS.2013.2248301).
- Muckenhuber, S., A. A. Korosov, and S. Sandven. 2016. "Open-source feature-tracking algorithm for sea ice drift retrieval from Sentinel-1 SAR imagery." *Cryosphere* 10 (2): 913–925. DOI:[10.5194/tc-10-913-2016](https://doi.org/10.5194/tc-10-913-2016).
- Nakamura, K., H. Wakabayashi, S. Uto, K. Naoki, F. Nishio, and S. Uratsuka. 2006. "Sea-ice thickness retrieval in the Sea of Okhotsk using dual-polarization SAR data," *Annals of Glaciology* 44: 261–268. DOI:[10.3189/172756406781811420](https://doi.org/10.3189/172756406781811420).
- NOAA. How does sea ice affect global climate? National Ocean Service website, <https://oceanservice.noaa.gov/facts/sea-ice-climate.html>, 26/02/21.
- Onstott, R. G. 1992. "SAR and scatterometer signatures of sea ice." In *Microwave Remote Sensing of Sea Ice* edited by F. D. Carsey. Washington, DC, USA: American Geophysical Union
- OTB Team. 2018. *OTB Cook Book Documentation*. Available online: <https://www.orfeo-toolbox.org/packages/OTBCookBook.pdf>.

- Overland, J. E., J. A. Francis, E. Hanna, and M. Wang. 2012. "The recent shift in early summer Arctic atmospheric circulation." *Geophysical Research Letters* 39 (19): L19804. DOI:[10.1029/2012GL053268](https://doi.org/10.1029/2012GL053268).
- Overland, J. E., and M. Wang. 2013, "When will the summer Arctic be nearly sea ice free? " *Geophysical Research Letters* 40(10): 2097–2101. DOI:[10.1002/grl.50316](https://doi.org/10.1002/grl.50316).
- Palosuo, E. 1963. The Gulf of Bothnia in winter II. Freezing and ice forms, *Merentutkimuslaitoksen Julk.*, 209, 42–64.
- Pedregosa, F., G. Varoquaux, A. Gramfort, V. Michel, B. Thirion. 2011. "Scikit-learn: Machine Learning in Python." *Journal of Machine Learning Research* 12: 2825-2830. [arXiv:1201.0490](https://arxiv.org/abs/1201.0490).
- Potter, R. E., J. T. Walden, and R. A. Haspel. 1981. "Design and Construction of Sea Ice Roads in The Alaskan Beaufort Sea." Paper presented at the Offshore Technology Conference, Houston, Texas, May 4–7. DOI:[10.4043/4080-MS](https://doi.org/10.4043/4080-MS).
- Ressel, R., A. Frost, and S. Lehner. 2015. "A Neural Network-Based Classification for Sea Ice Types on X-Band SAR Images." *IEEE Journal of Selected Topics in Applied Earth Observations and Remote Sensing* 8 (7): 3672–3680. DOI: [10.1109/JSTARS.2015.2436993](https://doi.org/10.1109/JSTARS.2015.2436993).
- Richards, J. A. 2009. "Remote sensing with imaging radar." In *interferometric and tomographics*. New York: Springer.
- Richards J.A., and Jia X. 2006. *Remote Sensing Digital Image Analysis*. Heidelberg: Springer.
- Rosen, P. A., S. Hensley, I. R. Joughin, F. K. Li, S. N. Madsen, E. Rodríguez, and R. M. Goldstein. 2000. "Synthetic Aperture Radar Interferometry." In *Proceedings of the IEEE* 88(3): 333–382. DOI:[10.1109/5.838084](https://doi.org/10.1109/5.838084).

- Sadeghi, Y., B. St-Onge, B. Leblon, M. Simard, and K. Papathanassiou. 2014. "Mapping Forest Canopy Height Using TanDEM-X DSM and Airborne LiDAR DTM." *In Proceedings of IEEE Geoscience and Remote Sensing Symposium*, Quebec City, QC, Canada, 13-18 July. DOI:[10.1109/IGARSS.2014.6946359](https://doi.org/10.1109/IGARSS.2014.6946359).
- Sandven, S., and O. M. Johannessen. 2006. "Sea Ice Monitoring by Remote Sensing." *In Remote Sensing of the Marine Environment, Manual of Remote Sensing* edited by J. Gower. Maryland, USA: American Society for Photogrammetry and Remote Sensing.
- Schmitt, M. 2014. "Reconstruction of Urban Surface Models from Multi-Aspect and Multi-Baseline Interferometric SAR." PhD diss., Technische Universität München.
- Seinä, A., H. Grönvall, S. Kalliosaari, J. Vainio, P. Eriksson, and J.-E. Lundqvist. 2001. *WMO sea ice nomenclature: terminology for the Baltic Sea in English, Finnish and Swedish*. MERI Report No. 43, Finnish Marine Research Institute, Finland.
- Seinä, A., P. Mälkki, and H. Grönvall. 2006. "GSE programme benefits to Baltic Sea ice navigation." *In Proceedings of the 4th EuroGOOS*, Brest, France, 6–9 June 2005, pp. 667-672.
- Seinä, A., and E. Palosuo. 1996. *The classification of the maximum annual extent of ice cover in the Baltic Sea 1720–1995*. MERI-Report Series of the Finnish Institute of Marine Res 27:79–91.
- Seinä, A., and J. Peltola. 1991. *Duration of Ice Season and Statistics of Fast Ice Thickness along the Finnish Coast 1961-1990*. Helsinki: Merentutkimuslaitos.

- Shen, H., W. Perrie, Y. Hu, and Y. He. 2018. "Remote sensing of waves propagating in the marginal ice zone by SAR." *Journal of Geophysical Research: Oceans* 123 (1): 189–200. DOI:[10.1002/2017jc013148](https://doi.org/10.1002/2017jc013148).
- Shokr, M. E. 1991. "Evaluation of second-order texture parameters for sea ice classification from radar images." *Journal of Geophysical Research* 96: 10625–10640. DOI:[10.1029/91JC00693](https://doi.org/10.1029/91JC00693).
- Shokr, M. E, and N. Sinha. 2015. *Sea Ice: Physics and Remote Sensing*. Washington: American Geophysical Union.
- Similä, M., M. Leppäranta, H. B. Granberg and, J. E. Lewis. 1992. "The relationship between SAR imagery and regional sea ice ridging characteristics from BEPERS-88." *International Journal of Remote Sensing* 13 (13): 2415–2432. DOI:[10.1080/01431169208904279](https://doi.org/10.1080/01431169208904279).
- Similä, M., and J. Helminen. 1995. "The identification of the deformed sea ice fields from ERS-1 SAR image by wavelets." In *Proceedings of the IEEE Geoscience and Remote Sensing Symposium*, Firenze, Italy, 10–14 July.
- Skolnik, M. I. "Radar." *Encyclopedia Britannica*, Invalid Date. <https://www.britannica.com/technology/radar>.
- Soh, L.-K., and C. Tsatsoulis. 1999. "Texture Analysis of SAR Sea Ice Imagery Using Gray Level Co-occurrence Matrices." *IEEE Transactions on Geoscience and Remote Sensing* 37 (2): 780–795. DOI:[10.1109/36.752194](https://doi.org/10.1109/36.752194).
- Soh, L.-K., C. Tsatsoulis, C. Bertoia, and D. Gineris. 2004. "ARKTOS: An Intelligent System for SAR Sea Ice Image Classification." *IEEE Transactions on Geoscience and Remote Sensing* 42 (1): 229–248. DOI:[10.1109/TGRS.2003.817819](https://doi.org/10.1109/TGRS.2003.817819).

- Solberg, S., R. Astrup, J. Breidenbach, B. Nilsen, and D. Weydahl. 2013. "Monitoring Spruce Volume and Biomass with InSAR Data from TanDEM-X." *Remote Sensing of Environment* 139: 60–67. DOI:[10.1016/j.rse.2013.07.036](https://doi.org/10.1016/j.rse.2013.07.036).
- Solberg, S., D. J. Weydahl, and R. Astrup. 2015. "Temporal Stability of X-Band Single-Pass InSAR Heights in a Spruce Forest: Effects of Acquisition Properties and Season." *IEEE Transactions on Geoscience and Remote Sensing* 53 (3): 1607–1614. DOI:[10.1109/TGRS.2014.2346473](https://doi.org/10.1109/TGRS.2014.2346473).
- Spreen, G., R. Kwok, and D. Menemenlis. 2011. "Trends in Arctic sea ice drift and role of wind forcing: 1992–2009." *Geophysical Research Letters* 38 (19): L19501. DOI: [10.1029/2011GL048970](https://doi.org/10.1029/2011GL048970).
- Stumpf, A., and N. Kerle. 2011. "Object-oriented Mapping of Landslides Using Random Forests." *Remote Sensing of Environment* 115 (10): 2564–2577. DOI:[10.1016/j.rse.2011.05.013](https://doi.org/10.1016/j.rse.2011.05.013).
- Sun, Y. 1996. "Automatic ice motion retrieval from ERS-1 SAR images using the optical flow method." *International Journal of Remote Sensing* 17 (11): 2059–2087. DOI:[10.1080/01431169608948759](https://doi.org/10.1080/01431169608948759).
- Timokhov, L.A. 1998. "Ice dynamics models." In *physics of Ice-covered Seas* (Vol. 1, pp.343–380). Helsinki University Press.
- Timco, G. W., and R. P. Burden. 1997. "An analysis of the shapes of sea ice ridges." *Cold Regions Science and Technology* 25 (1): 65–77. DOI:[10.1016/S0165-232X\(96\)00017-1](https://doi.org/10.1016/S0165-232X(96)00017-1).
- Tofani, V., F. Raspini, F. Catani, and N. Casagli. 2013. "Persistent Scatterer Interferometry (PSI) technique for landslide characterization and monitoring." *Remote Sensing* 5: 1045–1065. DOI:[10.3390/rs5031045](https://doi.org/10.3390/rs5031045).
- Torres, R., P. Snoeij, D. Geudtner, D. Bibby, M. Davidson, E. Attema, P. Potin et al. B. Rommenna, N. Floury, M. Brown, I. N. Traver, P. Deghaye, B. Duesmann,

- B. Rosich, N. Miranda, C. Bruno, M. L'Abbate, R. Croci, A. Pietropaolo, M. Huchler, F. Rostanc. 2012. "GMES Sentinel-1 mission." *Remote Sensing of Environment* 120: 9–24. DOI:[10.1016/j.rse.2011.05.028](https://doi.org/10.1016/j.rse.2011.05.028).
- Ulaby, F. T., D. G. Long, W. Blackwell, C. Elachi, A. Fung, Ch. Ruf, K. Sarabandi, J. v. Zyl, and H. Zebker. 2014. *Microwave Radar and Radiometric Remote Sensing*. Ann Arbor, Michigan: University of Michigan Press.
- User guide Sentinel 1. Available online: <https://sentinel.esa.int/web/sentinel/user-guides/sentinel-1-sar/revisit-and-coverage> (accessed on 2021).
- Veci, L. *Interferometry Tutorial*. Array Systems. Available online: <http://sentinel1.s3.amazonaws.com/docs/S1TBX%20Stripmap%20Interferometry%20with%20Sentinel-1%20Tutorial.pdf> (accessed on 12 August 2017).
- Vesecky, J. F., R. Samadani, M.P. Smith, J.M. Daida, and R.N. Bracewell. 1988. "Observation of sea-ice dynamics using synthetic aperture radar images: automated analysis." *IEEE Transactions on Geoscience and Remote Sensing* 26 (1): 38-47. DOI:[10.1109/36.2998](https://doi.org/10.1109/36.2998).
- Voipio, A. 1981. *The Baltic Sea*. Amsterdam, Holland: Elsevier Oceanography Series No. 30, 1981.
- Volkov, V. A., O. M. Johannessen, V. E. Borodachev, G. N. Voinov, L. H. Pettersson, L. P. Bobylev, and A. Kouraev. 2002. *Polar Seas Oceanography—An Integrated Case Study of the Kara Sea*. Springer-Praxis series in Remote Sensing.
- Wadhams, P. 2000. *Ice in the ocean*. Amsterdam, the Netherlands: Gordon & Breach Science Publishers.
- Wang, L., K. Deng, and M. Zheng. 2020. "Research on ground deformation monitoring method in mining areas using the probability integral model

- fusion D-InSAR, sub-band InSAR and offset-tracking”. *International Journal of Applied Earth Observation and Geoinformation* 85: 101981. DOI:[10.1016/j.jag.2019.101981](https://doi.org/10.1016/j.jag.2019.101981).
- Wang, Zh., J. Liu, J. Wang, L. Wang, M. Luo, Z. Wang, P. Ni, and H. Li. 2020. “Resolving and Analyzing Landfast Ice Deformation by InSAR Technology Combined with Sentinel-1A Ascending and Descending Orbits Data.” *Sensors* 20 (22): 6561. DOI:[10.3390/s20226561](https://doi.org/10.3390/s20226561).
- Weeks, W. F. 1980. “Overview”. *Cold Regions Science and Technology* 2, 1–35. [A general presentation of the structural fields of sea ice covers]
- Weeks, W.F. 1998. “Growth conditions and structure and properties of sea ice” In *Physics of Ice-Covered Seas*, Vol. 1, pp. 25–104. Helsinki University Press, Helsinki. [Structure of ice freezing from saline water].
- Weeks, W.F. 2010. *On sea ice*. Fairbanks: University of Alaska Press.
- Weeks, W.F. and S.F. Ackley. 1986. “The growth, structure, and properties of sea ice.” In *the geophysics of sea ice*. Edited by N. Untersteiner, 9-164. New York: Plenum Press.
- Weeks, W.F., A. Kovacs, and W.D. Hibler. 1971. “Pressure ridge characteristics in the Arctic coastal environment.” In *proceedings of the 1st International Conference on Port and Ocean Engineering under Arctic Conditions (POAC)*. Trondheim, Norway. Retrieved from. http://www.poac.com/Papers/POAC71_V1.zip.
- JCOMM Expert Team on Sea Ice, Sea-Ice Nomenclature: Snapshot of the WMO Sea Ice Nomenclature WMO No. 259, Terminology and Codes, WMO-JCOMM, 2014, vol. 1, 1st ed. 1970, DOI:[10.25607/OBP-1515](https://doi.org/10.25607/OBP-1515).
- Werner, Ch., U. Wegmueller, T. Strozzi, and A. Wiesmann. 2000. “GAMMA SAR and interferometric processing software.” European Space Agency-ENVISAT Symposium, Gothenburg, Sweden, 16-20 Oct.

- Woodgate, R. A., T. Weingartner, and R. Lindsay. 2010. "The 2007 Bering Strait oceanic heat flux and anomalous arctic sea-ice retreat." *Geophysical Research Letters* 37 (1). DOI:[10.1029/2009GL041621](https://doi.org/10.1029/2009GL041621).
- Yitayew, T., V. Dierking, D.V. Divine, T. Eltoft, L. Ferro-Famil, A. Rösel, and J. Negrel. 2018. "Validation of Sea-Ice Topographic Heights Derived From TanDEM-X Interferometric SAR Data With Results From Laser Profiler and Photogrammetry." *IEEE Transactions on Geoscience and Remote Sensing* 56 (11): 6504–6520. DOI:[10.1109/TGRS.2018.2839590](https://doi.org/10.1109/TGRS.2018.2839590).
- Yu, Q., C. Moloney, and F. M. Williams. 2002. "SAR sea-ice texture classification using discrete wavelet transform based methods." *In proceedings of the IEEE Geoscience and Remote Sensing Symposium*, Toronto, Canada, 24–28 July 2002; Volume 5, pp. 3041–3043.
- Zakhvatkina, N. Y., V. Y. Alexandrov, O. M. Johannessen, S. Sandven, and I. Y. Frolov. 2013. "Classification of Sea Ice Types in ENVISAT Synthetic Aperture Radar Images." *IEEE Transactions on Geoscience and Remote Sensing* 51 (5): 2587–2600. DOI:[10.1109/TGRS.2012.2212445](https://doi.org/10.1109/TGRS.2012.2212445).
- Zebker, H. A. and J. Villasenor. 1992. "Decorrelation in interferometric radar echoes." *IEEE Transactions on Geoscience and Remote Sensing* 30 (5): 950–959. DOI:[10.1109/36.175330](https://doi.org/10.1109/36.175330).
- Zubov, N. N. 1945. *Arctic Ice (in Russian)*, 491 pp., Moscow: Istatel'stvo Glasevmorputi.
- Zhou, H., J. Zhang, L. Gong, and X. Shang. 2012. "Comparison and Validation of Different DEM Data Derived from InSAR". *Procedia Environmental Sciences* 12: 590–597. DOI:[10.1016/j.proenv.2012.01.322](https://doi.org/10.1016/j.proenv.2012.01.322).